Modelling Framework for Radio Frequency Spatial Measurement

by

Andrew Donald Wiles

A thesis
presented to the University of Waterloo
in fulfilment of the
thesis requirement for the degree of
Master of Applied Science
in
Systems Design Engineering

Waterloo, Ontario, Canada, 2006

I hereby declare that I am the sole author of this thesis. This is a true copy of the thesis, including any required revisions, as accepted by my examiners.

I understand that my thesis may be made electronically available to the public.

Andrew D. Wiles

Abstract

The main crux of this thesis was to produce a model that was capable of simulating the theoretical performance of different configurations for a spatial measurement system using radio frequency technology. It has been important to study new modalities of spatial measurement since spatial measurement systems are an enabling technology that have allowed for the creation of better medical procedures and techniques, provided valuable data for motion capture in animation and biomechanics, and have improved the quality of manufacturing processes in many industries. However, there has been room for improvement in the functional design and accuracy of spatial measurement systems that will enhance current applications and further develop new applications in medicine, research and industry.

In this thesis, a modelling framework for the investigation of spatial measurement based on radio frequency signals was developed. The simulation framework was designed for the purpose of investigating different position determination algorithms and sensor geometries. A finite element model using the FEMLAB partial differential equation modelling tool was created for a time-domain model of electromagnetic wave propagation in order to simulate the radio frequency signals travelling from a transmitting source antenna to a set of receiving antenna sensors. Electronic line signals were obtained using a simple receiving infinitesimal dipole model and input into a time difference of arrival localization algorithm. The finite element model results were validated against a set of analytical solutions for the free space case. The accuracy of the localization algorithm was measured against a set of possible applications for a potential radio frequency spatial measurement system design.

It was concluded that the simulation framework was successful should one significant deficiency be corrected in future research endeavours. A phase error was observed in the signals extracted at the receiving antenna locations. This phase error, which can be up to 40°, was attributed to the zeroth order finite elements implemented in the finite element model. This phase error can be corrected in the future if higher order vector elements are introduced into future versions of FEMLAB or via the development of custom finite element analysis software but were not implemented in this thesis due to time constraints. Other improvements were also suggested for future work.

Acknowledgments

It truly is amazing that for an independent body of work such as this thesis that there are so many people out there that need to be acknowledged for their contribution to this work. First of all, I would like to thank my supervisors Eric Kubica and Shane Pinder for providing me the opportunity to pursue this line of research under their guidance. My appreciation is not limited to their valuable input throughout this two year process but also for their willingness to embark on this research experience.

I also need to extend my sincere gratitude to the people at Northern Digital Inc.(NDI) who have supported me in my academic addiction. There are very few corporations that exist that would support an employee in the manner that NDI has supported me. In particular, David Crouch and Stephen Leis of the senior management team showed a level of trust and belief in my abilities that have flattered and empowered me at the same time. Laura Kacur and Lee Murray of the Human Resources group worked tirelessly to ensure the NSERC Industrial Postgraduate Scholarship was approved and that the transition from employee to graduate student occurred smoothly. I also need to thank the members of the Advanced Research Group who were always willing to engage in technical discussions. Specifically, Terry Fisher, Geoff Vanderkooy, Christian Schilling, Georg Brunner and Stefan Kirsch participated in monthly meetings dubbed as the RF steering committee. David Swart and John Nieminen were also very valuable sounding boards in the final stretch of this process as they provided an attentive ear, some valuable references and ideas that helped me complete this project. Last but definitely not least, Don Frantz who has been one of my mentors at NDI provided me with a wealth of information that included technical ideas, historical reviews and other not so relevant tidbits of information.

Finally, I need to deeply thank my family for bearing with me through this process. My parents, grandparents, brother and in-laws have provided me a great deal of support and patience as I have occasionally neared the brink of insanity and missed a few family events. However, my deepest gratitude is reserved for my wife Meg who never wavered in her undying love and support that propelled me from start to finish.

This work was supported by the National Science and Engineering Research Council and Northern Digital Inc.

For my grandmother, grandfather and Meg.

Contents

List of Figures

List of Tables

Nomenclature and Definitions

Variable Types and Operators

$a \equiv$ scalar variable

$\bar{\boldsymbol{a}} \equiv$ vector variable

$\hat{\boldsymbol{a}} \equiv$ unit vector variable

$\boldsymbol{A} \equiv$ matrix variable

$\boldsymbol{a} \equiv$ tensor variable

$\tilde{\boldsymbol{a}}, \tilde{\boldsymbol{A}} \equiv$ Time-varying vector field where $\tilde{\boldsymbol{A}} = \tilde{\boldsymbol{A}}(x, y, z, t)$. e.g., the electric field intensity is $\tilde{\boldsymbol{E}}$.

$\bar{\boldsymbol{a}} \odot \bar{\boldsymbol{b}} \equiv$ element by element multiplication, $a_x b_x \hat{\boldsymbol{x}} + a_y b_y \hat{\boldsymbol{y}} + a_z b_z \hat{\boldsymbol{z}}$.

$\bar{\boldsymbol{a}} \cdot \bar{\boldsymbol{b}} \equiv$ Dot product of vectors $\bar{\boldsymbol{a}}$ and $\bar{\boldsymbol{b}}$

$\bar{\boldsymbol{a}} \times \bar{\boldsymbol{b}} \equiv$ Cross product of vectors $\bar{\boldsymbol{a}}$ and $\bar{\boldsymbol{b}}$

$|\bar{\boldsymbol{a}}| \equiv$ Magnitude of a vector given by $\sqrt{\bar{\boldsymbol{a}} \cdot \bar{\boldsymbol{a}}}$

$\nabla \equiv$ Gradient of a scalar or vector (see Appendix A.3).

$\nabla\cdot \equiv$ Divergence of a scalar or vector (see Appendix A.3).

$\nabla\times \equiv$ Curl of a scalar or vector (see Appendix A.3).

$\nabla^2 \equiv$ Laplacian of a scalar or vector (see Appendix A.3).

$\tilde{\boldsymbol{A}}^+ \equiv$ field value on the *up* side of a boundary.

$\tilde{\boldsymbol{A}}^- \equiv$ field value on the *down* side of a boundary.

$\mathbb{R} \equiv$ Defines the number space in terms of a scalar space ($\mathbb{R}$) or two-dimensional vector space ($\mathbb{R}^2$) or three-dimensional vector space ($\mathbb{R}^3$).

$\Re \equiv$ An operator that considers only the real part of a complex variable.

$\mathcal{L} \equiv$ Differential operator where $\mathcal{L}(u)$ is a linear function of arbitrary derivatives of the variable u.

Specific Variables

$\tilde{\boldsymbol{E}} \equiv$ electric field intensity
$V \equiv$ voltage
$\tilde{\boldsymbol{E}}^i \equiv$ incident electric field intensity
$\tilde{\boldsymbol{E}}^s \equiv$ scattered electric field intensity
$\tilde{\boldsymbol{E}}_0 \equiv$ specified electric field intensity
$\tilde{\boldsymbol{H}} \equiv$ magnetic field intensity
$\tilde{\boldsymbol{D}} \equiv$ electric flux density
$\tilde{\boldsymbol{B}} \equiv$ magnetic flux density
$\tilde{\boldsymbol{J}} \equiv$ electric current density
$\tilde{\boldsymbol{\rho}} \equiv$ electric charge density
$\tilde{\boldsymbol{A}} \equiv$ magnetic vector potential
$\phi \equiv$ magnetic scalar potential or correlation function
$\tilde{\boldsymbol{K}} \equiv$ a redefined magnetic vector potential
$\varepsilon \equiv$ permittivity (free space value: ε_0)
$\mu \equiv$ permittivity (free space value: μ_0)
$\sigma \equiv$ conductivity
$\Omega \equiv$ system volume or sub-domain
$\Gamma \equiv$ system boundary
$\bar{\boldsymbol{v}} \equiv$ test vector function
$f \equiv$ frequency
$t \equiv$ time
$\lambda \equiv$ wavelength
$c_0 \equiv$ speed of light
$\bar{\boldsymbol{p}} \equiv$ position vector
$\tau \equiv$ time delay
$\theta \equiv$ angle variable
$\delta \equiv$ angular error

Coordinate Systems

Cartesian Coordinates	$\bar{\boldsymbol{p}} = x\hat{\boldsymbol{e}}_x + y\hat{\boldsymbol{e}}_y + z\hat{\boldsymbol{e}}_z$
Spherical Coordinates	$\bar{\boldsymbol{p}} = r\hat{\boldsymbol{e}}_r + \theta\hat{\boldsymbol{e}}_\theta + \phi\hat{\boldsymbol{e}}_\phi$

Terminology

marker	an object of which the position measurement is obtainable, e.g., an infrared LED in an optical spatial measurement device or an electric coil in a magnetic sensor.
position sensor	the sensing device that measures the position of a marker, e.g., the CCD camera in an optical sensor.
sensor array	group of sensors in uniform or non-uniform pattern that form the position sensor, e.g., collection of antennas used in time difference of arrival measurements.

Acronyms

BVP	Boundary value problem.
GPS	Global positioning system.
RF	Radio frequency.
TDOA	Time difference of arrival.

Chapter 1

Introduction

Spatial measurement systems have a long history of development and have quite a varied selection of implementations. From a simple ruler that measures a one-dimensional length to a measuring cup that provides volumes to a highly complex coordinate measurement machine that provides basic three-dimensional coordinates, spatial measurement is a necessity in science, engineering and other everyday life activities.

Some of the great feats in spatial measurement can be attributed to the great explorers of the New World. Magellan, Cartier and many others sought out to explore unknown land and sea which resulted in the creation of maps that would guide them in a return visit for colonization of the new lands or trade with other civilizations. The early maps eventually led to a reference system of longitude and latitude that allowed sea going vessels to navigate safely relative to known landmarks and sun patterns. Eventually, other measurement systems such as LORAN-C[1] [40] and various forms of RADAR technology [32] were developed. A very active area of research today is the use of phased array techniques to improve the accuracy of RADAR [15]. Now global positioning systems (GPS) are widely used to assist sea captains in their travels [30, 39].

Global positioning systems have also opened up other opportunities where spatial measurement is critical. In particular, geographical information systems (GIS) have become quite prevalent in tourism, industrial asset tracking and military activities [17]. In tourism, GPS receivers are tied into a geographical database that can return relevant local informa-

[1]LORAN-C is a positioning system that is similar to GPS except that the reference transmitters are ground based stations located throughout Europe and North America.

tion to the user such as the closest hotel or seafood restaurant. In industrial asset tracking, shipping companies are able to monitor their trucks, train cars and other shipping vessels in order to optimize their shipping needs. Finally, military groups, particularly those of the United States who have access to the more accurate GPS signal which is encrypted for national security applications [39], can potentially use position data from infantry units and naval ships to track their soldiers progress without having to relay the information via other easily intercepted communication channels.

The industrial revolution created a whole other need for spatial measurement as mass production machinery was invented. An example industry is the automotive industry which required parts to be manufactured accurately and repeatedly. In the 1960s, the coordinate measurement machine (CMM) was developed that could be used for part tolerance inspection, reverse engineering tasks and other general measurement requirements [70]. From table top systems to gantry style systems that can fit an entire cube van, the coordinate measurement machine solved a problem of spatial measurement[2]. However, as the industrial revolution continues to march forward and manufacturing techniques improve, manufacturers want to be able to bring their coordinate measurement machines right to the production assembly line. The current designs of coordinate measurement machines make this task difficult and so other solutions have been sought. Articulated arms came to the forefront as the first portable coordinate measurement machines (PCMM) and are briefly discussed in Section 2.2.2. Originally developed for digitizing objects to bridge the gap between physical models and animation, the articulated arms were small enough to be used on the assembly lines. The open-loop kinematic measurement systems continued to be developed and the possible measurement volume became larger and the measurement performance became more accurate. However, experience has revealed that manufacturers sought to provide their workers on the assembly line with a more versatile measurement system that did not require them to be connected to a rigid and somewhat cumbersome system that were the articulated arms.

Today, optical measurement systems have been introduced into production assembly lines as the newest generation of the portable coordinate measurement machine. As with the articulated arms, optical measurement machines were developed primarily for other applications. For example, Northern Digital Inc. [45] developed the WATSMART system in

[2]Laser interferometers were also developed in order to calibrate and characterize the coordinate measurement machines.

1984 primarily for biomechanics research at the University of Waterloo. The multi-camera measurement system provided researchers some of the first three-dimensional measurement data for gait and other human movement research which were previously limited to two-dimensional data provide by cinematography and video machines [69]. The success of the WATSMART system led to the further development of other optical and magnetic tracking devices at Northern Digital and other spatial measurement system producers for use in many applications. Some of these applications include (i) motion capture systems for animation and video gaming, (ii) detailed biomechanics research and (iii) computer assisted surgery and therapy[3] techniques [49]. It is in these applications where the need for a "local position measurement system" will be the focus of the work presented in this thesis.

Table 1.1 provides a summary of the typical working volume and their associated required accuracy levels. The content in this table is based on the experiences of the author working in the metrology industry. The table shows that there have been a varied range in the operational volumes and in the accuracy requirements for each application. The industrial PCMM solution has the most stringent requirements and also has some additional parameters. The industrial PCMM system is required to operate in what is typically the most strenuous environment where temperatures can range from near freezing to extreme heat and humidity in large manufacturing facilities.

In computer assisted surgery and gait analysis two types of three-dimensional spatial measurement systems, optical and magnetic, have been typically used. Examples include the Polaris, Optotrak and Aurora from Northern Digital Inc. (NDI) [45]; Polhemus' magnetic tracker [50]; and the Flock of Birds from Ascension Technology Corporation [3]. Each type has its own weaknesses that prevent the systems from being used in certain cases. For example, optical systems have required that the camera systems have an unobstructed view of the infrared LEDs or retro-reflective spheres/discs, i.e. the position sensors must maintain direct line of sight of the markers. If the markers become occluded due to the users or equipment being used then the position sensor is unable to track. Magnetic systems on the other hand do not require a direct line of sight but they can be very sensitive to ferromagnetic materials present in both the region of interest and beyond. The *holy grail* of local position measurement has been a system that can overcome these two main

[3]Originally called "image-guided surgery", the term "computer assisted surgery and therapy" is typically used to better capture the state of the art of surgical systems available today.

Application	Typical Volume	Required Accuracy
Motion Capture and Biomechanics	Small experimental volume would be 2m by 2m by 2m while a larger experiment could require 10m by 10m by 3m or larger.	Typically centimeter level accuracy is sufficient but improvements in biomechanical models are requiring more accuracy.
Computer Assisted Surgery	Approximately 1.0m^3 sphere for neurosurgery and 2.0m by 2.0m by 2.0m for orthopaedic procedures.	Sub-millimeter accuracy typically required but orthopaedic procedures are beginning to require better accuracy.
Industrial PCMM	Volume should be able to contain an entire automobile.	Applications require accuracies from 0.5mm to less than 0.1mm.

Table 1.1: Example applications using spatial measurement devices and their typical specifications. These specifications are not found neatly summarized in the literature but are based on the author's experiences working in the metrology industry.

defects in the current complement of systems. Further, the wish list for many engineers includes the desire for wireless probes that can be inserted into the body for pathology diagnosis, treatment and study.

In working towards creating the *holy grail* of measurement, scientists in the metrology community have been researching different modalities of measurable signals. In particular, radio frequency signals have become a focus for some researchers. Stelzer et al. have demonstrated a radio frequency system similar to today's global positioning systems which are also based on radio frequency signals [59, 60]. The fundamental difference in Stelzer's local position measurement system and the global position system was that Stelzer uses a time difference of arrival technique instead of the time of flight algorithm used in global position systems [4]. However, the system only exhibits a 10cm accuracy for a 500m by 500m test area and was still essentially a two-dimensional system. The performance of Stelzer's system is limited by the systems ability to resolve the time difference of arrival between transmitter and receiver to a level that provides sub-decimeter performance. Other attempts at radio frequency measurement systems have been based on taking the known information of global positioning systems and simply scaling them down with some correction factors for localized issues which still only results in centimeter accuracy levels. This clearly does not match the goals of the applications mentioned earlier in this chapter.

There are three main factors driving the desire to investigate a radio frequency measurement system. First, there has been a significant advancement in radio frequency circuitry in the recent past. Radio frequency circuitry is successfully being miniaturized in a convenient package that provides technology end users highly functional cellular telephones, two-way paging systems and wireless internet systems. A quick review of today's technology publications will show that micro-electromechanical systems (MEMS), micro-optoelectromechanical systems (MOEMS) and nanotechnology endeavours are continuing to provide an opportunity to reduce the size of radio frequency circuitry. Second, antenna research is also advancing in the direction of miniaturization. Again, MEMS and nanotechnology research are providing opportunities to reduce the sizes of current half-wavelength antennas and the like. An example includes the floating-patch MEMS antenna presented by Cho et al. [18] which measures less than $5mm^2$. Finally, the state of the art in computing power provides a new level of analysis where highly complex systems, such as radiating

[4] Section 2.2.1 describes some of the details for the two techniques.

and receiving antennas, can be simulated in order to study their behaviors using virtual prototyping before building an expensive real world prototype.

Radio frequency signals provide some significant challenges that need to be overcome before a solution is deemed acceptable. The most significant problem with radio frequency local measurement systems has been that the radio frequency signals are affected by occluding objects and reflective objects. However, there are techniques available to distinguish reflected signals from non-reflected signals using beam forming technology via phased array configurations [14, 15]. Current research has been based in empirical experiments and model based design using a top-down design methodology. That is, design and development projects in radio frequency spatial measurement have been focused on developing prototypes with corrective models rather than studying the associated physics and developing metrology theory.

In this thesis, a different methodology for solving the problem of spatial measurement using radio frequency based signals is presented based on a bottom-up design methodology. That is, start with the basic building blocks of a radio frequency system and slowly add to the complexity through simulation to study the problem, one phenomenon at a time. The reason this methodology is useful is two-fold. First, the bottom-up design methodology allows for the physics and interactions to be studied at a fundamental level. Using Maxwell's equations, electromagnetic waves (a superset of radio frequency waves) can be solved analytically and simulated numerically. Simple objects can be introduced to the situation that in turn create a complex environment for the local position measurement system. The simulation environment allows the researcher to study the problem with full control over the level of noise and errors present in the system. Often in empirical research and top-down design methodology, there are several sources of error (i.e., electronic component non-linearities and errors, external noise sources, etc.) that can mislead a researcher as the real world environment creates a constant flux in the experimental conditions. The simulations can be later verified using empirical research where additional noise and errors need to be identified.

Second, the bottom-up design allows the research to study the problem in abstract and theoretical situations. In particular, unique sensor configurations or array designs can be studied without the need to create a physical prototype and conduct costly empirical experiments. For example, Figure 1.1 shows a theoretical concept of a sensor that may be successful in a radio frequency measurement system. In general, the radio frequency

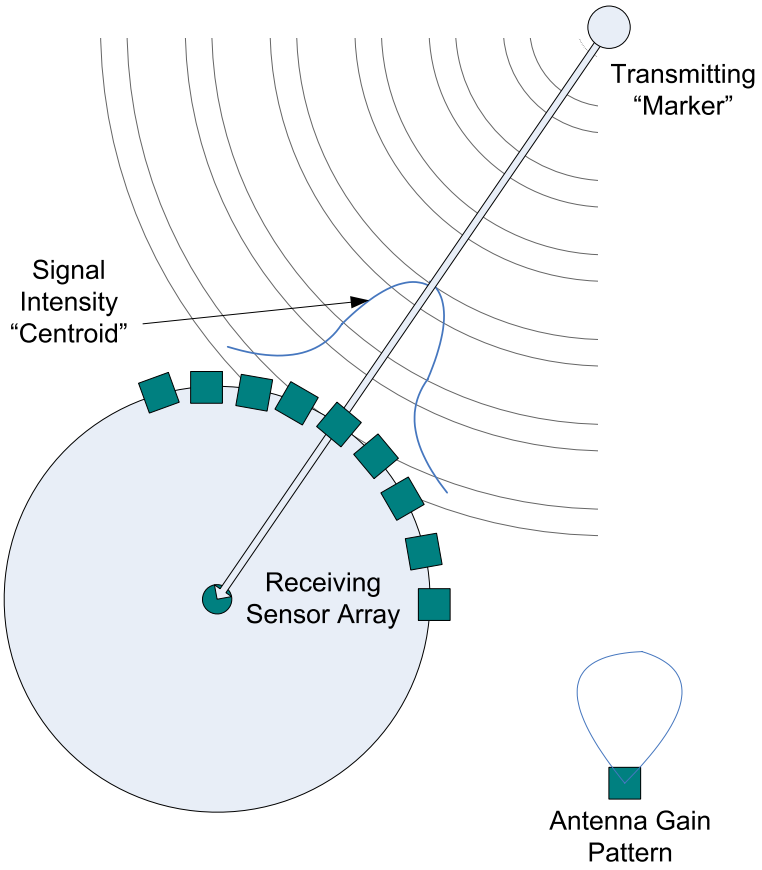

Figure 1.1: Concept diagram for a given sensor of a radio frequency spatial measurement system. An independent array of antennas isplaced on a ring or sphere. The gain of the antennas are a function of angle and hence the signal from a given marker forms a "centroid" on the surface of the ring or sphere. In the case of a circular array a plane that passes through the location of the marker can be defined by the centroid and the center of the ring. A spherical array would provide a line that passes through the center of the sphere, the centroid and the marker. Both a time difference of arrival solution and time of flight solution can be implemented very easily in order to study the inherent errors of all three methods.

spatial measurement systems being investigated; including GPS, the work by Stelzer et al. and other unreferenced experiments; tend to be focused on time based measurement solutions. The configuration diagramed in Figure 1.1 is a spatially based measurement system. In this conceptual design, an array of antennas is placed on a sphere of known radius. Each antenna is tuned to have a gain pattern that peaks in the direction of a line that passes through both the center of the sphere and the antenna itself. Then, if there exists a radiating marker in space (e.g., a radiating antenna), the independent array of antennas can receive the signals and through signal processing a waveform[5] as shown by the Gaussian shape profile in the figure can be created. A weighted average algorithm can be used to determine a centroid for the waveform and a line can be defined in a local coordinate frame as passing through the center[6] of the sphere and centroid. Two or more sets of sensors will allow for the definition of two or more lines where in a global coordinate frame the intersection, or near intersection, of the two lines will provide the location of the source (see Section 2.2.1 for a more detailed description on the intersection of lines method).

Unfortunately, in practice this type of concept is not easily investigated for two reasons: (i) cost of prototype and (ii) coupling of closely positioned antennas. The cost of investigating such a prototype would be very expensive and highly complex to build as the signal acquisition hardware may need to extract signals from potentially hundreds of antennas. Although simple back of the napkin calculations would suggest that the configuration is potentially a good solution, there are many potential caveats that would make the physical prototype an exercise in fiscal waste. Further, there are additional problems such as noise and interference between antennas that are close to one another which adds to the complexity of the investigation.

However, investigating this concept of radio frequency spatial measurement in a virtual prototype or simulation in a logical bottom-up design process allows for a number of these problems to be avoided. Specifically, data acquisition problems are generally avoided, assuming the computer can handle the amount of data being generated. Also, the effect of coupling between adjacent antennas can be added and removed from the simulation

[5]The use of the term waveform is an analogy to the terminology used with optical position measurement systems where the waveform is the raw signal obtained for a linear charge-couple device (CCD) array.

[6]The center of the sphere is analogous to the focal point of the lens system in an optical spatial measurement system.

depending on the phenomenon of interest at the time. Furthermore, other methods of spatial measurement can be studied including time-based methods or hybrid methods that combine both time and spatial based properties.

With the idea of a virtual testing platform in mind, the goal of this thesis is to develop a theoretical model that can be used for the simulation of multiple configurations of a radio frequency spatial measurement device. The model defines the propagation of a signal in the form of an electromagnetic wave in the radio frequency portion of the spectrum travelling from a transmitting antenna (marker) through a volume that may contain physical objects to a set of receiving antennas (sensors). The signals at the receiving antennas are then used as input into a position localization algorithm, such as the time difference of arrival method, in order to determine the position of the transmitting antenna. The model is implemented using the finite element method which allows for the study of the effect that attenuating and reflective objects have on the ability to accurately determine the position of the transmitting antenna if the locations of the objects are not known *a priori* to the sensor system. The physical objects investigated in the simulation would include simple book shelves, tables and other similar laboratory equipment or the objects could be anything that may appear in an operating room or along a manufacturing production line. The existence of these objects in the field would not be known to the sensor system and algorithms. The next phase of research beyond this thesis is to use the model in a full set of simulations studying various marker and sensor configurations as well as different localization algorithms. With the successful development of a model, the first potential test configuration that may be simulated is introduced earlier in this chapter and is depicted in Figure 1.1.

The remaining chapters in this thesis describe the proposed model, the techniques to solve the model and some results explaining its performance. Chapter 2 begins with some background information including a description of the electromagnetic theory and spatial measurement theory that is referenced throughout the remainder of the thesis. Chapter 3 discusses the use of the finite element method to model the propagation of electromagnetic waves through a specified volume that may or may not contain objects that can cause attenuations and reflections of radio frequency signals. The chapter is separated into three sections where first the governing equations are derived using the weak formulation. Second, a discussion on the realities of implementing a finite element model for electromagnetic wave propagation using the chosen software tool, FEMLAB,

is provided. Finally, the methods of applying an excitation (i.e., radiating marker) and receiving a signal (i.e., sensor array) are presented. Chapter 4 is an analysis on the accuracy of the finite element method for three different source signals including plane waves (i.e., a propagating wave where its source exists at a location infinitely far from the region of interest), cylindrical waves (i.e., a propagating wave from an infinitely long line source such as a wire) and spherical waves (i.e., a propagating wave from a point source). Chapter 5 describes the use of the time difference of arrival algorithm for position measurement in detail. The end of this chapter presents the results of the integration of the finite element model presented in Chapter 3 and the time difference of arrival algorithm presented earlier in the chapter. It is here where the limitations of the chosen software tool for this framework are brought to light. Finally, Chapter 6 provides a summary of the work presented and discusses the next steps for this research endeavour.

Chapter 2

Background

The main crux of this thesis is to produce a theoretical model that can be used in simulation to determine the theoretical performance of different configurations for a spatial measurement system using radio frequency technology. In order to accomplish this goal there are two main components of the simulation framework that need to be considered. The first consists of how electromagnetic (EM) waves are simulated using Maxwell's equations and the techniques used in computational electromagnetics. Second, the different methods of position determination are discussed.

In this section, a brief introduction is provided to both components. This section is not exhaustive but it should provide enough background for understanding the methods and relevance of the results in the rest of thesis.

2.1 Simulation Methods for Computational Electromagnetics

Nearly all computational electromagnetic problems are based on being able to solve Maxwell's equations for a given situation. Here the general form of Maxwell's equations as used in the FEMLAB software is shown [20]. A more general version of Maxwell's equations can be found in Balanis' text on Electromagnetics [5][1].

[1]The more general form in Balanis' text contains a source magnetic current density ($\tilde{\boldsymbol{J}}_m$ volts/square meter) and a magnetic charge density ($\tilde{\boldsymbol{\rho}}_m$ webers/cubic meter). These are removed in the FEMLAB

James Clerk Maxwell was not credited with the discovery of all of the four equations that are associated to his name, rather Maxwell is credited with combining the four equations, discovered by other scientists, in order to create a unified theory that describes an electromagnetic wave. The four equations are Maxwell-Ampere's Law (equation 2.1), Faraday's Law (equation 2.2), Gauss' Electric Law (equation 2.3) and Gauss' Magnetic Law (equation 2.4). The equations are summarized below using the differential form with field notation with the variables defined in Table 2.1 [5].

Maxwell-Ampere's Law relates the curl of the magnetic field ($\tilde{\boldsymbol{H}}$) to the electric current density ($\tilde{\boldsymbol{J}}$) and the electric flux density ($\tilde{\boldsymbol{D}}$).

$$\nabla \times \tilde{\boldsymbol{H}} = \tilde{\boldsymbol{J}} + \frac{\partial \tilde{\boldsymbol{D}}}{\partial t} \tag{2.1}$$

Faraday's Law is of the same form of Maxwell-Ampere's Law relating the electric field ($\tilde{\boldsymbol{E}}$) and magnetic flux density ($\tilde{\boldsymbol{B}}$). Notice that that the magnetic current density has been dropped as it is not a physically realizable component [5].

$$\nabla \times \tilde{\boldsymbol{E}} = -\frac{\partial \tilde{\boldsymbol{B}}}{\partial t} \tag{2.2}$$

Gauss' Electric and Magnetic Laws relate the flux densities for the electric and magnetic fields respectively to the associated charge densities. Again, notice that the magnetic charge density has been assumed to be negligible.

$$\nabla \cdot \tilde{\boldsymbol{D}} = \tilde{\boldsymbol{\rho}}, \tag{2.3}$$

$$\nabla \cdot \tilde{\boldsymbol{B}} = 0. \tag{2.4}$$

In all four of Maxwell's equations, $\tilde{\boldsymbol{E}}$, $\tilde{\boldsymbol{H}}$, $\tilde{\boldsymbol{D}}$, $\tilde{\boldsymbol{B}}$, $\tilde{\boldsymbol{J}}$ and $\tilde{\boldsymbol{\rho}}$ are field variables that are time-varying and are a function of the space coordinates and time, e.g., $\tilde{\boldsymbol{E}} = \tilde{\boldsymbol{E}}(x, y, z, t)$ and $\tilde{\boldsymbol{E}} \in \mathbb{R}^3$.

An additional useful relationship is the equation of continuity

$$\nabla \cdot \tilde{\boldsymbol{J}} = -\frac{\partial \tilde{\boldsymbol{\rho}}}{\partial t}. \tag{2.5}$$

model as they are not useful in the wave propagation model.

Variable	Definition
$\tilde{\boldsymbol{H}} \equiv$	magnetic field intensity (amperes/meter)
$\tilde{\boldsymbol{E}} \equiv$	electric field intensity (volts/meter)
$\tilde{\boldsymbol{B}} \equiv$	magnetic flux density (webers/square meter)
$\tilde{\boldsymbol{D}} \equiv$	electric flux density (coulombs/square meter)
$\tilde{\boldsymbol{J}} \equiv$	electric current density (amperes/square meter)
$\tilde{\boldsymbol{\rho}} \equiv$	electric charge density (coulombs/cubic meter)

Table 2.1: Definition of electromagnetic variables for Maxwell's equations as described by Balanis [5].

The equation of continuity simply shows that the surface current is directly related to the time rate of change of the charge density.

Of the four equations presented by Maxwell and the equation of continuity, only three are independent. The EM fields can be solved for using Maxwell-Ampere's Law (equation 2.1), Faraday's Law (equation 2.2) and either one of Gauss's Electric Law (equation 2.3) or the Equation of Continuity(equation 2.5)[2]. However, there are three equations, in vector form, and the six unknowns in vector form listed in Table 2.1. Therefore, constitutive relationships are required that relate the flux densities to the field intensities and the current densities to the charge densities

$$\tilde{\boldsymbol{D}} = \varepsilon_0 \tilde{\boldsymbol{E}} + \tilde{\boldsymbol{P}}, \tag{2.6}$$

$$\tilde{\boldsymbol{B}} = \mu_0 \left(\tilde{\boldsymbol{H}} + \tilde{\boldsymbol{M}} \right), \tag{2.7}$$

$$\tilde{\boldsymbol{J}} = \sigma \tilde{\boldsymbol{E}}, \tag{2.8}$$

where $\tilde{\boldsymbol{P}}$ and $\tilde{\boldsymbol{M}}$ are the electric and magnetic polarization vectors respectively for the given material and the Greek variables are the material properties for electromagnetics. The permittivity, ε, describes the dielectric properties of the material which relates to the materials ability to store electric charge. The permeability, μ, describes the ability of a material to become magnetized when exposed to an applied magnetic field. The

[2]This is only possible because the magnetic currents and charges are deemed negligible, therefore, throughout the remainder of this thesis the magnetic currents and charge densities will be assumed set to zero unless otherwise stated.

conductivity, σ, relates the current density in a material to the applied magnetic field. These properties are summarized in Table 2.2 and the derivation of the material specific values follows.

Variable	Definition	Value in Free Space
$\varepsilon \equiv$	permittivity (farads/meter)	$\varepsilon_0 = 8.854 \times 10^{-12}$
$\mu \equiv$	permeability (henries/meter)	$\mu_0 = 4\pi \times 10^{-7}$
$\sigma \equiv$	conductivity (siemens/meter)	$\sigma_0 = 0$

Table 2.2: Definition of material properties variables for the constitutive equations needed to solve Maxwell's equations.

The third constitutive equation is relatively straight forward, however, the first two constitutive equations, (equations 2.6 and 2.7) introduce two additional time-varying values. For linear and isotropic materials where the electric properties are uniformly constant in all spatial dimensions, these values can be written in terms of the field intensities because the two equations in question have a free space term and a material specific term. That is, the first term in equation 2.6 is $\varepsilon_0 \tilde{\boldsymbol{E}}$ which is the flux density for free space. The second term is the material specific term where $\tilde{\boldsymbol{P}}$ can be expressed as $\tilde{\boldsymbol{P}} = \varepsilon_0 \chi_e \tilde{\boldsymbol{E}}$ where χ_e is the electrical susceptibility of the given material. Equation (2.6) now becomes

$$\begin{aligned} \tilde{\boldsymbol{D}} &= \varepsilon_0 \tilde{\boldsymbol{E}} + \varepsilon_0 \chi_e \tilde{\boldsymbol{E}} \\ &= \varepsilon_0 (1 + \chi_e) \tilde{\boldsymbol{E}}. \end{aligned} \tag{2.9}$$

The $1 + \chi_e$ term becomes the relative permittivity constant, ε_r, which is related to the static (absolute) permittivity, ε_s, by

$$\varepsilon_r = \frac{\varepsilon_s}{\varepsilon_0} = 1 + \chi_e, \tag{2.10}$$

resulting in the simplified constitutive equation for linear materials,

$$\begin{aligned} \tilde{\boldsymbol{D}} &= \varepsilon_0 \varepsilon_r \tilde{\boldsymbol{E}} \\ &= \varepsilon \tilde{\boldsymbol{E}}. \end{aligned} \tag{2.11}$$

Material	**Permittivity** ε_r	**Permeability** μ_r	**Conductivity** σ
Free Space	1	1	0
Air	1.0006	1.0000004	0
Distilled Water	81	0.999991	10^{-4}
Aluminium	1	1.00002	3.96×10^7
Plywood	2.2	1	0

Table 2.3: Electrical properties for select materials. Similarly to the derivation for the material specific properties, these materials are assumed to be linear and isotropic. [5]

In general, the subscript s is dropped from the permittivity and it is assumed that $\varepsilon \equiv \varepsilon_s$.

A similar formulation is followed for the magnetic polarization vector where $\tilde{\boldsymbol{M}}$ is expressed as $\tilde{\boldsymbol{M}} = \chi_m \tilde{\boldsymbol{H}}$ allowing equation (2.7) to become

$$\begin{aligned} \tilde{\boldsymbol{B}} &= \mu_0 \left(\tilde{\boldsymbol{H}} + \chi_m \tilde{\boldsymbol{H}} \right) \\ &= \mu_0 (1 + \chi_m) \tilde{\boldsymbol{H}}, \end{aligned} \tag{2.12}$$

where χ_m is the magnetic susceptibility term. As with the permittivity, the $1 + \chi_m$ term becomes the relative permeability term, μ_r, which is related to the static (absolute) permeability term, μ_s, by

$$\mu_r = \frac{\mu_s}{\mu_0} = 1 + \chi_m, \tag{2.13}$$

resulting in the simplified constitutive equation for linear materials,

$$\begin{aligned} \tilde{\boldsymbol{B}} &= \mu_0 \mu_r \tilde{\boldsymbol{H}} \\ &= \mu \tilde{\boldsymbol{H}}. \end{aligned} \tag{2.14}$$

Similarly to the permittivity, the subscript s is dropped from the notation.

Non-linear and anisotropic properties of materials can be simulated but are beyond the scope of this background introduction.

2.1.1 Typical Numerical Methods for EM

In ideal situations, a given wave propagation problem would be solved analytically using the equations mentioned in the previous section. However, in practice this becomes impossible as even a simple problem becomes complicated when several interfering objects are included. Therefore, some methods that provide good approximations of the analytical solution have been created.

Computational electromagnetics have two primary techniques for electromagnetic simulation: (i) finite element techniques (FE) and (ii) the finite-difference time-domain method (FDTD). Both techniques have been thoroughly investigated over the years and both have their advantages. The finite element technique is well implemented in the commercial package FEMLAB provided by Comsol [19]. The FDTD method is well documented in several texts including Taflove [62] and Kunz et al. [41].

2.1.1.1 The Finite Difference Time Domain Method

The first computational method developed for wave propagation using Maxwell's equations is the Finite-Difference Time-Domain (FDTD) method. The method was developed by Yee in 1966 [72]. The algorithm steps through discretized space and time to solve for the electric and magnetic fields generated by a scatterer[3] under the influence of incoming EM waves or from a radiating source that may exist in the region of interest. Originally for an isotropic medium, the algorithm has been improved to handle an assortment of materials including conductive ones [61].

The FDTD method has been developed for one-dimensional, two-dimensional and three-dimensional forms, but for simplicity here, the two-dimensional problem for the transverse magnetic case will be discussed as found in Yee [72]. The finite difference equations for the transverse magnetic case are

[3] A scatterer is an object that can reflect or absorb the electromagnetic energy impinged on the object.

$$E_z^{n+1}(i,j) = E_z^n(i,j) + \frac{\Delta t}{\epsilon_0 \Delta x}\left[H_y^{n+\frac{1}{2}}(i+\tfrac{1}{2},j) - H_y^{n+\frac{1}{2}}(i-\tfrac{1}{2},j)\right] - \frac{\Delta t}{\epsilon_0 \Delta y}\left[H_x^{n+\frac{1}{2}}(i,j+\tfrac{1}{2}) - H_x^{n+\frac{1}{2}}(i,j-\tfrac{1}{2})\right], \quad (2.15)$$

$$H_y^{n+\frac{1}{2}}(i,j+\tfrac{1}{2}) = H_y^{n-\frac{1}{2}}(i,j+\tfrac{1}{2}) - \frac{\Delta t}{\epsilon_0 \Delta y}\left[E_z^n(i,j+1) - E_z^n(i,j)\right], \quad (2.16)$$

$$H_x^{n+\frac{1}{2}}(i+\tfrac{1}{2},j) = H_y^{n-\frac{1}{2}}(i+\tfrac{1}{2},j) - \frac{\Delta t}{\epsilon_0 \Delta x}\left[E_z^n(i+1,j) - E_z^n(i,j)\right], \quad (2.17)$$

where n denotes the time step for time point $n\Delta t$ and (i,j) represent the discretized spatial positions for position $(i\Delta x, j\Delta y)$. The "half-steps" are used to update the overlapping electric and magnetic fields. That is, the magnetic fields are updated on the $\frac{1}{2}$ time and space steps while the electric fields are updated on the full time and space steps. Useful diagrams for both the two-dimensional case and the three-dimensional case are given in Sullivan [61]. To solve for the electric and magnetic fields, the algorithm steps through each time and spatial step updating the equations and variables at each step.

The FDTD method as presented by Yee has a weakness at the boundaries of the simulation region because without any boundary conditions outgoing waves will reflect at the boundary and continue to propagate throughout the region instead of continuing outwards. Several methods have been investigated to absorb the outgoing waves but the most popular and robust is clearly Berenger's perfectly matched layers (PML) for absorbing boundary conditions [8, 9]. Berenger's PML method uses the permeability and permittivity properties together to cause propagating waves to cancel at the edges.

As with most numerical problems the temporal and spatial discretizations need to follow the Nyquist criteria,

$$\Delta t \leq \frac{T}{2} \quad (2.18)$$

$$\Delta x \leq \frac{\lambda}{2} \quad (2.19)$$

where Δt is the temporal step, Δx is the spatial step, T is the largest signal period and λ is the smallest signal wavelength.

The FDTD method has been used and is heavily documented in the literature. However, its use is limited to spatial discretizations that are uniformly spaced in rectangular patterns along the x, y, z axes. Therefore, it is very difficult to model situations with curved surfaces and other complicated objects. Fortunately, with the increased capabilities of computers another method, the finite element method, has become quite popular.

2.1.1.2 The Finite Element Method

The finite element method is similar to the FDTD method in that the electromagnetic fields are propagated through a discretized volume. However, the main difference between the two is that the mesh generated for the finite element method is unstructured versus the structured mesh that is required for the FDTD method. That is, in the FDTD method, the mesh that is used to approximate the geometry has nodes that are uniformly spaced. The spacing can differ in each spatial dimension but should remain at constant intervals for a given direction. In the finite element method, the mesh can be unstructured where the nodes can be placed non-uniformly throughout the simulation region. The nodes are connected using a method called tetrahedralization which forms the *finite elements* [27]. This is the fundamental advantage that the finite element method has.

Clearly, by the introduction to this thesis in Chapter 1 the finite element method has been selected. Details of how the simulation has been developed are given in Chapter 3 and therefore the discussion here is kept brief.

2.1.2 Software Application Tools

When developing a simulation of this type the selection of the software tool has one main criteria: Does the user develop the code from scratch or does the user enlist the assistance of a pre-existing tool?

In order to speed the development of the simulation a pre-existing tool, FEMLAB 3.1 [19], was selected. FEMLAB 3.1 is a general partial differential equation solver that uses the finite element as its numerical approximation. FEMLAB 3.1 allows the user to model several different types of systems and even includes a set of specialized modules for electromagnetics, continuum mechanics, fluid dynamics and heat transfer.

Other software packages that were considered included Ansys' Electromagnetics package [2] and Ansoft's Maxwell package [1]. However, due to software availability and cost, FEMLAB proved to be the appropriate choice for this thesis.

2.2 Methods of Position Determination

There exist three general methods of position determination: (i) triangulation, (ii) articulated devices and (iii) parameter estimation. The following sections describe some of the methodologies used to determine the position of a given target.

2.2.1 Triangulation

Triangulation is the most common method used to determine the position of an object without being in direct contact with the object. The global positioning system (GPS) is likely the most well known system that uses triangulation but there exist several others including those that are based on optics and magnetics [3, 45, 50]. The following sections summarize the variations of the most common triangulation methods,

- Intensity Based or Received Signal Strength,
- Time of Flight,
- Time Difference of Arrival,
- Intersection of Planes and
- Intersection of Lines.

2.2.1.1 Intensity Based Method

The intensity based method, also known as the received signal strength method, can take on two configurations. The first configuration consists of a single transmitting isotropic marker with three or more isotropic receiving reference sensors while the second configuration is the inverse of the first, i.e., three transmitting reference sensors and one receiving marker. Considering the first configuration, given the transmitted intensity or power, the intensity received (received signal strength) is deemed to be related to the distance travelled by the

signal. The position is then determined by the intersection of three spheres where the distance is the radius of the sphere and the position of the center of the spheres is the pre-determined positions of the reference sensors.

Bahl and Padmanabhan at Microsoft Research was investigating this method as an add-on feature to their wireless networking systems for context sensitive computing [4]. Bahl and Padmanabhan showed the results for a system that tracks the position of a wireless PDA throughout the second floor of their research facility. Bahl and Padmanabhan placed three base stations throughout the floor with 50 rooms covering 980m^2 and recorded the signal strength received at each base station from the PDA. However, instead of using the triangulation method above they implemented a nearest neighbour parameter estimation algorithm based on a set of measurements from several known locations. This algorithm was important because it was discovered that objects in the field have a significant effect on the measurement accuracy. The algorithm allowed for signals to be attenuated as signals passed through walls and furniture, since the nearest neighbour algorithm characterized the space of interest. Unfortunately, human bodies attenuate the signals significantly, and test subjects holding the PDA found that their position changed drastically simply by changing their orientation. Therefore, in a dynamic office environment, laboratory, or operating room, human bodies will significantly affect the measurement accuracy and will not be appropriate for the applications sought in this thesis. However, this method will continue to be useful as wireless networking progresses and the signal strength is readily available. Hightower and Borriello provide an interesting discussion on the use of location systems in ubiquitous computing[4] [31].

2.2.1.2 Time of Flight

The time of flight (TOF) method is the fundamental technique in global positioning systems (GPS). There are a few different global positioning systems including the European Union's GALILEO system and the Russian GLONASS system but the American NAVSTAR system is the system typically referred to as GPS [30] and will be the one considered here.

The methods used to determine position using GPS are well known [39, 47, 48, 63, 71]. The sensors that make up the GPS components consist of a set of satellites transmitting their current locations (ephemerides, $\bar{\boldsymbol{s}}_i$) used as reference positions and a ground receiver

[4]Ubiquitous computing is also referred to as context sensitive information systems.

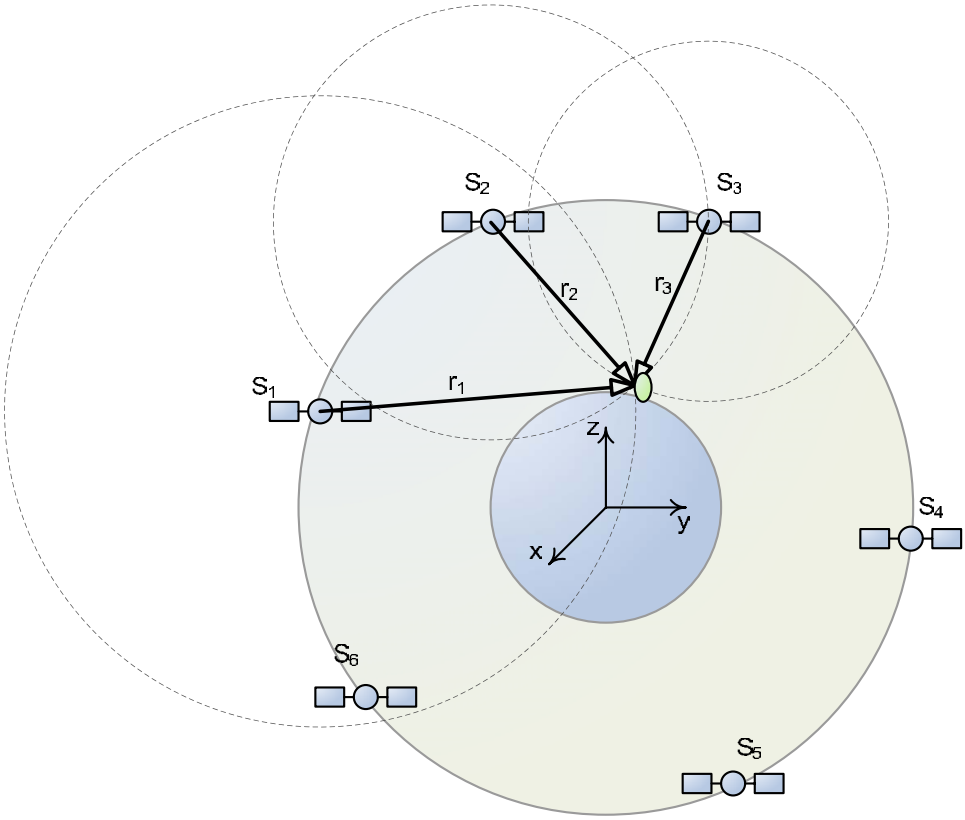

Figure 2.1: This figure is a simple representation of a how a GPS system determines the 3D position of a GPS receiver on the earth's surface. Shown here is a GPS receiver (oval) on the earth's surface with six satellites ($S_1, S_2, S_3, S_4, S_5, S_6$) orbiting the earth at a constant altitude. With a known clock offset, GPS systems are based on using the time of flight to determine the range distances between the GPS receiver and at least three of the satellites, (r_1, r_2, r_3). If the positions of the satellite are known in the a coordinate reference frame ($\bar{\boldsymbol{s}}_1$, $\bar{\boldsymbol{s}}_2$, $\bar{\boldsymbol{s}}_3$), say earth-fixed coordinate frame, then the position of the receiver ($\bar{\boldsymbol{p}}_{rec}$) can be determined by solving for the intersection of the three spheres. Here a sample network of 6 GPS satellites is shown, but the true GPS network is composed of 24 satellites. Also, the solution can be made robust by using more than three satellites, but typically four satellites are used to take into account the effect of the clock offset between the satellites and the ground receiver.

that determines its own position based on the satellite transmissions. The position determination is similar to the intensity based systems where the intersection of three or more spheres provides the location of the receiver as shown in Figure 2.1. However, instead of using the intensity to resolve the range the time of flight is determined by calculating the phase of a pseudo random number (PRN) signal modulated onto the satellite carrier signal. The PRN signal has a cyclical pattern with a period of up to one week. The time of flight is then related easily to the range by,

$$r_i = c_0 \cdot t_i, \tag{2.20}$$

where r_i is the distance to satellite i, c_0 is the speed of light (approximately 3×10^8 m/s) and t_i is the time of flight for satellite i. With the range known to a minimum set of four satellites the position of the receiver is determined by solving the nonlinear set of equations given by

$$\sqrt{(\bar{\boldsymbol{p}}_{rec} - \bar{\boldsymbol{s}}_i) \cdot (\bar{\boldsymbol{p}}_{rec} - \bar{\boldsymbol{s}}_i)} + c_0 \cdot \Delta t = r_i, \quad \text{for } i = 1 \ldots N. \tag{2.21}$$

In this set of equations there are four unknowns, the three vector components of the receiver position $\bar{\boldsymbol{p}}_{rec}$ and the unknown clock offset of the receiver Δt[5]. A solution can be found for $N \geq 4$ satellites using a given nonlinear systems of equation solver such as a least squares method.

Clearly, the GPS system is not that simple as there are corrections needed for atmospheric interference and algorithms needed for tracking and signal lock. However, that discussion is beyond the scope of this background review.

In general, the difficulties with time of flight calculations are two-fold (i) the resolution and (ii) the effect of multipath signals caused by the reflection of the RF signals. With typical GPS applications a measurement within even 50 meters is acceptable. However, as the system is reduced to a localized configuration, the time of flight needs to be resolved to the picosecond level for sub-millimeter or even millimeter accuracy. The technology required to resolve to this level is still in development. However, the more significant issue

[5]The clocks used in the satellites and receiver are not precisely synchronized, therefore, there will always be a small clock offset between the satellites and the receivers. This additional variable, Δt, will compensate for this unknown difference.

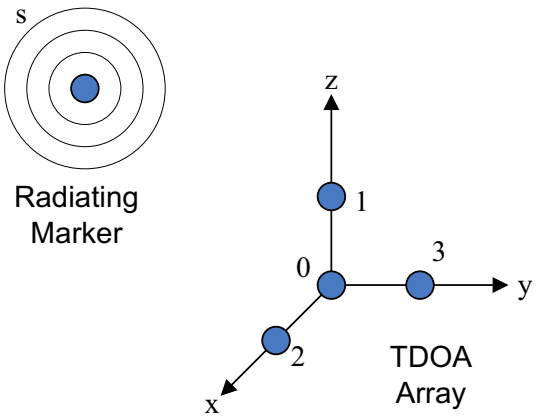

Figure 2.2: Example of time difference of arrival method. A 3+1 configuration with the reference sensor located at the origin is shown with a single radiating source marker.

is the ability to handle multipath signals caused by objects in the field unknown to the GPS system model. Hence, GPS is nearly impossible indoors and in dense urban areas that are inherently multipath environments. This same effect occurs with the local position measurement system and can in fact be more significant as the environment is naturally composed of objects that will reflect the RF signals.

2.2.1.3 Time Difference of Arrival

The time difference of arrival (TDOA) technique is a variation on the time of flight technique. In this method, four or more antennas are used to receive signals from a given transmitting marker. The time delay between the given pairs of antennas are used to determine a heading or direction. For N antennas there are $\binom{N}{2}$ headings (time delays) that can be computed. The intersection of the headings is determined by solving a set of conic equations (typically hyperbolic) [16, 29, 73].

Figure 2.2 has a diagram for an example time difference of arrival method. Here a $3+1$ sensor system is depicted where a source marker s emits a signal that impinges on the array of receiving sensors $a_i, i = 0, 1, 2, 3$. The a_0 sensor is designated as the reference sensor and is defined to be located at the origin of the coordinate frame. The locations of the sensor arrays are then defined in equation 2.22.

$$\bar{\boldsymbol{p}}_0 = \begin{bmatrix} x_0 \\ y_0 \\ z_0 \end{bmatrix} = \begin{bmatrix} 0 \\ 0 \\ 0 \end{bmatrix}, \quad \bar{\boldsymbol{p}}_i = \begin{bmatrix} x_i \\ y_i \\ z_i \end{bmatrix} \quad i = 1, 2, 3 \tag{2.22}$$

The location of the source signal is represented by

$$\bar{\boldsymbol{p}}_s = \begin{bmatrix} x_s \\ y_s \\ z_s \end{bmatrix}. \tag{2.23}$$

The time differences are taken with respect to the reference sensor a_0 and can be determined by a few different methods including the phased lock loop [65] or a cross-correlation technique [73]. The time differences are represented mathematically to be

$$\Delta t_i = t_i - t_0 \quad i = 1, 2, 3 \tag{2.24}$$

where t_0 is the absolute time of arrival at sensor a_0 and t_i is the absolute time of arrival at sensor a_i. Note that the absolute times of arrival are not actually determined and only the difference Δt_i is computed.

The range difference d_i is the difference in distance travelled by the radiating signal to sensor a_i relative to sensor a_0 and is computed using the speed of light.

$$d_i = c\Delta t_i \quad i = 1, 2, 3 \tag{2.25}$$

The range differences d_i are also related to the difference in the Euclidean distance of the source from sensor a_i and the Euclidean distance of the source from the reference sensor a_0.

$$d_i = \sqrt{(x_i - x_s)^2 + (y_i - y_s)^2 + (z_i - z_s)^2} - \sqrt{x_s^2 + y_s^2 + z_s^2} \quad i = 1, 2, 3 \tag{2.26}$$

Rearranging equation 2.26 results in

$$x_i x_s + y_i y_s + z_i z_s + d_i \sqrt{x_s^2 + y_s^2 + z_s^2} = \frac{1}{2}\left(x_i^2 + y_i^2 + z_i^2 - d_i^2\right) \quad i = 1, 2, 3 \tag{2.27}$$

which results in three non-linear equations and three unknowns. A closed-form method for solving this system of equations is presented in Mellen et al. [29]. The algorithm in Mellen is for an $N+1$ sensor system which suggests that the above equations can be easily expanded to handle more than four sensors which provides redundancy in the system computations. Further, Mellen has suggested that a weighting matrix can be added to the algorithm to assist in providing robust measurement based on *a priori* statistics.

As with some of the other methods presented here the line of sight is of issue. However, it may be realistic to assume that most of the path lines travelled by the signals from source to receiver have similar obstructions and resulting in the headings being accurately computed for each sensor pair provided that the receivers are sufficiently close to one another.

2.2.1.4 Intersection of Planes

Another method for triangulation is the intersection of planes shown in Figure 2.3. In this method, a set of planes is defined at n sensors by

$$A_i x + B_i y + C_i z + D_i = 0 \qquad \text{for } i = 1 \ldots N, \tag{2.28}$$

where $N = 3$ for a direct solution and $N > 3$ for an over-determined set of equations. The position of the marker source is found by solving the set of linear equations for x, y and z.

For the Optotrak shown in Figure 2.3, the sensors are linear infrared CCD sensors, however any configuration where a plane is defined through a variable centroid and a known reference location can be used to define a plane.

The coefficients for equation 2.28 for the $N = 3$ Optotrak system are generated by two vectors:

- a vector that is perpendicular to both the line formed by the CCD array and principle viewing direction (z-axis) and
- a vector that passes through both the centroid formed on the CCD and the effective focal point of the lens system.

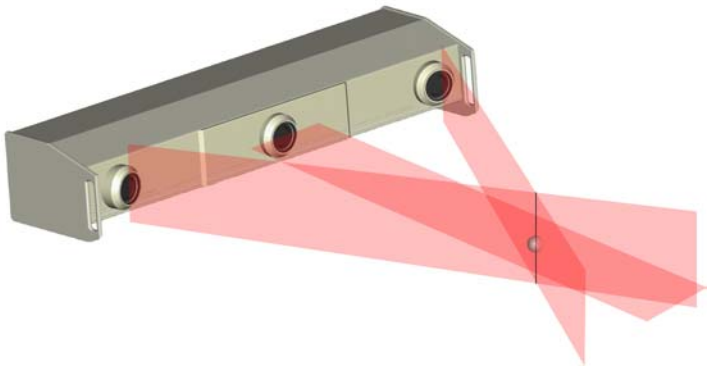

Figure 2.3: Triangulation method using intersection of planes. This method is shown here using the Optotrak from Northern Digital [45]. In this case the Optotrak uses three linear CCD arrays which can define a set of planes that pass through the effective focal point of the lenses and the centroid formed on the given CCD array by the focused light from the marker, e.g., a light emitting diode. The location of the marker is located at the intersection of the three planes. Image courtesy of Northern Digital Inc.

2.2.1.5 Intersection of Lines

The intersection of lines method is similar to that of the intersecting planes except that N lines are defined for at least $N = 2$ sensors. The lines are not independently determined as they are generated by finding the intersection of two planes using a two-dimensional sensor array.

In an optical system, the light emitted or reflected from a marker of interest is captured on a two-dimensional CCD array. A weighted centroid algorithm determines the horizontal (x_a) and vertical (y_a) coordinates of the object on the image captured by the array. Each coordinate (x_a, y_a) defines a plane that passes through it and the focal point similar to that shown in Figure 2.3 and equation 2.28. The intersection of these two planes allows the calculation of the equation of a line in parametric form,

$$\bar{\boldsymbol{p}}_i = \bar{\boldsymbol{p}}_{0i} + t\hat{\boldsymbol{p}}_{0i} \qquad \text{for } i = 1 \ldots N, \tag{2.29}$$

where $\bar{\boldsymbol{p}}$ is the vector representing the coordinates on a line, $\bar{\boldsymbol{p}}_0$ is a point defined on the line, $\hat{\boldsymbol{p}}_0$ is a vector defining the direction of the line and t is a parameter defining a position on the line.

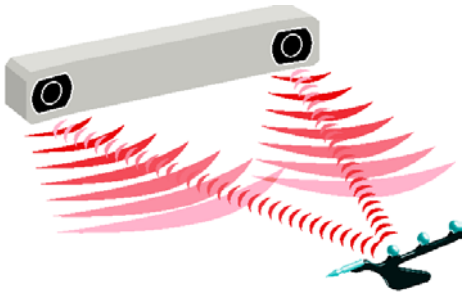

Figure 2.4: Triangulation method using intersection of lines. This method is shown here using the Polaris from Northern Digital [45]. In this case the Polaris uses two area CCD arrays which each define a line that passes through the effective focal point of the lenses and the centroid formed on the CCD sensor. The location of the marker, e.g. a light emitting diode or retro-reflective sphere, is at the intersection of the two lines. Image courtesy of Northern Digital Inc.

In a perfectly defined system, all of the lines should intersect at the marker location. In reality, the position of the marker is found by an optimization procedure that finds the position of the marker in the region where the lines are closest to one another. A graphical example of a reflected marker is shown in Figure 2.4. Details of finding the nearest points between two lines is given in Section 5.1.2 on page 95.

2.2.2 Articulated Devices

Articulated measurement devices are a collection of joined segments where the relative position or orientation at the joints is precisely measured. In general, the sensors are either linear encoders or angular encoders where a collection of rigid links and joints are placed in a open loop linkage. The sensed positions are then input into a model of the mechanical linkage which determines the position of the end tip by propagating all the sensor positions through the model.

In general, these systems can be awkward and difficult to use because they are rigidly attached to their base and the linkages need to be manipulated to place the measured tip at the desired location to be measured. Faro [28] and Romer [53] each provide articulated

arms for various industrial and miscellaneous digitizing needs. Although very accurate, the awkwardness of the articulated arm is disliked by medical personnel because it can block other medical equipment and is impractical for gait researchers because it will actually inhibit the subjects gait.

2.2.3 Black Box Modelling

In some position measurement systems, the physical models can be so complicated that the data collected at the sensors do not match the models closely enough to be used in high accuracy situations. Therefore, in order to create accurate measurements, generalized models are introduced. The intensity based method using the nearest neighbor method in Section 2.2.1 could also be implemented using a black box model. Black box modelling can also be used as a correction model to already well established spatial measurement models. For example, systematic errors in the system that cannot be related to the physical model can be corrected using the black box model determined at the time of system characterization[6].

These models are typically high-order polynomials where the polynomial coefficients are dependent on the system of measurement. For example, for a system with N sensors that are position dependent, the following polynomial shown to 3rd order can be created.

$$x = \phi_0^x + \sum_{i=1}^{N} \phi_i^x s_i + \sum_{i=1}^{N}\sum_{j\geq i}^{N} \phi_{i,j}^x s_i s_j + \sum_{i=1}^{N}\sum_{j\geq i}^{N}\sum_{\substack{k\geq i\\ k\geq j}}^{N} \phi_{i,j,k}^x s_i s_j s_k + \dots \tag{2.30}$$

$$y = \phi_0^y + \sum_{i=1}^{N} \phi_i^y s_i + \sum_{i=1}^{N}\sum_{j\geq i}^{N} \phi_{i,j}^y s_i s_j + \sum_{i=1}^{N}\sum_{j\geq i}^{N}\sum_{\substack{k\geq i\\ k\geq j}}^{N} \phi_{i,j,k}^y s_i s_j s_k + \dots \tag{2.31}$$

$$z = \phi_0^z + \sum_{i=1}^{N} \phi_i^z s_i + \sum_{i=1}^{N}\sum_{j\geq i}^{N} \phi_{i,j}^z s_i s_j + \sum_{i=1}^{N}\sum_{j\geq i}^{N}\sum_{\substack{k\geq i\\ k\geq j}}^{N} \phi_{i,j,k}^z s_i s_j s_k + \dots \tag{2.32}$$

The positions (x, y, z) are found by relating the sensor signals $(s_i, i = 1 \dots N)$ and model coefficients (ϕ). The model coefficients are determined through experiments where the marker is placed in many known locations and the sensor measurements are recorded.

[6]The term characterization is often replaced with the term calibration[68].

A least squares algorithm (see section A.4) can then be used to estimate the coefficients that can be then used in practical situations.

This method is fundamentally an alternative method to the nearest neighbour method presented by Bahl et al. [4] discussed earlier in the intensity based methods. Instead of using a physical model that relates the signal attenuation to the distance R, the intensity of the signal can be used in the polynomial model and position can be determined in alternative manner.

Chapter 3

Model Development for Signal Transmission and Receipt

In general, models are used to simulate the real world, often over a given period of time. The theoretical model developed here is no different. In fact, the conceptual design of the model is highly simplified but the implementation is complicated. Figure 3.1 provides a conceptual schematic of the system. In this model the radiation from a source marker is propagated throughout a region of interest. The region of interest may be modelled both with the region empty and with reflecting and attenuating objects present in the volume. The signals collected at the sensor array will be processed and various position determination algorithms can be tested. The actual implementation involves solving Maxwell's equations using a numerical method because solving the equations using analytical methods is difficult. Therefore, the remainder of this chapter describes the details of the model developed.

The model is divided into three distinct components with each one being implemented separately in phases as illustrated in Figure 3.2. In phase 1, the system domain model is developed in terms of electromagnetic radiation and its propagation throughout space and time. Fundamentally, the system consists of a transmitter and a set of receivers that interact over a given space. The issue of interest is how objects unknown to the sensor system in the surrounding space affect this interaction since the desired accuracy of the system is highly dependent on the ability to reduce the effects of the radio frequency signals that are

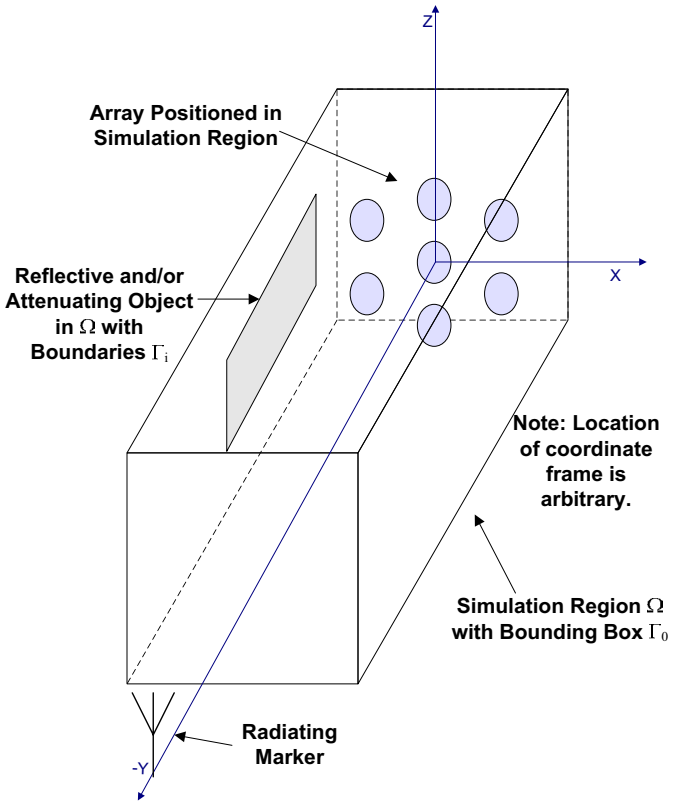

Figure 3.1: Conceptual schematic of the physical configuration for the model region. Using the finite element method in FEMLAB, an input signal is applied to the boundary intersected by the positive y-axis. The signal will then propagate through the volume towards the array. The signals received at the arrays will be processed and phased array techniques will be used to determine the position of the source signal. Studies will be performed with both the free space condition and with objects in the region that both reflect and attenuate the signal.

reflected or attenuated. In phase 2, the conversion from a line signal[1] on the electronics and antennas to electromagnetic space are modelled in order to provide the appropriate input to the radiation model developed in phase 1. Phase 3 involves developing the signal processing and position determination algorithms in order to determine an accurate 3D position. The input into this portion of the simulation is the signal received from the antenna models developed in phase 2.

Figure 3.2 shows a block diagram of the model would be used during simulation. Each part of the model is identified with respect to the phase that portion of the simulation will be developed. Phases 1 and 2 are discussed in the following sections while phase 3 is introduced in Chapter 5.

3.1 Governing Equations for Electromagnetic Propagation

Simulating the propagation of electromagnetic waves through space can be described as a boundary value problem (BVP) [10, 36]. That is, a set of partial differential equations describe the behaviour of the vector field in a volume based on the conditions posed on the boundaries that truncate space to a finite region. Here, the partial differential equations that govern the volume Ω are Maxwell-Ampere's Law 2.1 and Faraday's Law 2.2 from section 2.1 where the flux density and current density variables can be eliminated by substituting in the constitutive equations 2.8, 2.11 and 2.14.[2]

$$\left.\begin{aligned} \nabla \times \tilde{\boldsymbol{H}} &= \sigma \tilde{\boldsymbol{E}} + \varepsilon \frac{\partial \tilde{\boldsymbol{E}}}{\partial t} \\ \nabla \times \tilde{\boldsymbol{E}} &= -\mu \frac{\partial \tilde{\boldsymbol{H}}}{\partial t} \end{aligned}\right\} \quad \in \Omega \tag{3.1}$$

Recall that the material properties are the permittivity ($\varepsilon = \varepsilon_r \varepsilon_0$), the permeability ($\mu = \mu_r \mu_0$) and the conductivity ($\sigma$) where in free space $\varepsilon_r = \mu_r = 1$, $\sigma = 0$.

[1] The line signal is not to be confused with the *line source* presented later in this chapter and Chapter 4. The line signal is the signal generated by the transmitter electronics or received at the receiver antenna. The line signal is usually measured in volts.

[2] Note: It is assumed that the materials of interest are linear materials and the linear simplifications of the constitutive relations can be used.

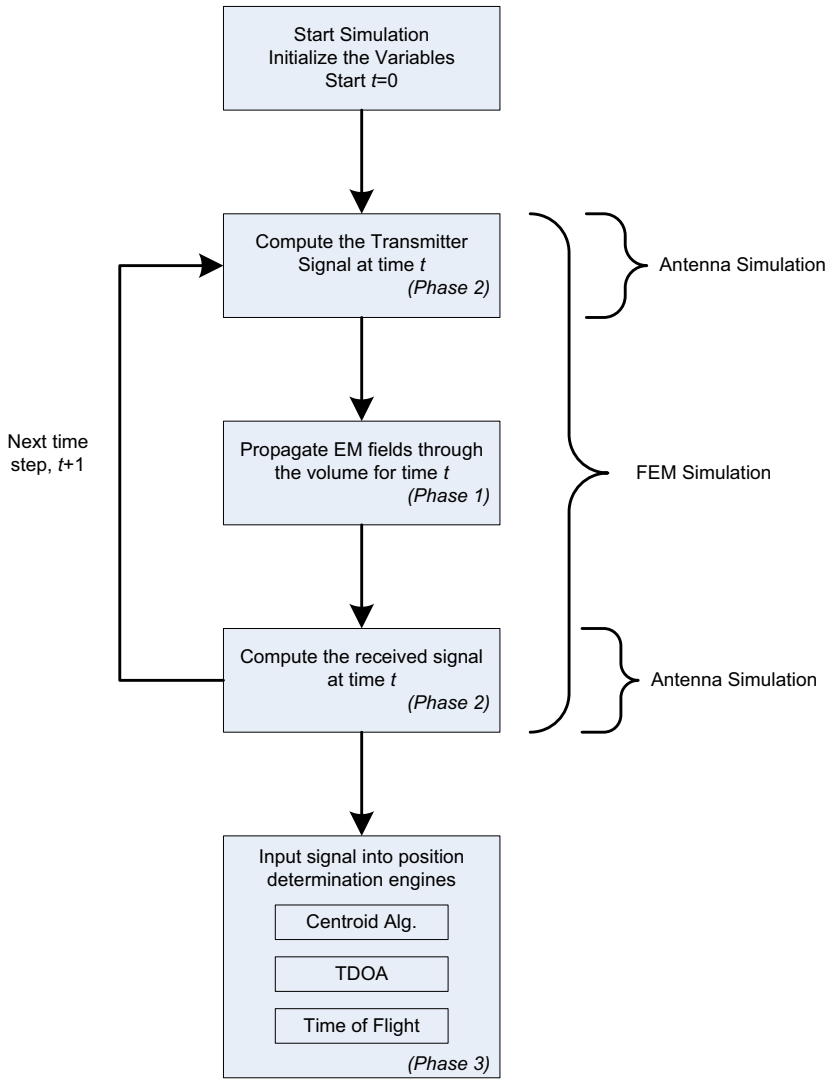

Figure 3.2: Process Diagram for the model framework during simulation. Phase 1 involves propagating the radio frequency energy from a source through the volume of interest. An important part of phase 1 is in the development of a volume truncation technique that allows the boundaries to act as if they were located at infinity (see section 3.2.4). Phase 2 sees the development of the input signal either by a current source on the active area of an antenna or by using the Dirichlet condition that defines the EM field for an antenna located outside of the volume (see section 3.3). Finally, the development and testing of position determination algorithms are part of phase 3. Phases 1 and 2 are discussed at length in this chapter, but phase 3 is introduced in Chapter 5.

The boundary conditions are divided into two sets. First, the internal boundaries Γ_i use the boundary continuity equations to transmit the electromagnetic fields from one medium (denoted as the positive side) to a second medium (denoted as the negative side). This is accomplished by ensuring that the tangential electric and magnetic fields are equal on both sides of the boundary.

$$\left.\begin{aligned} \hat{\boldsymbol{n}} \times \left(\tilde{\boldsymbol{E}}^{+} - \tilde{\boldsymbol{E}}^{-} \right) = 0 \\ \hat{\boldsymbol{n}} \times \left(\tilde{\boldsymbol{H}}^{+} - \tilde{\boldsymbol{H}}^{-} \right) = 0 \end{aligned} \right\} \quad \in \Gamma_i \tag{3.2}$$

The exterior boundary conditions are truncating boundaries and are required to absorb any electromagnetic propagation as if the boundaries extended to infinity. The finite element formulation naturally reflects any wave impinging on the boundary that is not aligned with the normal direction of the boundary. Unfortunately, complete absorption is nearly impossible because their is not one boundary condition that is effective for absorbing waves impinging the boundary from all directions [36]. However, a low reflection absorbing boundary condition [20] can be described by

$$\sqrt{\frac{\mu}{\varepsilon}} \hat{\boldsymbol{n}} \times \tilde{\boldsymbol{H}} + \tilde{\boldsymbol{E}} - \left(\hat{\boldsymbol{n}} \cdot \tilde{\boldsymbol{E}} \right) \hat{\boldsymbol{n}} = 2\tilde{\boldsymbol{E}}_0 - 2 \left(\hat{\boldsymbol{n}} \cdot \tilde{\boldsymbol{E}}_0 \right) \hat{\boldsymbol{n}} + 2\sqrt{\frac{\mu}{\varepsilon}} \hat{\boldsymbol{n}} \times \tilde{\boldsymbol{H}}_0 \quad \in \Gamma_0, \tag{3.3}$$

where $\tilde{\boldsymbol{E}}_0$ and $\tilde{\boldsymbol{H}}_0$ are input fields that occur on the boundary [20, 36]. This boundary condition balances the tangential magnetic field ($\hat{\boldsymbol{n}} \times \tilde{\boldsymbol{H}}$) and the transverse electric field ($\tilde{\boldsymbol{E}} - \left(\hat{\boldsymbol{n}} \cdot \tilde{\boldsymbol{E}} \right) \hat{\boldsymbol{n}}$)[3]. The boundary condition sets the tangential magnetic field and the transverse electric field equal to their associated input fields which are typically zero everywhere except at the input boundaries. This absorbing boundary condition is exact for waves with the Poynting vector ($\tilde{\boldsymbol{S}} = \tilde{\boldsymbol{E}} \times \tilde{\boldsymbol{H}}$) aligned with the boundary normal direction and is only approximately absorbed for waves that travel in a direction other than the normal direction of the boundary. The reflection coefficient can be computed as a function of the angle that the Poynting vector forms with the normal direction but the reflection coefficient becomes irrelevant when multiple waves are superimposed and impinging at different angles at the same location on the boundary [36].

In general, the boundary value problem can be summarized as shown in Formulation 3.1.

[3]The transverse field can also be written as $\tilde{\boldsymbol{E}} - \left(\hat{\boldsymbol{n}} \cdot \tilde{\boldsymbol{E}} \right) \hat{\boldsymbol{n}} = \hat{\boldsymbol{n}} \times \hat{\boldsymbol{n}} \times \tilde{\boldsymbol{E}}$.

Formulation 3.1 Boundary Value Problem for Maxwell's Equations

$$\left.\begin{aligned} \nabla \times \tilde{\boldsymbol{H}} &= \sigma \tilde{\boldsymbol{E}} + \varepsilon \frac{\partial \tilde{\boldsymbol{E}}}{\partial t} \\ \nabla \times \tilde{\boldsymbol{E}} &= -\mu \frac{\partial \tilde{\boldsymbol{H}}}{\partial t} \end{aligned}\right\} \quad \in \Omega$$

$$\left.\begin{aligned} \hat{\boldsymbol{n}} \times \left(\tilde{\boldsymbol{E}}^{+} - \tilde{\boldsymbol{E}}^{-} \right) &= 0 \\ \hat{\boldsymbol{n}} \times \left(\tilde{\boldsymbol{H}}^{+} - \tilde{\boldsymbol{H}}^{-} \right) &= 0 \end{aligned}\right\} \quad \in \Gamma_i$$

$$\sqrt{\frac{\mu}{\varepsilon}} \hat{\boldsymbol{n}} \times \tilde{\boldsymbol{H}} + \tilde{\boldsymbol{E}} - \left(\hat{\boldsymbol{n}} \cdot \tilde{\boldsymbol{E}} \right) \hat{\boldsymbol{n}} = 2\tilde{\boldsymbol{E}}_0 - 2 \left(\hat{\boldsymbol{n}} \cdot \tilde{\boldsymbol{E}}_0 \right) \hat{\boldsymbol{n}} + 2\sqrt{\frac{\mu}{\varepsilon}} \hat{\boldsymbol{n}} \times \tilde{\boldsymbol{H}}_0 \quad \in \Gamma_0$$

3.1.1 Wave Equation Formulation Derivation

In general, it is preferred to solve for a single vector field, i.e., electric field intensity ($\tilde{\boldsymbol{E}}$), magnetic field intensity ($\tilde{\boldsymbol{H}}$), electric flux density ($\tilde{\boldsymbol{D}}$) or magnetic flux density ($\tilde{\boldsymbol{B}}$). In this simulation, the variable of interest is the electric field intensity because the electric field is used to determine the voltage signal generated at the antenna ports. Therefore, in order to simplify the solution of Maxwell's equations, the equations need to be manipulated to isolate the electric field intensity.

The two equations in 3.1 give two coupled partial differential equations with two vector field variables and some material properties. In order to isolate the electric field intensity the curl operator is applied to both sides of Faraday's law, the second equation of 3.1.

$$\nabla \times \left(\nabla \times \tilde{\boldsymbol{E}} \right) = \nabla \times \left(-\mu \frac{\partial \tilde{\boldsymbol{H}}}{\partial t} \right) \tag{3.4}$$

The curl on the right hand side can be taken inside the partial time derivative to get

$$\nabla \times \left(\nabla \times \tilde{\boldsymbol{E}} \right) = -\mu \frac{\partial \left(\nabla \times \tilde{\boldsymbol{H}} \right)}{\partial t}. \tag{3.5}$$

Substitute in Ampere's Law from the first equation of 3.1 into 3.5,

$$\nabla \times \left(\nabla \times \tilde{\boldsymbol{E}} \right) = -\mu \frac{\partial}{\partial t} \left(\sigma \tilde{\boldsymbol{E}} + \varepsilon \frac{\partial \tilde{\boldsymbol{E}}}{\partial t} \right). \tag{3.6}$$

Balanis [5] provides an identity required to simplify the left hand side, $\nabla \times \nabla \times \tilde{\boldsymbol{E}} = \nabla \left(\nabla \cdot \tilde{\boldsymbol{E}} \right) - \nabla^2 \tilde{\boldsymbol{E}}$, to obtain

$$\nabla \left(\nabla \cdot \tilde{\boldsymbol{E}} \right) - \nabla^2 \tilde{\boldsymbol{E}} = -\mu \frac{\partial}{\partial t} \left(\sigma \tilde{\boldsymbol{E}} + \varepsilon \frac{\partial \tilde{\boldsymbol{E}}}{\partial t} \right). \tag{3.7}$$

Now from Gauss Electric Law (2.3) and the constitutive relation (2.11) it can be shown that $\nabla \cdot \tilde{\boldsymbol{E}} = \tilde{\boldsymbol{\rho}}/\varepsilon$ by substituting equation 2.11 into equation 2.3. So the equation can be rearranged and the electric charge can be moved to the right hand side.

$$\mu\varepsilon \frac{\partial^2 \tilde{\boldsymbol{E}}}{\partial t^2} + \mu\sigma \frac{\partial \tilde{\boldsymbol{E}}}{\partial t} - \nabla^2 \tilde{\boldsymbol{E}} = \nabla \left(\frac{\rho}{\varepsilon} \right) \tag{3.8}$$

The boundary conditions also need to be reformulated by taking the time derivative of equations having a magnetic term 3.2 and 3.3.

$$\left.\begin{aligned} \hat{\boldsymbol{n}} \times \left(\tilde{\boldsymbol{E}}^{+} - \tilde{\boldsymbol{E}}^{-} \right) &= 0 \\ \hat{\boldsymbol{n}} \times \left(\frac{\partial \tilde{\boldsymbol{H}}^{+}}{\partial t} - \frac{\partial \tilde{\boldsymbol{H}}^{-}}{\partial t} \right) &= 0 \end{aligned}\right\} \quad \in \Gamma_i \tag{3.9}$$

$$\begin{aligned} \sqrt{\frac{\mu}{\varepsilon}} \frac{\partial}{\partial t} \hat{\boldsymbol{n}} \times \tilde{\boldsymbol{H}} + \frac{\partial}{\partial t} \left(\tilde{\boldsymbol{E}} - \left(\hat{\boldsymbol{n}} \cdot \tilde{\boldsymbol{E}} \right) \hat{\boldsymbol{n}} \right) \\ = \frac{\partial}{\partial t} \left(2\tilde{\boldsymbol{E}}_0 - 2 \left(\hat{\boldsymbol{n}} \cdot \tilde{\boldsymbol{E}}_0 \right) \hat{\boldsymbol{n}} \right) + 2\sqrt{\frac{\mu}{\varepsilon}} \frac{\partial}{\partial t} \hat{\boldsymbol{n}} \times \tilde{\boldsymbol{H}}_0 \quad \in \Gamma_0 \end{aligned} \tag{3.10}$$

Moving the time derivatives inside the curl equations and substituting in Faraday's Law from equation 3.1 then the boundary conditions become

$$\left.\begin{aligned} \hat{\boldsymbol{n}} \times \left(\tilde{\boldsymbol{E}}^{+} - \tilde{\boldsymbol{E}}^{-} \right) &= 0 \\ \hat{\boldsymbol{n}} \times \left(\nabla \times \tilde{\boldsymbol{E}}^{+} - \nabla \times \tilde{\boldsymbol{E}}^{-} \right) &= 0 \end{aligned}\right\} \quad \in \Gamma_i, \tag{3.11}$$

$$\sqrt{\frac{1}{\mu\varepsilon}}\hat{\boldsymbol{n}}\times\nabla\times\tilde{\boldsymbol{E}}+\frac{\partial}{\partial t}\left(\tilde{\boldsymbol{E}}-\left(\hat{\boldsymbol{n}}\cdot\tilde{\boldsymbol{E}}\right)\hat{\boldsymbol{n}}\right)$$
$$=\frac{\partial}{\partial t}\left(2\tilde{\boldsymbol{E}}_0-2\left(\hat{\boldsymbol{n}}\cdot\tilde{\boldsymbol{E}}_0\right)\hat{\boldsymbol{n}}\right)+2\sqrt{\frac{1}{\mu\varepsilon}}\hat{\boldsymbol{n}}\times\nabla\times\tilde{\boldsymbol{E}}_0\quad\in\Gamma_0. \quad (3.12)$$

The boundary condition on the outer boundary is often referred to as the matched boundary condition and is also called a mixed boundary condition. This wave equation formulation is summarized in Formulation 3.2.

Formulation 3.2 Wave Equation Boundary Value Problem

$$\mu\varepsilon\frac{\partial^2\tilde{\boldsymbol{E}}}{\partial t^2}+\mu\sigma\frac{\partial\tilde{\boldsymbol{E}}}{\partial t}-\nabla^2\tilde{\boldsymbol{E}}=\nabla\left(\frac{\rho}{\varepsilon}\right)\quad\in\Omega$$

$$\left.\begin{aligned}\hat{\boldsymbol{n}}\times\left(\tilde{\boldsymbol{E}}^{+}-\tilde{\boldsymbol{E}}^{-}\right)=0\\ \hat{\boldsymbol{n}}\times\left(\nabla\times\tilde{\boldsymbol{E}}^{+}-\nabla\times\tilde{\boldsymbol{E}}^{-}\right)=0\end{aligned}\right\}\quad\in\Gamma_i$$

$$\sqrt{\frac{1}{\mu\varepsilon}}\hat{\boldsymbol{n}}\times\nabla\times\tilde{\boldsymbol{E}}+\frac{\partial}{\partial t}\left(\tilde{\boldsymbol{E}}-\left(\hat{\boldsymbol{n}}\cdot\tilde{\boldsymbol{E}}\right)\hat{\boldsymbol{n}}\right)=\frac{\partial}{\partial t}\left(2\tilde{\boldsymbol{E}}_0-2\left(\hat{\boldsymbol{n}}\cdot\tilde{\boldsymbol{E}}_0\right)\hat{\boldsymbol{n}}\right)+2\sqrt{\frac{1}{\mu\varepsilon}}\hat{\boldsymbol{n}}\times\nabla\times\tilde{\boldsymbol{E}}_0\quad\in\Gamma_0$$

This formulation can also be found in the literature in papers by Lee et al.[42] and Carpes Jr. et al. [37]. However, in both cases the authors have generated their own finite element libraries[4] that can be used to test the formulation. In this case, there are some difficulties implementing this formulation using FEMLAB and they are discussed in the next section.

3.1.2 Wave Equation Formulation Implementation

FEMLAB and the finite element method was chosen for the electromagnetic wave propagation simulation as discussed in section 2.1.2. The FEMLAB package is a general partial differential equation solver that uses the finite element method as its numerical solver.

[4]These libraries were not generally available for public use.

Within FEMLAB is a set of specialized application modules including the electromagnetic application mode that allows the user to simply define geometry, material properties and excitations and the program will generate the finite element equations and solve the problem and provide several postprocessing options. However, the FEMLAB electromagnetic application mode has a significant feature missing from the program. The electromagnetic wave mode in FEMLAB 3.1 solves all models in time-harmonic form and not in time-dependent (time-domain) form. That is, all time-varying electromagnetic fields can be reduced to the time-harmonic form [5, 20, 36]. For a single given frequency (ω), the time-varying vector field representing electric field intensity ($\tilde{\boldsymbol{E}}$) can be reduced to a magnitude ($\hat{\mathbf{E}}$) and phase (ϕ) of a sinusoidal signal,

$$\begin{aligned} \tilde{\boldsymbol{E}}(x,y,z,t) &= \hat{\mathbf{E}}(x,y,z)\cos(\omega t+\phi), && (3.13)\\ &= \Re\left(\hat{\mathbf{E}}(x,y,z)\,e^{j(\omega t+\phi)}\right), && (3.14)\\ &= \Re\left(\hat{\mathbf{E}}(x,y,z)\,e^{j\omega t}e^{j\phi}\right). && (3.15) \end{aligned}$$

For the time-harmonic form, the phase term $e^{j\phi}$ can be dropped and a solution is found for $t = 0$ or $\phi = 0$ with equation (3.15) becoming

$$\tilde{\boldsymbol{E}} = \Re\left(\tilde{\mathbf{E}}(x,y,z)\,e^{j\omega t}\right). \quad (3.16)$$

After a solution is found, the phase term can be reincorporated into the solution during postprocessing so that a solution can be described at any point within the time period.

The time-harmonic form is very limiting in terms of the level of detail that can be studied in the analysis. The analysis is limited to a single arbitrarily defined frequency but other draw backs include not being able to study

- the transient behaviour of the system,
- the effect of noisy and data encoded signals and
- the phase difference in the antenna array.

The last item in the above list is critical since this is the fundamental goal of this simulator.

Fortunately, FEMLAB has an alternative method of formulation, equation-based models. The equation-based model mode in FEMLAB simply solves any given partial differential equation (PDE) for the given geometry, parameters (material properties) and excitations. Several solution options exist including solving for a stationary problem, time-harmonic or time-dependent. Therefore, instead of being restricted to the time-harmonic electromagnetic application mode, the simulation can be reformulated from Maxwell's equations into a solvable set of partial differential equations where FEMLAB will be used to solve the equations throughout the domain of interest.

The partial differential equations for the finite element method can be formulated in several different manners, but in typical English language contradictions, the most powerful form is the weak form. The weak form allows for the partial differential equations to be solved by reducing the order of the differential equations and eliminating some of the terms that exist in the strong form listed in Formulation 3.2. Derivation of the weak form is discussed later in this chapter.

In FEMLAB, the partial differential equations that act over the domain Ω can be written in coefficient strong form, generalized strong form, and weak form. In each form the problem is formulated with a partial differential equation that governs the behaviour throughout the volume followed by a generalized Neumann boundary condition[5] and a Dirichlet boundary condition. The Dirichlet boundary conditions specifies the variables on the boundary to be a specified value, while the Neumann boundary condition relates the flux of the variables normal to surface to a specified value.

Coefficient strong form:

$$\begin{aligned} &\boldsymbol{D}_a\frac{\partial\tilde{\boldsymbol{u}}}{\partial t}+\nabla\cdot(-\boldsymbol{c}\nabla\tilde{\boldsymbol{u}}-\boldsymbol{\alpha}\tilde{\boldsymbol{u}}+\boldsymbol{\gamma})+\boldsymbol{\beta}\cdot\nabla\tilde{\boldsymbol{u}}+\boldsymbol{a}\tilde{\boldsymbol{u}}=\bar{\boldsymbol{f}} && \in\Omega \\ &\hat{\boldsymbol{n}}\cdot(\boldsymbol{c}\nabla\tilde{\boldsymbol{u}}+\boldsymbol{\alpha}\tilde{\boldsymbol{u}}-\boldsymbol{\gamma})+\boldsymbol{q}\tilde{\boldsymbol{u}}=\bar{\boldsymbol{g}}-\boldsymbol{H}^T\bar{\boldsymbol{\mu}} && \in\Gamma \\ &\boldsymbol{H}\tilde{\boldsymbol{u}}=\bar{\boldsymbol{r}} && \in\Gamma \end{aligned} \tag{3.17}$$

[5]The generalized Neumann boundary condition is also referred to as a mixed boundary condition.

General strong form:

$$\begin{aligned} \boldsymbol{D}_a \frac{\partial \tilde{\boldsymbol{u}}}{\partial t} + \nabla \cdot \bar{\boldsymbol{\Lambda}} &= \bar{\boldsymbol{f}} && \in \Omega \\ -\hat{\boldsymbol{n}} \cdot \bar{\boldsymbol{\Lambda}} &= \bar{\boldsymbol{g}} + \left(\frac{\partial \bar{\boldsymbol{r}}}{\partial \tilde{\boldsymbol{u}}} \right)^T \bar{\boldsymbol{\mu}} && \in \Gamma \\ \bar{\mathbf{0}} &= \bar{\boldsymbol{r}} && \in \Gamma \end{aligned} \tag{3.18}$$

General weak form:

$$\begin{aligned} 0 = &\int_\Omega \boldsymbol{D}_a \bar{\boldsymbol{v}} \cdot \frac{\partial \tilde{\boldsymbol{u}}}{\partial t} \partial\Omega + \int_\Omega \bar{\boldsymbol{v}} \cdot \left(\nabla \cdot \bar{\boldsymbol{\Lambda}} + \bar{\boldsymbol{f}} \right) \partial\Omega \\ &+ \int_\Gamma \bar{\boldsymbol{v}} \cdot \left(\bar{\boldsymbol{g}} + \left(\frac{\partial \bar{\boldsymbol{r}}}{\partial \tilde{\boldsymbol{u}}} \right)^T \bar{\boldsymbol{\mu}} \right) \partial\Gamma \\ \bar{\mathbf{0}} = &\bar{\boldsymbol{r}} \qquad \in \Gamma \end{aligned} \tag{3.19}$$

In all forms of the partial differential equations, $\tilde{\boldsymbol{u}}$ is the time-varying vector field of interest $\in \mathbb{R}^3$ and the coefficients are described in Table 3.1 as given by the Comsol Modelling Guide [21]. In general, the operators in the forms listed above are tensor operators which are briefly described in Appendix A.1 on page 118. However, for the remainder of this thesis it is assumed that all variables are of the matrix-vector formulation unless otherwise stated.

The coefficient strong form is useful for linear or nearly linear systems where the physical quantities are easily identified in this form. The general strong form allows for a wider range of nonlinear problems as each coefficient can be a function of the time-varying vector field or its spatial derivatives. FEMLAB also provides the functionality that allows one to replace the $\nabla \cdot \bar{\boldsymbol{\Lambda}}$ with a generalized spatial differential operator $\mathcal{L}$ that can be applied to a vector variable $\tilde{\boldsymbol{u}}$ using functional notation $\mathcal{L}(\tilde{\boldsymbol{u}})$ so that more general problems can be formulated. The weak form allows for the generalization of the model so that edge and point contributions can be added to the system in addition to being able to simplify the system of equations. Again, the $\mathcal{L}(\tilde{\boldsymbol{u}})$ operator can be used here. See section 3.2 for more on the weak form and its use in this simulation.

Two difficulties arise from the formulation in equation 3.8. First, the Laplacian of a vector is not present in the first order PDE and the equivalent term must be found. Secondly, this is a second order partial differential equation which does not match the first order PDE in equation 3.17.

Coefficient	Definition
	Coefficient Form
$\boldsymbol{D}_a \equiv$	mass coefficient (matrix)
$\boldsymbol{c} \equiv$	diffusion coefficient (varying order tensor)
$\boldsymbol{\alpha} \equiv$	conservative flux* convection coefficient (varying order tensor)
$\boldsymbol{\gamma} \equiv$	conservative flux* source term (varying order tensor)
$\boldsymbol{\beta} \equiv$	convection coefficient (varying order tensor)
$\boldsymbol{a} \equiv$	absorption coefficient (varying order tensor)
$\bar{\boldsymbol{f}} \equiv$	source term (vector)
$\hat{\boldsymbol{n}} \equiv$	outward unit normal direction on the boundary (vector)
$\boldsymbol{q} \equiv$	boundary absorption coefficient (varying order tensor)
$\bar{\boldsymbol{g}} \equiv$	boundary flux source term (vector)
$\boldsymbol{H} \equiv$	reaction matrix (matrix)
$\bar{\boldsymbol{\mu}} \equiv$	Lagrange multipliers (vector)
$\bar{\boldsymbol{r}} \equiv$	boundary source term (vector)
	General Form
	$\boldsymbol{D}_a, \hat{\boldsymbol{n}}, \bar{\boldsymbol{g}}, \bar{\boldsymbol{r}}$ and $\bar{\boldsymbol{\mu}}$ as in the coefficient form
$\bar{\boldsymbol{\Lambda}} \equiv$	flux term† (vector)
$\bar{\boldsymbol{f}} \equiv$	source term† (vector)
	Weak Form
	$\boldsymbol{D}_a, \bar{\boldsymbol{\Lambda}}, \bar{\boldsymbol{f}}, \bar{\boldsymbol{g}}, \bar{\boldsymbol{r}}$ and $\bar{\boldsymbol{\mu}}$ as in the coefficient form
$\bar{\boldsymbol{v}} \equiv$	basis test function (vector)

Table 3.1: Summary of PDE coefficients for the coefficient, general and weak form in FEMLAB. The definition of the terms are typical names that may not be appropriate for an electromagnetic model, however, the original names are drawn from other fields such as continuum mechanics, fluid dynamics and heat transfer.

*The conservative flux term is the bracketed expression in equation 3.17, $(-(c)\nabla\tilde{\boldsymbol{u}} - \boldsymbol{\alpha}\tilde{\boldsymbol{u}} + \boldsymbol{\gamma})$.

† These terms can be a function of the spatial coordinates (x, y, z), the time-varying field of interest $(\tilde{\boldsymbol{u}})$ or its spatial derivatives $(\nabla\tilde{\boldsymbol{u}}, \nabla\cdot\tilde{\boldsymbol{u}}, \nabla\times\tilde{\boldsymbol{u}}, \nabla^2\tilde{\boldsymbol{u}})$.

For the first issue, by inspection it is clear that there is a second spatial derivative term, specifically $\nabla \cdot (-\boldsymbol{c}\nabla\tilde{\boldsymbol{u}})$ in equations 3.17 or 3.18. Fortunately, it is shown in Appendix B that $-\nabla^2\tilde{\boldsymbol{E}} = \nabla \cdot \left(-\boldsymbol{c}\nabla\tilde{\boldsymbol{E}}\right)$, where $\boldsymbol{c}$ is set to an identity $\in \mathbb{R}^3$.

For the second issue, FEMLAB has a suggested solution which they refer to as the wave extension of the time-dependent solution. The wave extension is just a change of variable technique where two first order PDEs are solved instead of one second order. The problem from equation 3.17 is reformulated to be

$$\boldsymbol{D}_a\frac{\partial\dot{\tilde{\boldsymbol{u}}}}{\partial t} + \nabla \cdot (-\boldsymbol{c}\nabla\tilde{\boldsymbol{u}} - \boldsymbol{\alpha}\tilde{\boldsymbol{u}} + \boldsymbol{\gamma}) + \boldsymbol{\beta} \cdot \nabla\tilde{\boldsymbol{u}} + \boldsymbol{a}\tilde{\boldsymbol{u}} = \bar{\boldsymbol{f}}, \tag{3.20}$$

$$\frac{\partial\tilde{\boldsymbol{u}}}{\partial t} = \dot{\tilde{\boldsymbol{u}}}, \tag{3.21}$$

where $\dot{\tilde{\boldsymbol{u}}}$ is the first time derivative.

Using the wave extension form, there are six unknowns defined in two vectors as

$$\tilde{\boldsymbol{E}} = \begin{bmatrix}\tilde{\boldsymbol{E}}_x & \tilde{\boldsymbol{E}}_y & \tilde{\boldsymbol{E}}_z\end{bmatrix}^T \qquad \dot{\tilde{\boldsymbol{E}}} = \begin{bmatrix}\dot{\tilde{\boldsymbol{E}}}_x & \dot{\tilde{\boldsymbol{E}}}_y & \dot{\tilde{\boldsymbol{E}}}_z\end{bmatrix}^T. \tag{3.22}$$

Substitute $\dot{\tilde{\boldsymbol{E}}} = \dfrac{\partial\tilde{\boldsymbol{E}}}{\partial t}$ into equation 3.8 and add a second equation relating the first time derivative to the partial derivative with respect to t,

$$\mu\varepsilon\frac{\partial\dot{\tilde{\boldsymbol{E}}}}{\partial t} + \mu\sigma\dot{\tilde{\boldsymbol{E}}} + \nabla \cdot \left(-\boldsymbol{I}_3\nabla\tilde{\boldsymbol{E}}\right) = \nabla\left(\frac{\rho}{\varepsilon}\right), \tag{3.23}$$

$$\frac{\partial\tilde{\boldsymbol{E}}}{\partial t} - \dot{\tilde{\boldsymbol{E}}} = \bar{\boldsymbol{0}}, \tag{3.24}$$

where $\boldsymbol{I}_3$ is the identity matrix $\in \mathbb{R}^3$. This form results in six equations and six unknowns that can be expressed in matrix format

$$\begin{bmatrix}\boldsymbol{0} & \mu\varepsilon\boldsymbol{I}_3\\ \boldsymbol{I}_3 & \boldsymbol{0}\end{bmatrix}\frac{\partial}{\partial t}\begin{bmatrix}\tilde{\boldsymbol{E}}\\ \dot{\tilde{\boldsymbol{E}}}\end{bmatrix} + \nabla \cdot \left(-\begin{bmatrix}\boldsymbol{I}_3 & \boldsymbol{0}\\ \boldsymbol{0} & \boldsymbol{0}\end{bmatrix}\nabla\begin{bmatrix}\tilde{\boldsymbol{E}}\\ \dot{\tilde{\boldsymbol{E}}}\end{bmatrix}\right) + \begin{bmatrix}\boldsymbol{0} & \mu\sigma\boldsymbol{I}_3\\ \boldsymbol{0} & -\boldsymbol{I}_3\end{bmatrix}\begin{bmatrix}\tilde{\boldsymbol{E}}\\ \dot{\tilde{\boldsymbol{E}}}\end{bmatrix} = \begin{bmatrix}\nabla\left(\dfrac{\tilde{\boldsymbol{\rho}}}{\varepsilon}\right)\\ \bar{\boldsymbol{0}}\end{bmatrix}. \tag{3.25}$$

PDE in Strong Form for FEMLAB Coefficient Form

$$\boldsymbol{D}_a \frac{\partial \tilde{\boldsymbol{u}}}{\partial t} + \nabla \cdot (-\boldsymbol{c}\nabla\tilde{\boldsymbol{u}} - \boldsymbol{\alpha}\tilde{\boldsymbol{u}} + \boldsymbol{\gamma}) + \boldsymbol{\beta} \cdot \nabla\tilde{\boldsymbol{u}} + \boldsymbol{a}\tilde{\boldsymbol{u}} = \bar{\boldsymbol{f}}$$

Term	Symbol	Value
Unknowns	$\tilde{\boldsymbol{u}} =$	$\begin{bmatrix} \tilde{\boldsymbol{E}}^T & \dot{\tilde{\boldsymbol{E}}}^T \end{bmatrix}^T$
Mass coefficient	$\boldsymbol{D}_a =$	$\begin{bmatrix} \boldsymbol{0} & \mu\varepsilon\boldsymbol{I}_3 \\ \boldsymbol{I}_3 & \boldsymbol{0} \end{bmatrix}$
Diffusion coefficient	$\boldsymbol{c} =$	$\begin{bmatrix} \boldsymbol{I}_3 & \boldsymbol{0} \\ \boldsymbol{0} & \boldsymbol{0} \end{bmatrix}$
Conservative flux convection coefficient	$\boldsymbol{\alpha} =$	$\boldsymbol{0}$
Conservative flux source term	$\boldsymbol{\gamma} =$	$\boldsymbol{0}$
Convection coefficient	$\boldsymbol{\beta} =$	$\boldsymbol{0}$
Absorption coefficient	$\boldsymbol{a} =$	$\begin{bmatrix} \boldsymbol{0} & \mu\sigma\boldsymbol{I}_3 \\ \boldsymbol{0} & -\boldsymbol{I}_3 \end{bmatrix}$
Source term	$\bar{\boldsymbol{f}} =$	$\begin{bmatrix} \nabla\left(\frac{\rho}{\varepsilon}\right) \\ \bar{\boldsymbol{0}} \end{bmatrix}$

Table 3.2: Summary of Unknowns and Coefficients for FEMLAB Solution. Unfortunately, this formulation is not possible because there is no explicit access to all of the entries in $\boldsymbol{a}$.

Therefore, based on the original equation 3.17 the unknowns and coefficients are summarized in Table 3.2.

Unfortunately, this formulation is flawed due to the way that FEMLAB formulates the wave extension. In the third term of the equation 3.25, the $\mu\sigma\dot{\tilde{\boldsymbol{E}}}$ is not explicitly accessible. FEMLAB uses a unique augmentation method to create the wave extension that is only valid for lossless media ($\sigma = 0$). Details on how the wave extension is formulated can be found in the FEMLAB manuals [21] and is beyond the scope of this thesis.

However, it is possible to write the system using the generalized spatial differential operator and the weak form method to implement equation 3.25 with the associated boundary conditions. Again, FEMLAB fails to solve the problem efficiently as the linear system of equations that is created for the finite element method is difficult to solve. There does not exist an efficient preconditioner and iterative linear solver combination in FEMLAB 3.1 that can handle this formulation. However, the problem can be reformulated in another way that can be solved efficiently and accurately in FEMLAB. This method and the use of the weak form is discussed in the next two sections.

3.1.3 Vector Potential Formulation Derivation

Another common method for solving Maxwell's equations is to use scalar and vector potentials [5]. This method allows for the reduction in the number of curl operators in addition to maintaining a first order time derivative system which is preferred because it reduces the amount of inaccuracy in the field calculations and it can be implemented within the FEMLAB framework. The vector potential formulation is presented here for the time domain method. Note that this derivation runs parallel to the time harmonic derivation presented in Balanis [5].

Beginning with Gauss' Law for magnetics in equation 2.4 it is noted that the identity $\nabla \cdot (\nabla \times \tilde{\boldsymbol{u}}) = 0$ can be used to arbitrarily redefine the magnetic flux $\tilde{\boldsymbol{B}}$ to be the curl of some other value namely $\tilde{\boldsymbol{A}}$ which is defined as the magnetic vector potential.

$$\nabla \cdot \tilde{\boldsymbol{B}} = 0 \rightarrow \nabla \cdot \left(\nabla \times \tilde{\boldsymbol{A}} \right) = 0 \tag{3.26}$$

Using the constitutive relation in equation 2.14 and removing the divergence operator the curl of $\tilde{\boldsymbol{A}}$ to be related to the magnetic field intensity.

$$\tilde{\boldsymbol{H}} = \frac{1}{\mu}\nabla \times \tilde{\boldsymbol{A}} \tag{3.27}$$

Starting with Faraday's Law, equation 3.27 is substituted in to get

$$\nabla \times \tilde{\boldsymbol{E}} = -\frac{\partial}{\partial t}\left(\nabla \times \tilde{\boldsymbol{A}}\right). \tag{3.28}$$

Bringing the curl inside the time derivative and moving everything to the left hand side allows for the collection of the curl term which gives

$$\nabla \times \left(\tilde{\boldsymbol{E}} + \frac{\partial \tilde{\boldsymbol{A}}}{\partial t}\right) = 0. \tag{3.29}$$

Here it is noted that there exists the identity

$$\nabla \times (-\nabla\phi) = 0 \tag{3.30}$$

where ϕ is a scalar variable. In this particular case, the scalar variable is the scalar electric potential. Combining equations 3.29 and 3.30 results in

$$\tilde{\boldsymbol{E}} + \frac{\partial \tilde{\boldsymbol{A}}}{\partial t} = -\nabla\phi \rightarrow \tilde{\boldsymbol{E}} = -\frac{\partial \tilde{\boldsymbol{A}}}{\partial t} - \nabla\phi \tag{3.31}$$

The next step involves taking Ampere's Law and substituting in equation 3.27 where the following is obtained.

$$\nabla \times \frac{1}{\mu}\nabla \times \tilde{\boldsymbol{A}} - \sigma\tilde{\boldsymbol{E}} - \varepsilon\frac{\partial \tilde{\boldsymbol{E}}}{\partial t} = 0 \tag{3.32}$$

In equation 3.27, the curl of $\tilde{\boldsymbol{A}}$ is defined but the divergence has yet to be defined. Since the divergence is independent of its curl then the divergence can be defined arbitrarily. Therefore, it is desired to define the divergence in a manner that simplifies the formulation as is done similarly by Balanis for the time harmonic form [5].

Before defining the divergence the expression can be expanded by substituting in equation 3.31 and applying the vector identity in equation A.17.

$$\nabla\left(\nabla \cdot \tilde{\boldsymbol{A}}\right) - \nabla^2\tilde{\boldsymbol{A}} - \mu\sigma\tilde{\boldsymbol{E}} + \varepsilon\mu\frac{\partial}{\partial t}\left(\frac{\partial \tilde{\boldsymbol{A}}}{\partial t} + \nabla\phi\right) = 0 \tag{3.33}$$

The term that simplifies equation 3.33 is the Lorentz gauge.

$$\nabla \cdot \tilde{\boldsymbol{A}} = -\varepsilon\mu\frac{\partial\phi}{\partial t} \tag{3.34}$$

The boundary equations are formulated in a similar manner to that in the wave equation where equation 3.27 is substituted into 3.2 and 3.3. Formulation 3.2 can then be reformulated using equations 3.26, 3.33 and 3.34 to get a new formulation as shown in Formulation 3.3.

Formulation 3.3 Vector Potential Boundary Value Problem

$$\left.\begin{aligned} \nabla \times \frac{1}{\mu}\nabla \times \tilde{\boldsymbol{A}} - \sigma\tilde{\boldsymbol{E}} - \varepsilon\frac{\partial\tilde{\boldsymbol{E}}}{\partial t} = 0 \\ \tilde{\boldsymbol{E}} = -\frac{\partial\tilde{\boldsymbol{A}}}{\partial t} - \nabla\phi \\ \nabla \cdot \tilde{\boldsymbol{A}} = -\varepsilon\mu\frac{\partial\phi}{\partial t} \end{aligned}\right\} \quad \in \Omega$$

$$\left.\begin{aligned} \hat{\boldsymbol{n}} \times \left(\tilde{\boldsymbol{E}}^{+} - \tilde{\boldsymbol{E}}^{-}\right) = 0 \\ \hat{\boldsymbol{n}} \times \left(\frac{1}{\mu}\nabla \times \tilde{\boldsymbol{A}}^{+} - \frac{1}{\mu}\nabla \times \tilde{\boldsymbol{A}}^{-}\right) = 0 \end{aligned}\right\} \quad \in \Gamma_i$$

$$\hat{\boldsymbol{n}} \times \frac{1}{\mu}\nabla \times \tilde{\boldsymbol{A}} + \sqrt{\frac{\varepsilon}{\mu}}\left(\tilde{\boldsymbol{E}} - \left(\hat{\boldsymbol{n}} \cdot \tilde{\boldsymbol{E}}\right)\right)\hat{\boldsymbol{n}} = 2\sqrt{\frac{\varepsilon}{\mu}}\left(\tilde{\boldsymbol{E}}_0 - \left(\hat{\boldsymbol{n}} \cdot \tilde{\boldsymbol{E}}_0\right)\right)\hat{\boldsymbol{n}} + 2\hat{\boldsymbol{n}} \times \frac{1}{\mu}\nabla \times \tilde{\boldsymbol{A}}_0 \quad \in \Gamma_0$$

Before moving on to discuss the implementation details it is important to examine the above formulation. In this formulation, the source is only applied to the transverse boundary components. This is sufficient for plane waves that are travelling in the direction or anti-direction of the surface normal, however, difficulties arise when there exists field values in the normal direction of the boundary. For example, in Figure 3.1, a source with an E_y component on the boundary that is intersected by the y-axis will not be transmitted. Only the E_x and E_z are propagated across the boundary and into the volume. Therefore, in order to introduce signals more complicated than a plane wave at infinity, such as an infinitesimal dipole that has an E_y component, two methods can be employed.

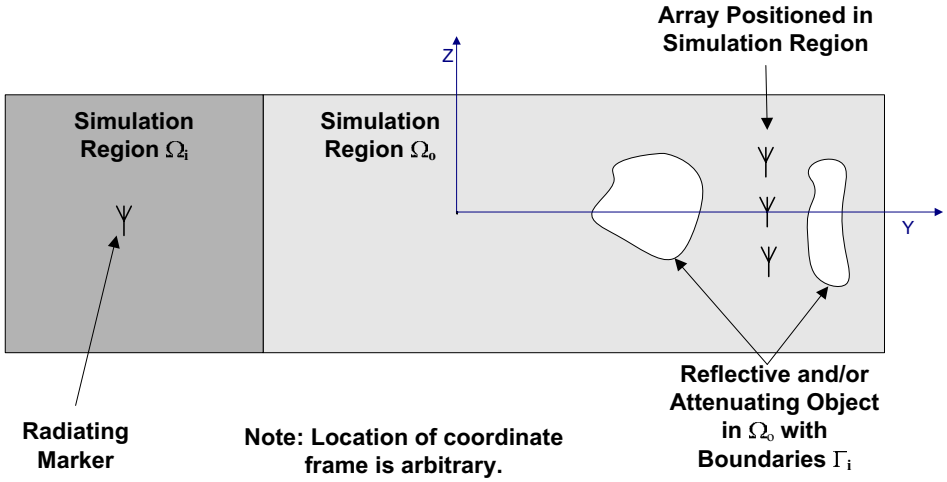

Figure 3.3: Conceptual schematic for incident and scattered fields. The electric fields in the input region are completely defined with a Dirichlet condition and the vector potential is computed using the equations in Formulations 3.4 or 3.5. The electric and vector potential fields are then computed throughout the rest of the volume. The boundary between the two regions is physically defined in Formulation 3.5 but is only mathematically defined in Formulation 3.4 by the function of $\tilde{\boldsymbol{E}}^i$.

The first method involves making a small change to the formulation by recognizing that the electric field can be separated into two components: incident or input field ($\tilde{\boldsymbol{E}}^i$) and the scattered field ($\tilde{\boldsymbol{E}}^s$) which is simply related to the total field by

$$\tilde{\boldsymbol{E}} = \tilde{\boldsymbol{E}}^i + \tilde{\boldsymbol{E}}^s. \tag{3.35}$$

Equation 3.35 can be substituted directly into the equations for Ω in Formulation 3.3. A new Dirichlet condition can be introduced which defines the values of the incident field for a small sub-volume such as the example given in Figure 3.3. The volume Ω is split into two sub-volumes Ω_i and Ω_o and the Dirichlet condition is applied differently in each volume.

$$\tilde{\boldsymbol{E}}^i = \tilde{\boldsymbol{E}}_0 \quad \in \Omega_i \tag{3.36}$$

$$\tilde{\boldsymbol{E}}^i = 0 \quad \in \Omega_o \tag{3.37}$$

where $\tilde{\boldsymbol{E}}_0$ is the electric field of the input signal defined by an analytical expression in Ω_i. The boundary conditions are handled differently in that it is only necessary to implement the absorbing boundary conditions on the scattered field and the input is already handled by the Dirichlet condition. The new formulation is provided in Formulation 3.4.

Formulation 3.4 Vector Potential BVP with Incident and Scattered Fields

$$\left.\begin{aligned} \nabla \times \frac{1}{\mu} \nabla \times \tilde{\boldsymbol{A}} - \sigma \left(\tilde{\boldsymbol{E}}^i + \tilde{\boldsymbol{E}}^s \right) - \varepsilon \frac{\partial}{\partial t} \left(\tilde{\boldsymbol{E}}^i + \tilde{\boldsymbol{E}}^s \right) = 0 \\ \tilde{\boldsymbol{E}}^i + \tilde{\boldsymbol{E}}^s = -\frac{\partial \tilde{\boldsymbol{A}}}{\partial t} - \nabla \phi \\ \nabla \cdot \tilde{\boldsymbol{A}} = -\varepsilon \mu \frac{\partial \phi}{\partial t} \end{aligned}\right\} \quad \in \Omega$$

$$\tilde{\boldsymbol{E}}^i = \tilde{\boldsymbol{E}}_0 \quad \in \Omega_i$$

$$\tilde{\boldsymbol{E}}^i = 0 \quad \in \Omega_o$$

$$\left.\begin{aligned} \hat{\boldsymbol{n}} \times \left(\tilde{\boldsymbol{E}}^{s+} - \tilde{\boldsymbol{E}}^{s-} \right) = 0 \\ \hat{\boldsymbol{n}} \times \left(\frac{1}{\mu} \nabla \times \tilde{\boldsymbol{A}}^{+} - \frac{1}{\mu} \nabla \times \tilde{\boldsymbol{A}}^{-} \right) = 0 \end{aligned}\right\} \quad \in \Gamma_i$$

$$\hat{\boldsymbol{n}} \times \frac{1}{\mu} \nabla \times \tilde{\boldsymbol{A}} + \sqrt{\frac{\varepsilon}{\mu}} \left(\tilde{\boldsymbol{E}}^s - \left(\hat{\boldsymbol{n}} \cdot \tilde{\boldsymbol{E}}^s \right) \right) \hat{\boldsymbol{n}} = 0 \quad \in \Gamma_0$$

The second method uses a similar configuration in Figure 3.3 but the two regions, Ω_i and Ω_o are physically separated and only the total field is considered. The material properties for the two regions are set to be identical except for any objects that are introduced into Ω_o and the boundary that separates the two regions has the same properties of Γ_i as defined in Formulation 3.3. Finally, an additional Dirichlet condition is added to Ω_i that defines the total electric field using an analytical expression, $\tilde{\boldsymbol{E}}_0$. The new set of equations is given in Formulation 3.5.

Formulation 3.5 Vector Potential BVP using an Input Region

$$\left.\begin{aligned} \nabla \times \frac{1}{\mu}\nabla \times \tilde{\boldsymbol{A}} - \sigma\tilde{\boldsymbol{E}} - \varepsilon\frac{\partial \tilde{\boldsymbol{E}}}{\partial t} = 0 \\ \tilde{\boldsymbol{E}} = -\frac{\partial \tilde{\boldsymbol{A}}}{\partial t} - \nabla\phi \\ \nabla \cdot \tilde{\boldsymbol{A}} = -\varepsilon\mu\frac{\partial \phi}{\partial t} \end{aligned}\right\} \quad \in \Omega_i, \Omega_o$$

$$\tilde{\boldsymbol{E}} = \tilde{\boldsymbol{E}}_0 \quad \in \Omega_i$$

$$\left.\begin{aligned} \hat{\boldsymbol{n}} \times \left(\tilde{\boldsymbol{E}}^+ - \tilde{\boldsymbol{E}}^-\right) = 0 \\ \hat{\boldsymbol{n}} \times \left(\frac{1}{\mu}\nabla \times \tilde{\boldsymbol{A}}^+ - \frac{1}{\mu}\nabla \times \tilde{\boldsymbol{A}}^-\right) = 0 \end{aligned}\right\} \quad \in \Gamma_i$$

$$\hat{\boldsymbol{n}} \times \frac{1}{\mu}\nabla \times \tilde{\boldsymbol{A}} + \sqrt{\frac{\varepsilon}{\mu}}\left(\tilde{\boldsymbol{E}} - \left(\hat{\boldsymbol{n}} \cdot \tilde{\boldsymbol{E}}\right)\right)\hat{\boldsymbol{n}} = 0 \quad \in \Gamma_0$$

Formulation 3.5 is preferred because it has fewer degrees of freedom than Formulation 3.4. The incident field, $\tilde{\boldsymbol{E}}^i$ introduces three more dependent variables to the equation set.

3.1.4 Vector Potential Formulation Implementation

With a new formulation defined it now needs to be examined for implementation within the FEMLAB framework. In reviewing the forms in equations 3.17, 3.18 and 3.19 in section 3.1.2 it is clear that the above formulation does not match. However, FEMLAB does allow that the equations can be input explictly using the weak form. However, before deriving the weak form, it is important to review the above formulation and note that this system has seven unknowns within the domain Ω. It would be advantageous to reduce the number of variables and equations in order to simplify the finite element system of equations.

De Flaviis et al. [25] has suggested that the scalar potential can be dropped by introducing a new vector variable $\tilde{\boldsymbol{K}}$. This new variable is related to the electric field such

that

$$\frac{\partial \tilde{\boldsymbol{K}}}{\partial t} = -\tilde{\boldsymbol{E}}. \tag{3.38}$$

It was shown by De Flaviis that curl properties remain constant and that similar results were exhibited with traditional finite difference time domain (FDTD) method, the new vector potential method and the analytical results. Therefore, the formulation can be written without the scalar potential and the constants can be re-arranged for future use since only linear materials are being considered at this time.

Formulation 3.6 Vector Potential BVP without the Scalar Potential

$$\left.\begin{aligned} \nabla \times \frac{1}{\mu} \nabla \times \tilde{\boldsymbol{K}} \varepsilon - \sigma \tilde{\boldsymbol{E}} - \frac{\partial}{\partial t} \tilde{\boldsymbol{E}} = 0 \\ \frac{\partial \tilde{\boldsymbol{K}}}{\partial t} + \tilde{\boldsymbol{E}} = 0 \end{aligned}\right\} \quad \in \Omega_i, \Omega_o$$

$$\tilde{\boldsymbol{E}} = \tilde{\boldsymbol{E}}_0 \quad \in \Omega_i$$

$$\left.\begin{aligned} \hat{\boldsymbol{n}} \times \left(\tilde{\boldsymbol{E}}^+ - \tilde{\boldsymbol{E}}^- \right) = 0 \\ \hat{\boldsymbol{n}} \times \left(\frac{1}{\mu} \nabla \times \tilde{\boldsymbol{K}}^+ - \frac{1}{\mu} \nabla \times \tilde{\boldsymbol{K}}^- \right) = 0 \end{aligned}\right\} \quad \in \Gamma_i$$

$$-\sqrt{\frac{\varepsilon}{\mu}} \left(\tilde{\boldsymbol{E}} - \left(\hat{\boldsymbol{n}} \cdot \tilde{\boldsymbol{E}} \right) \right) \hat{\boldsymbol{n}} - \hat{\boldsymbol{n}} \times \frac{1}{\mu} \nabla \times \tilde{\boldsymbol{K}} = 0 \quad \in \Gamma_0$$

The outer boundary condition can also be reformulated to be

$$-\sqrt{\frac{\varepsilon}{\mu}} \left(\frac{\partial \tilde{\boldsymbol{K}}}{\partial t} - \left(\hat{\boldsymbol{n}} \cdot \frac{\partial \tilde{\boldsymbol{K}}}{\partial t} \right) \right) \hat{\boldsymbol{n}} - \hat{\boldsymbol{n}} \times \frac{1}{\mu} \nabla \times \tilde{\boldsymbol{K}} = 0 \quad \in \Gamma_0 \tag{3.39}$$

which is similar to the impedance boundary condition in time harmonic form represented solely by the vector potential [12]. Further, if vector elements are used then the boundary

conditions on the internal boundaries are automatically fulfilled by the finite element formulation [20, 36]. That is, the electrical field is always continuous and the curl of the vector potential forms the natural boundary condition and is also continuous. Therefore, the internal boundary conditions can be omitted from the formulation since they are implicitly applied in the finite element formulation.

In order to implement this in FEMLAB the strong form shown in Formulation 3.6 needs to be expressed using the weak form. The weak form derivation as derived for implementation in FEMLAB is described here based on the general steps provided in the FEMLAB manual [20]. First, each of the equations in Formulation 3.6 are multiplied by a test function $\bar{\boldsymbol{v}}$. The test function must be sufficiently smooth and capable of providing an approximate solution of the problem. The collection of equations are then integrated over volume and boundaries. In order to simplify the formulation of the weak form, the vector test function is subdivided into two vectors such that

$$\bar{\boldsymbol{v}} = \begin{bmatrix} \bar{\boldsymbol{v}}_E \\ \bar{\boldsymbol{v}}_K \end{bmatrix}. \tag{3.40}$$

Multiplying the stacked equations by the vector test functions using the dot product and integrating over the volume results in the following weak formulation.

$$\begin{aligned} \iiint_{\Omega} \left[\bar{\boldsymbol{v}}_E \cdot \left(\nabla \times \frac{1}{\mu} \nabla \times \tilde{\boldsymbol{K}} \right) - \sigma \bar{\boldsymbol{v}}_E \cdot \tilde{\boldsymbol{E}} - \varepsilon \bar{\boldsymbol{v}}_E \cdot \frac{\partial}{\partial t} \tilde{\boldsymbol{E}} + \bar{\boldsymbol{v}}_K \cdot \tilde{\boldsymbol{E}} + \bar{\boldsymbol{v}}_K \cdot \frac{\partial \tilde{\boldsymbol{K}}}{\partial t} \right] \partial\Omega \\ + \iiint_{\Omega_i} \bar{\boldsymbol{v}}_E \cdot \left(\tilde{\boldsymbol{E}} - \tilde{\boldsymbol{E}}_0 \right) \partial\Omega_i \\ - \oiint_{\Gamma_o} \left[\sqrt{\frac{\varepsilon}{\mu}} \bar{\boldsymbol{v}}_E \cdot \left(\tilde{\boldsymbol{E}} - \left(\hat{\boldsymbol{n}} \cdot \tilde{\boldsymbol{E}} \right) \right) + \bar{\boldsymbol{v}}_E \cdot \left(\hat{\boldsymbol{n}} \times \frac{1}{\mu} \nabla \times \tilde{\boldsymbol{K}} \right) \right] \partial\Gamma_o = 0 \end{aligned} \tag{3.41}$$

Using Green's first vector theorem in equation A.18 provides an equivalent form for the third term of the weak form.

$$\begin{aligned} \iiint_{\Omega} \left[\bar{\boldsymbol{v}}_E \cdot \left(\nabla \times \frac{1}{\mu} \nabla \times \tilde{\boldsymbol{K}} \right) \right]) \partial\Omega \\ = \iiint_{\Omega} \frac{1}{\mu} \left[(\nabla \times \bar{\boldsymbol{v}}_E) \cdot \left(\nabla \times \tilde{\boldsymbol{K}} \right) \right] \partial\Omega - \oiint_{\Gamma_o} \left[\hat{\boldsymbol{n}} \cdot \left(\bar{\boldsymbol{v}}_E \times \frac{1}{\mu} \nabla \times \tilde{\boldsymbol{K}} \right) \right] \partial\Gamma_o \end{aligned} \tag{3.42}$$

Equation 3.42 can be substituted into 3.41 resulting in the following expression.

$$\begin{aligned}\iiint_{\Omega}\left[\frac{1}{\mu}\left(\nabla\times\bar{\boldsymbol{v}}_E\right)\cdot\left(\nabla\times\tilde{\boldsymbol{K}}\right)-\sigma\bar{\boldsymbol{v}}_E\cdot\tilde{\boldsymbol{E}}-\varepsilon\bar{\boldsymbol{v}}_E\cdot\frac{\partial}{\partial t}\tilde{\boldsymbol{E}}+\bar{\boldsymbol{v}}_K\cdot\tilde{\boldsymbol{E}}+\bar{\boldsymbol{v}}_K\cdot\frac{\partial\tilde{\boldsymbol{K}}}{\partial t}\right]\partial\Omega\\ +\iiint_{\Omega_i}\bar{\boldsymbol{v}}_E\cdot\left(\tilde{\boldsymbol{E}}-\tilde{\boldsymbol{E}}_0\right)\partial\Omega_i\\ -\oiint_{\Gamma_o}\left[\sqrt{\frac{\varepsilon}{\mu}}\bar{\boldsymbol{v}}_E\cdot\left(\tilde{\boldsymbol{E}}-\left(\hat{\boldsymbol{n}}\cdot\tilde{\boldsymbol{E}}\right)\right)+\bar{\boldsymbol{v}}_E\cdot\left(\hat{\boldsymbol{n}}\times\frac{1}{\mu}\nabla\times\tilde{\boldsymbol{K}}\right)+\hat{\boldsymbol{n}}\cdot\left(\bar{\boldsymbol{v}}_E\times\frac{1}{\mu}\nabla\times\tilde{\boldsymbol{K}}\right)\right]\partial\Gamma_o=0\end{aligned} \tag{3.43}$$

The terms that contain the $\nabla\times\tilde{\boldsymbol{K}}$ on the outer boundary cancel because $\hat{\boldsymbol{n}}\cdot\left(\bar{\boldsymbol{v}}_E\times\nabla\times\tilde{\boldsymbol{K}}\right)$ can be re-written as $(\hat{\boldsymbol{n}}\times\bar{\boldsymbol{v}}_E)\cdot\left(\nabla\times\tilde{\boldsymbol{K}}\right)$ using identity A.3 and similarly $\bar{\boldsymbol{v}}_E\cdot\left(\hat{\boldsymbol{n}}\times\nabla\times\tilde{\boldsymbol{K}}\right)$ can be written as $-\left(\hat{\boldsymbol{n}}\times\bar{\boldsymbol{v}}_E\right)\cdot\left(\nabla\times\tilde{\boldsymbol{K}}\right)$. This results in the final equation set in Formulation 3.7 that is implemented into FEMLAB.

Formulation 3.7 Vector Potential BVP Weak Form

$$\iiint_{\Omega}\left[\frac{1}{\mu}\left(\nabla\times\bar{\boldsymbol{v}}_E\right)\cdot\left(\nabla\times\tilde{\boldsymbol{K}}\right)-\sigma\bar{\boldsymbol{v}}_E\cdot\tilde{\boldsymbol{E}}-\varepsilon\bar{\boldsymbol{v}}_E\cdot\frac{\partial}{\partial t}\tilde{\boldsymbol{E}}+\bar{\boldsymbol{v}}_K\cdot\tilde{\boldsymbol{E}}+\bar{\boldsymbol{v}}_K\cdot\frac{\partial\tilde{\boldsymbol{K}}}{\partial t}\right]\partial\Omega$$

$$+\iiint_{\Omega_i}\bar{\boldsymbol{v}}_E\cdot\left(\tilde{\boldsymbol{E}}-\tilde{\boldsymbol{E}}_0\right)\partial\Omega_i-\oiint_{\Gamma_o}\left[\sqrt{\frac{\varepsilon}{\mu}}\bar{\boldsymbol{v}}_E\cdot\left(\tilde{\boldsymbol{E}}-\left(\hat{\boldsymbol{n}}\cdot\tilde{\boldsymbol{E}}\right)\right)\right]\partial\Gamma_o=0$$

The test functions, $[\bar{\boldsymbol{v}}_E \quad \bar{\boldsymbol{v}}_K]^T$, are the same functions that are used as interpolating functions in the finite elements. The test functions are supposed to be functions that can approximate the solution which is why the elemental interpolation functions are such a good fit because they were derived for the same reason. Details on the weak formulation, test functions and finite element interpolation functions can be found in the literature [36, 38, 43, 64].

3.2 Finite Element Method

The finite element method is well documented in the literature for its ability to numerically solve initial value problems and boundary value problems for many types of applications including electromagnetics [36, 38, 43, 64]. In particular, Jin [36] provides a very practical manual on the implementation of the finite element method while Monk [43] provides a very thorough mathematical discussion on the method.

In general, the FEMLAB software performs most of the difficult tasks for the finite element method and keeps them hidden from the user. However, since this simulation is a custom implementation, some details of the simulation need to be examined. A process diagram identifying the high level steps for the finite element model is given in Figure 3.4.

The first step in Figure 3.4, *Define Geometry*, involves creating a mathematical definition of the geometry for the simulation. The techniques used by FEMLAB to define the geometry are described in section 3.2.1. The governing equations of the simulation have been provided in section 3.1. Formulation 3.7 is the formulation required for the *Define Equations* step. The *Generate Mesh* step is where the geometry is discretized into finite elements. Details on the discretization and mesh generation are found in section 3.2.2. The size restrictions for the finite elements are discussed in section 3.2.3 in parallel with the time step size restriction which is required when the finite element equations are solved. The *Generate FEM Equations* step sees the finite element equations generated based on the vector finite elements described in section 3.2.2 and the physical location of each of the elements created during the mesh generation. The finite element equations are discrete approximations of the equations shown in Formulation 3.7 which include both the vector potential wave propagation equations and the first order absorbing boundary conditions. It has already been assumed that the first order absorbing boundary condition will be implemented but the other popular method of volume truncation, perfectly matched layers, and why it was not chosen is discussed in section 3.2.4. The collection of finite element equations form a linear system of equations that are solved in conjunction with a time stepping algorithm. The solution techniques in the *Solve System of Equations* step are presented in section 3.2.5. The final step is the *Post Simulation Analysis* step where the antenna models discussed in section 3.3 can be used to extract signals for use in the spatial measurement algorithm studies. At the end of this section, the difficulties found within FEMLAB are discussed as some undocumented or misleading descriptions in the FEMLAB

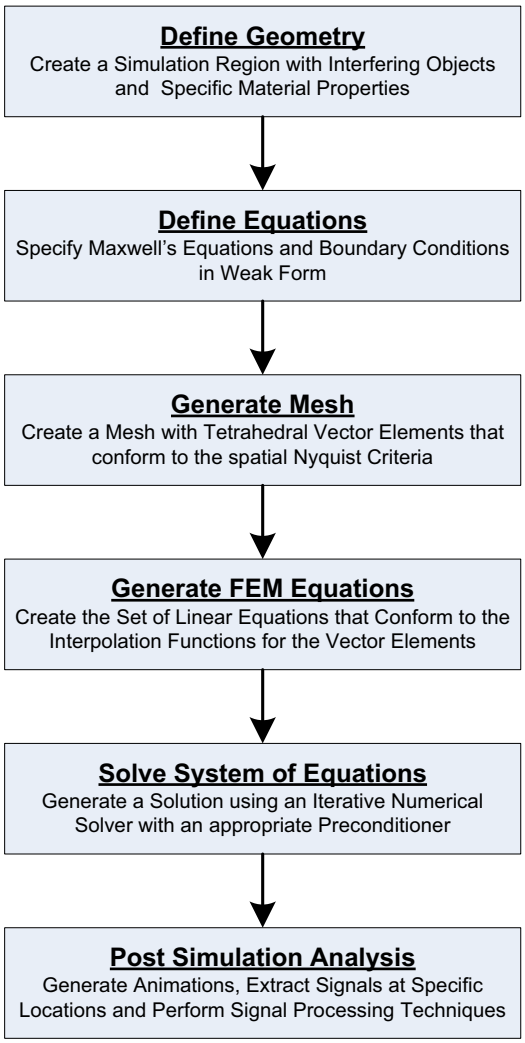

Figure 3.4: Process diagram for the finite element method.

manuals are explained in the context of this simulation. This section contains only a brief overview of the finite element method and the reader should consult the aforementioned texts for more detail.

3.2.1 Geometry Definition

In FEMLAB, the geometry can be represented in two different ways. The geometry can be imported from a DXF CAD format defined by several types of drafting software or the geometry can be built up using some basic building blocks (e.g., rectangular prisms, spheres, other three dimensional, two dimensional, one dimensional shapes) in the FEMLAB library. The basic building blocks provide a sufficient level of complexity to the current research.

The building blocks can be generated using the FEMLAB drawing tool or through a scripting language that is interpreted through the FEMLAB MATLAB[6] interface. The scripting language method was chosen for automation and parameterization purposes of the simulation process.

For three dimensional simulations, FEMLAB divides the geometry into four categories depending on the dimensionality of the object. The three dimensional objects are referred to as sub-domains and are used to describe the truncation volume and any other objects that appear within the simulated region. Collectively, the sub-domains form the global domain Ω that is used in the governing equations in section 3.1. The domain Ω is easily sub-divided into the input region Ω_i and region of interest Ω_o shown in Figure 3.3. Each sub-domain also stores the information relating to the material properties. For example, the rectangular prism that is used to represent the truncation boundary is either free space or air where the electrical properties are as defined in Table 2.1 while the attenuating and reflecting objects added to the volume could be made of wood, aluminum, water, etc.

The two dimensional objects are the faces on the sub-domains and are used to define the boundary conditions. The faces can be planar (e.g., prism surface) or curved (e.g., sphere surface) depending on the geometry of the sub-domain. Similarly to the sub-domains, the

[6]MATLAB, short form for matrix laboratory, is a general tool that is used for mathematical simulation and analysis. FEMLAB was originally built on the MATLAB platform before being created as a standalone package. However, the capabilities of scripting in the MATLAB environment remain for the purpose of automated simulations.

collection of the boundary components form the boundary Γ which can be divided into the internal and external boundaries, Γ_i and Γ_o. The faces can also be inserted independently to simulate thin structures such as microstrip antennas.

The one dimensional objects are the edge components which are represented by lines. As with the faces, edges can be straight or curved. Finally, the vertices (zero dimensional components) define infinitesimally small locations in the volume. Currently, the edge and vertex objects are not used explicitly in the simulation and are not included in the governing equations. They however, may be also included in the future to simplify the modelling of the complex antenna designs. It is here where the weak formulation of the partial differential equations becomes particularly useful as edge and point contributions can be added to the system.

3.2.2 Spatial Discretization and Mesh Generation

The fundamental idea of the finite element method is that a boundary value problem can be discretized into a set of small localized problems that together will provide an approximate solution that is sufficiently accurate. This replaces the typically impossible task of attempting to solve the problem using an analytical form. However, before the set of equations can be formulated the volume needs to be discretized into its finite elements.

There are several types of finite elements that can be used. In three dimensions tetrahedral and brick elements are common while triangular and rectangular elements are common in two dimensions. In this simulation tetrahedral elements like the ones shown in Figure 3.5 are used throughout the volume. The collection of finite elements that make up the physical geometry is called a mesh where the mesh generation technique uses a Delaunay tetrahedralization to generate the connected graph [27].

In typical finite element analysis the elemental and global equations are based on solving the dependent variables at the nodes of the elements while interpolation functions describe the field values for positions within a given element. The development of these equations is quite prominent in the literature including the aforementioned texts [36, 38, 43, 64] and will not be discussed in detail here.

However, a common issue with finite element simulations for electromagnetics is the occurrence of spurious solutions [36, 43]. In simple terms, the equations generated using nodal elements do not satisfy the divergence or curl conditions given in equations 2.3

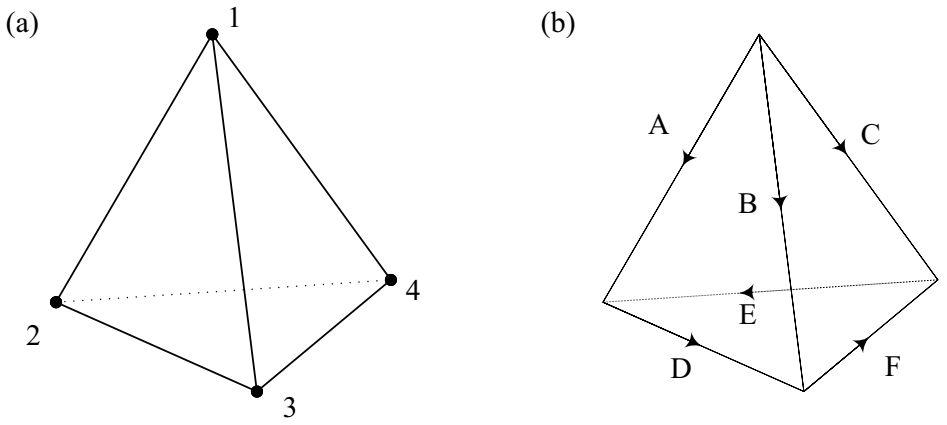

Figure 3.5: Sample tetrahedral elements in 3D. A nodal finite element shown in (a) uses field measurements at the nodes to approximate the field throughout the volume while the vector element in (b) approximates the field variables along the edges of the elements. The vector element is a zeroth order element. Higher order vector elements are not available within the FEMLAB application.

and 2.4. Further, difficulties arise when attempting to introduce boundary conditions for absorption. In order to correct for these issues a new element is introduced which eliminates the spurious solutions.

The Vector Finite Element[7] shown in (b) of Figure 3.5 prevents the existence of spurious solutions and allows for easy definition of boundary conditions. The main difference between the nodal element and the vector element is in the definition of the degrees of freedom (dependent variables). For the nodal element there are four dependent vector variables resulting in 12 degrees of freedom. The degrees of freedom associated with the nodal element that approximate the electric field are

$$\left.\begin{array}{l} E_{xi} \\ E_{y_i} \\ E_{zi} \end{array}\right\} \quad \text{for nodes } i = 1, 2, 3, 4. \tag{3.44}$$

For the vector element, the degrees of freedom are defined to be the field variable that is tangential to the edge. FEMLAB adds a t in front of the variable name in order to

[7]The vector finite element is also known as an edge element [36] and a Nedelec element [43].

distinguish it from the field variable. This can be shown mathematically as

$$tE_i = \hat{\boldsymbol{t}}_i \cdot \bar{\boldsymbol{E}} \quad \text{for edges } i = A, B, C, D, E, F. \tag{3.45}$$

The field value within an element is determined by interpolating the values on each edge where each edge value is weighted by a normalized distance between the point of interest and the associated edge. In nodal elements, a similar interpolation method is used but the field value is determined by interpolating the nodal values based on the distance from the point of interest to each node. Details of the interpolating functions can be found in Jin [36].

Although the main motivation in developing this element was to correct the issues with the divergence condition and assist with the definition of the boundary conditions, it has also resulted in reducing the number of degrees of freedom by half to six. Again, the practical implementation details can be found in Jin [36] while the full mathematical treatment is given in Monk [43].

3.2.3 Temporal and Spatial Sampling Rates

Numerical methods that are used in either the spatial domain or time domain require that special attention be paid to the sampling rates. Sampling rates that are too low will result in aliasing of the signal[8]. In the time domain, the sampling occurs at either regular or varying time intervals but in either case the size of the time step cannot be too large. FEMLAB allows that the user specify either a fixed time stepping algorithm or a free time stepping algorithm with a maximum time step specified. The free time stepping algorithm was used for this simulation framework.

The maximum time step can also be related to a minimum sampling frequency. The minimum required sampling frequency or the maximum possible time step is given by the Nyquist criteria [46, 51]

$$\begin{aligned} f_{sample} &= 2 f_{max} \quad \text{or} \\ t_{step} &= \frac{1}{2} T_{min} \end{aligned} \tag{3.46}$$

[8] Aliasing of a signal occurs when a signal is undersampled and the true form of the signal cannot be replicated after the signal is sampled.

where f_{max} is the largest frequency in the signal and T_{min} is the smallest signal period[9]. For the simulations presented in Chapters 4 and 5, t_{step} is set to 0.05 ns and correspondingly f_{sample} is 20 GHz. This sampling frequency is more than 10 times larger than the maximum signal frequency but this takes into account any noise in the system that may be higher than the GPS L1 frequency that is close to 1.5 GHz.

Similarly, in the spatial domain the sampling occurs at either regularly or varying spaced position intervals. In the finite element method the spacing is the distance between nodes and is varying depending on the meshing algorithm. Fixed nodal spacing can be implemented but the meshing algorithm can result in a degenerative mesh case. Therefore, the spatial sampling rates are related to the size of a finite element.

The size of an element is given by $h_{max} = \max(h_i)$ where h_i is the length of edge i for $i = A, B, C, D, E, F$. In order to avoid aliasing of the wave propagating through the volume in the spatial domain the distance between two nodes on all of the elements must be less than half of the smallest wavelength, λ_{min}, exhibited in the system.

$$h_{max} <= \lambda_{min}/2 \tag{3.47}$$

Note that the wavelength λ of a propagating wave or signal is related to the frequency f of the system by $\lambda = c/f$ where c is the speed of light in free space or $c = 1/\sqrt{\varepsilon\mu}$ in real materials. For the simulations presented in Chapters 4 and 5 λ_{min} corresponds to 0.015 m based on the aforementioned t_{step} and f_{sample}.

3.2.4 Volume Truncation

The simulation described here is an unbounded problem solved in a finite region hence requiring some boundaries that are not physical. Therefore, the external boundaries, Γ_o, need to perform two things. First, they must allow the specified input fields in from an external source. This was done by separating the electric field into its input and scattering components in equation 3.35 and introducing the input on a small sub-volume and allowing the input to propagate further through the volume.

Second, the boundaries need to absorb any electric fields leaving the boundary. The natural effect of the finite element method causes the boundaries to reflect portions of

[9]The maximum frequency and the minimum period are related by $f_{max} = \frac{1}{T_{min}}$

the imposing fields back into the volume creating a non-physical representation of the actual field. This is useful in waveguide studies where the walls of the waveguide actually reflect in a physical sense hence allowing the natural boundary conditions to be very useful. However, in a simulation that is supposed to be physically unbounded it is desired that the boundaries actually represent the volume extending to infinity, that is the boundaries absorb the energy impinged on them.

There are two methods that were investigated for volume truncation within the time domain finite element method. The first is the absorbing boundary condition and these are the conditions actually implemented in this simulation. These are the simplest boundary conditions that do not require any special implementation other than applying the equations on the boundary elements. However, the literature is mainly geared to the second order wave equation formulation [37, 36] and there was no boundary condition explicitly defined for the vector potential time domain formulation.

The low reflecting boundary condition (equation 3.3) suggested for the time harmonic solution as given by the FEMLAB [21] was implemented and it was quickly discovered in the section 3.1 that the first order absorbing condition as given in Carpes et al. [37] and Jin [36] can be derived from this low reflecting boundary condition. The boundary condition in equation 3.3 can also be put into the time harmonic form presented in Boyse et al. [12]. These absorbing conditions are not perfectly absorbing for all electric fields that impinge on the boundary but they are sufficient for the purpose of this simulation. The performance of this boundary condition is discussed further in Chapter 4.

The perfectly matched layer (PML) method was briefly introduced with regards to the finite difference time domain method (FDTD) in section 2.1.1.1. In time harmonic finite element formulation, the PML method is relatively straight forward indefining a set of complex anisotropic permittivity and permeabilities using a Laplace transform variable ($s = \alpha + j\omega$) in the absorbing regions that surround the truncated volume. The complex electrical properties create a lossy material that does not reflect at the boundary but gradually absorbs the wave as it moves outward.

Recently, the PML method has been extended to the finite element method by Jiao [34, 35] and Rylander [54, 55] using the inverse Laplace transform to convert the partial differential equations from the frequency domain to the time domain. Unfortunately, the term where the field variables are multiplied by the complex permeability or permittivity in the frequency domain becomes a convolution in the time domain. Since the first order

absorbing boundary conditions mentioned earlier were sufficient, the added complexity of a convolution operator in the finite element equations was unnecessary. Further, it would have been difficult to implement the convolution in the FEMLAB framework without increasing the number of equations.

3.2.5 Numerical Solvers

Once the finite element equations have been generated they can be solved using the linear system solver and a time stepping algorithm. Within FEMLAB there are not a lot choices for solvers since the form of the matrix is created by the stacking of the linear system of finite element equations. Since the system of equations is large an iterative solver with a preconditioning algorithm was chosen to solve system of equations. The resulting equations are not positive definite and are not symmetric causing several of the methods provided by FEMLAB to be useless. By the process of elimination the incomplete LU algorithm was chosen for the preconditioner and generalized minimum residual (GMRES) method was chosen for the linear solver [22].

The time stepping algorithm is based on a differential-algebraic system of equations solver called DASPK developed at the University of California, Santa Barbara [22].

3.2.6 FEMLAB Shortcomings

In creating this simulation, there were three items of confusion found within the FEMLAB manuals that caused some frustration in developing this simulation. The first has to do with the tangential variables defined for the vector finite elements. In the manuals, there is a reference to the tangential variables used on the boundaries for the finite element program which are defined as tEx, tEy, tEz. At first it was interpreted that the variables were simply a short hand for the tangential components of the field $\tilde{\boldsymbol{E}}$ given by $\tilde{\boldsymbol{E}}_{tan} = \left(\hat{\boldsymbol{t}} \cdot \tilde{\boldsymbol{E}}\right) \hat{\boldsymbol{t}}$ where $\hat{\boldsymbol{t}}$ is the tangential unit vector. Since in three-dimensions the tangential vector of a surface has an infinite number of possible directions, the tangential components of the fields are often related to the normal vector of the surface $\hat{\boldsymbol{n}}$ by the cross product $\tilde{\boldsymbol{E}}_{tan} = \hat{\boldsymbol{n}} \times \tilde{\boldsymbol{E}}$. However, it was later discovered through experiments that this was not true such that

$$\begin{bmatrix} tEx \\ tEy \\ tEz \end{bmatrix} \neq \hat{\boldsymbol{n}} \times \tilde{\boldsymbol{E}} \quad \in \Gamma \tag{3.48}$$

but instead the following is true.

$$\begin{bmatrix} tEx \\ tEy \\ tEz \end{bmatrix} = \tilde{\boldsymbol{E}} \quad \in \Gamma \tag{3.49}$$

This caveat requires the boundary equations be redefined so that the cross product with the normal vector is explicitly defined rather than assumed to be contained within the tangential variable. The confusion is extended further as spatial derivatives on the boundary are labeled as $tExTx$ for $\partial tE_x/\partial x$ and is similarly labeled for other vector variables and dimensions.

The second caveat found in developing the solution is in how the weak form is input into the FEMLAB solver. In section 3.1 the curl-curl operator is multiplied with a vector test function (element shape function) by the dot product. In order to simplify the formulation so that it is limited to first order spatial derivatives Green's first vector identity in equation A.18 is applied such that

$$\bar{\boldsymbol{v}}_e \cdot \left(\nabla \times \nabla \times \tilde{\boldsymbol{K}} \right) \rightarrow (\nabla \times \hat{\boldsymbol{v}}_e) \cdot \left(\nabla \times \tilde{\boldsymbol{K}} \right). \tag{3.50}$$

Expanding the curl operators for the test function into partial derivatives the expression on the right hand side of the arrow above becomes

$$(\nabla \times \hat{\boldsymbol{v}}_e) \cdot \left(\nabla \times \tilde{\boldsymbol{K}} \right) = \begin{bmatrix} \dfrac{\partial v_{ez}}{\partial y} - \dfrac{\partial v_{ey}}{\partial z} \\ \dfrac{\partial v_{ex}}{\partial z} - \dfrac{\partial v_{ez}}{\partial x} \\ \dfrac{\partial v_{ey}}{\partial x} - \dfrac{\partial v_{ex}}{\partial y} \end{bmatrix} \cdot \left(\nabla \times \tilde{\boldsymbol{K}} \right). \tag{3.51}$$

Implementing the above expression in FEMLAB results in an ill-conditioned system as it seems the volume integrals are not applied properly. Instead, the vector of partial derivatives needs to be separated into two terms and then input as

$$(\nabla \times \hat{\boldsymbol{v}}_e) \cdot \left(\nabla \times \tilde{\boldsymbol{K}}\right) = \begin{bmatrix} \dfrac{\partial v_{ez}}{\partial y} \\ \dfrac{\partial v_{ex}}{\partial z} \\ \dfrac{\partial v_{ey}}{\partial x} \end{bmatrix} \cdot \left(\nabla \times \tilde{\boldsymbol{K}}\right) - \begin{bmatrix} \dfrac{\partial v_{ey}}{\partial z} \\ \dfrac{\partial v_{ez}}{\partial x} \\ \dfrac{\partial v_{ex}}{\partial y} \end{bmatrix} \cdot \left(\nabla \times \tilde{\boldsymbol{K}}\right). \tag{3.52}$$

This formulation ensures that the equations are generated properly and that a properly conditioned system of equations is created.

A third issue encountered during the model development is in the need to explicitly define the finite element type on all geometrical levels. Upon generating a new model in FEMLAB, the program has a default element definition, typically a first or second order Lagrange nodal element. At first the vector elements were only explicitly defined at the sub-domain level and the default element was applied to the boundaries. Unfortunately, this form does not allow for the continuity equations assumed to be natural in the formulation to exist as is mentioned when developing the weak formulation in equation 3.41. The electric and vector potential fields do not cross any boundaries and only exist within the input region Ω_i. However, if the boundary elements are replaced explicitly with the vector element then the continuity equations are naturally imposed and the fields propagate across the boundary without issue.

3.3 Sensor Modelling

With the governing equations derived in Section 3.1 and the finite element method defined in Section 3.2 the attention turns to the signal source, $\tilde{\boldsymbol{E}}_0$ via a transmitting antenna and the acquisition of the signal at a receiving antenna. The source signal is considered first followed by a discussion on the signal acquisition technique. This discussion is related to phase 2 of the simulation process diagram shown in Figure 3.2 on page 33.

3.3.1 Transmitting Marker Source

The source signal or transmitting marker can be considered in two different contextual views, first the origin of the marker can be contained inside the simulation volume or the marker can be located externally to simulation. Figure 3.1 shows the marker located externally to the volume of interest.

If the marker is found to be contained within the volume then it can be modelled in two different ways. First, the antenna geometry can be included in the simulation at the marker position and the surface current at the active region of the antenna can be defined. The surface current is included in Maxwell's equations using the $\tilde{\boldsymbol{J}}$ variable expanded as

$$\tilde{\boldsymbol{J}} = \sigma\tilde{\boldsymbol{E}} + \tilde{\boldsymbol{J}}^i \tag{3.53}$$

where $\sigma\tilde{\boldsymbol{E}}$ is the surface current introduced by a conducting material and $\tilde{\boldsymbol{J}}^i$ is the source surface current defined by the antenna signal. Models for many types of antennas are included in Balanis' electromagnetic theory text[5] and antenna theory text [6].

The second method involves assuming that the source current density is zero and the electric field source signal for the given antenna is derived using analytical methods found in Balanis [6]. The analytically determined fields are applied to the input electric field variable ($\tilde{\boldsymbol{E}}_0$) as described in Section 3.1.

If the transmitting marker is located outside of the volume the implementation is the same for the second method used for a marker inside the volume where the electric field is solved for analytically and applied to the input electric field variable. This method is preferred for the scope of studies in this thesis but the other methods may be used as the simulation is used in the future for more complex case studies.

The analytical derivations for different signal types can be easily formulated using Balanis [6], however, only three formulations are presented as examples. These signals are (i) a plane wave, an isotropic source located at an infinite distance; (ii) a cylindrical wave, an infinite line source located at a finite distance from the simulation region; and (iii) a spherical wave located at a point that is a finite distance from the simulation region. In each case, the resulting electromagnetic wave is derived for three signal shapes, (a) Gaussian pulse, (b) Neumann pulse and (c) sinusoid modulated with a Gaussian pulse.

In reality, all three signal sources are not physically realizable nor can they be derived using Maxwell's equations using a current density source. The source types are not realizable because there are no physical objects that exist that can generate the appropriate surface current that can create the associated electric radiation pattern. However, these signals are useful approximations for more complicated antennas and can be simply defined explicitly in terms of the electric field intensity. Moreover, each signal type; plane, cylindrical and point source; can be defined for a source location ($\bar{\boldsymbol{p}}_{src} = x_{src}\hat{\boldsymbol{e}}_x + y_{src}\hat{\boldsymbol{e}}_y + z_{src}\hat{\boldsymbol{e}}_z$)

at observation point ($\bar{\boldsymbol{p}}_{obs} = x_{obs}\hat{\boldsymbol{e}}_x + y_{obs}\hat{\boldsymbol{e}}_y + z_{obs}\hat{\boldsymbol{e}}_z$) in Cartesian coordinates using the same notation for each signal type and are given in equations 3.54, 3.55 and 3.56.

Gaussian Pulse:

$$\tilde{\boldsymbol{E}}(\bar{\boldsymbol{p}}_{obs}, t) = A_0 \exp\left[\frac{-\left(t - t_0 - \frac{|\bar{\boldsymbol{r}}|}{c}\right)^2}{\tau^2}\right]\hat{\boldsymbol{e}} \tag{3.54}$$

Neumann Pulse (first time derivative of equation 3.54):

$$\tilde{\boldsymbol{E}}(\bar{\boldsymbol{p}}_{obs}, t) = -2A_0\left[\frac{\left(t - t_0 - \frac{|\bar{\boldsymbol{r}}|}{c}\right)}{\tau^2}\right]\exp\left[\frac{-\left(t - t_0 - \frac{|\bar{\boldsymbol{r}}|}{c}\right)^2}{\tau^2}\right]\hat{\boldsymbol{e}} \tag{3.55}$$

Sinusoid Modulated with a Gaussian Pulse:

$$\tilde{\boldsymbol{E}}(\bar{\boldsymbol{p}}_{obs}, t) = A_0 \exp\left[\frac{-\left(t - t_0 - \frac{|\bar{\boldsymbol{r}}|}{c}\right)^2}{\tau^2}\right]\cdot \sin(\omega t - k|\bar{\boldsymbol{r}}|)\hat{\boldsymbol{e}} \tag{3.56}$$

where t_0 is the time shift, τ is the Gaussian pulse width, ω is the angular frequency, k is the spatial frequency ($2\pi/\lambda$) of the sinusoidal signal, and $|\bar{\boldsymbol{r}}|$ is the signal distance to the observation point and $\hat{\boldsymbol{e}}$ is the electric field direction. The distance from source to observation point and the field direction is determined by using a modified spherical coordinate system (r, θ, ϕ) with its origin at $\bar{\boldsymbol{p}}_{src}$. The direction of propagation is in the $\hat{\boldsymbol{e}}_r$ and the electric field is present in the $\hat{\boldsymbol{e}}_\theta$ direction. The magnetic field would appear in the $\hat{\boldsymbol{e}}_\phi$ direction. However, in order to define wave propagation for the plane, cylindrical and spherical waves using the same notation, a wave type variable $\bar{\boldsymbol{d}} = \begin{bmatrix} d_x & d_y & d_z \end{bmatrix}^T$ is introduced. Further the spherical coordinates are defined as

$$\bar{\boldsymbol{r}} = r\hat{\boldsymbol{e}}_r \tag{3.57}$$

$$\bar{\boldsymbol{\theta}} = \theta\hat{\boldsymbol{e}}_\theta \tag{3.58}$$

$$\bar{\boldsymbol{\phi}} = \phi\hat{\boldsymbol{e}}_\phi \tag{3.59}$$

and are related to the Cartesian coordinate system using the wave type variable by

$$r = \sqrt{\left[\bar{\boldsymbol{d}} \odot (\bar{\boldsymbol{p}}_{obs} - \bar{\boldsymbol{p}}_{src})\right] \cdot \left[\bar{\boldsymbol{d}} \odot (\bar{\boldsymbol{p}}_{obs} - \bar{\boldsymbol{p}}_{src})\right]} \tag{3.60}$$

$$\theta = \cos^{-1}\left(\frac{d_z\left(z_{obs} - z_{src}\right)}{r}\right) \tag{3.61}$$

$$\phi = \tan^{-1}\left(\frac{d_y\left(y_{obs} - y_{src}\right)}{d_x\left(x_{obs} - x_{src}\right)}\right). \tag{3.62}$$

$\bar{\boldsymbol{d}}$ is set to be $\begin{bmatrix}1 & 0 & 0\end{bmatrix}^T$ for a plane wave travelling in the $+x$-direction and $\begin{bmatrix}0 & 1 & 0\end{bmatrix}^T$ for a travelling wave in the $+y$-direction. A cylindrical wave in the xy-plane has $\bar{\boldsymbol{d}} = \begin{bmatrix}1 & 1 & 0\end{bmatrix}^T$ while a point source is defined by $\bar{\boldsymbol{d}} = \begin{bmatrix}1 & 1 & 1\end{bmatrix}^T$.

Examples of the three signal shapes are shown in Figure 3.6 for the E_z component for a signal located at $\bar{\boldsymbol{p}}_{src} = \begin{bmatrix}0.00 & -1.00 & 0.00\end{bmatrix}^T$ and with the first observation point located at $\bar{\boldsymbol{p}}_{src_1} = \begin{bmatrix}0.00 & -0.25 & 0.00\end{bmatrix}^T$ and the second observation point located at $\bar{\boldsymbol{p}}_{src_2} = \begin{bmatrix}0.00 & 0.25 & 0.00\end{bmatrix}^T$. Due to the nature of the signals, the signal located at this particular observation point is identical for the plane wave, cylindrical wave and spherical wave because the r term is identical for all three.

3.3.2 Receiving Sensors

The receiving sensors have been chosen to be modelled as infinitesimal dipoles [6]. Infinitesimal dipole antennas are thin wire antennas where the length of the antenna is very short and the radius of the wire is very small. The voltage signal is determined in equation 3.63 by projecting the electric field vector at $\bar{\boldsymbol{p}}_{obs}$ onto the dipole where $\bar{\boldsymbol{t}}_d$ is parallel to the dipole wire and $\ell \ll \lambda$ is the length of the dipole. A schematic of the infinitesimal dipole is provided in Figure 3.7.

$$V(t) = \ell \hat{\boldsymbol{t}}_d \cdot \tilde{\boldsymbol{E}}(\bar{\boldsymbol{p}}_{obs}, t) \tag{3.63}$$

The infinitesimal dipole is in itself a directional antenna that receives the entire signal intensity for an electric field that is parallel with the dipole. A positive voltage is generated with fields pointing the same direction of the dipole and negative voltage is generated for

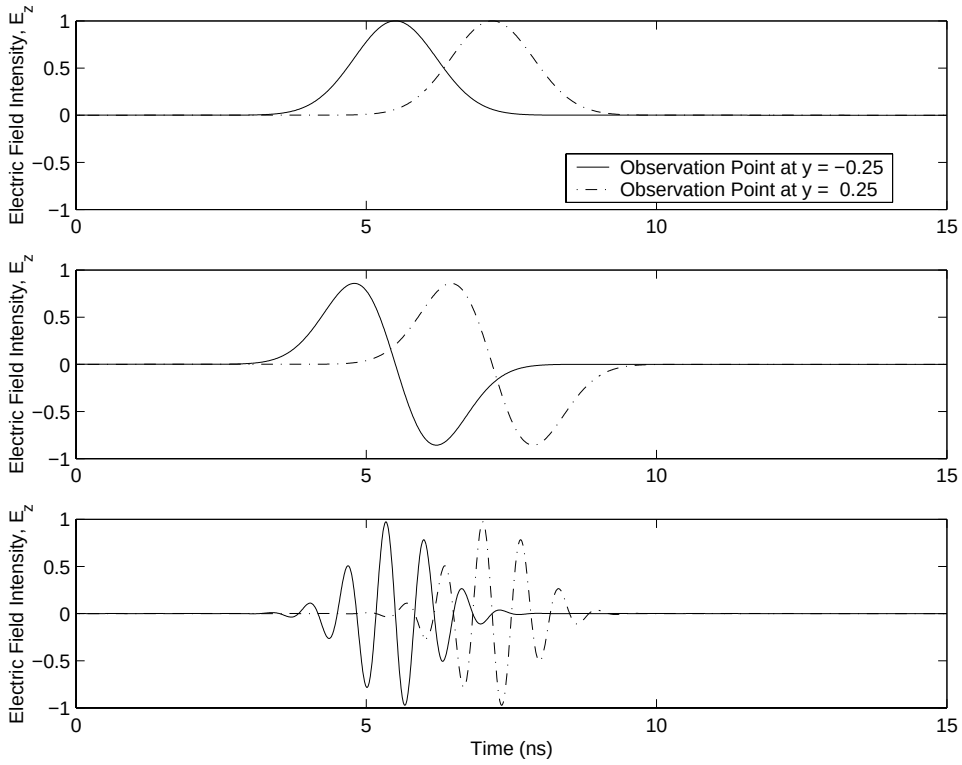

Figure 3.6: Plane wave signals for the Gaussian pulse (equation 3.54), Neumann pulse (equation 3.55) and sinusoid modulated with a Gaussian pulse (equation 3.56). The signal parameters were set to $t_0 = 3$ns, $\tau = 1ns$ and $f = 1.5$ GHz. The frequency for the sinusoid is close to the frequency used at the GPS L1 level.

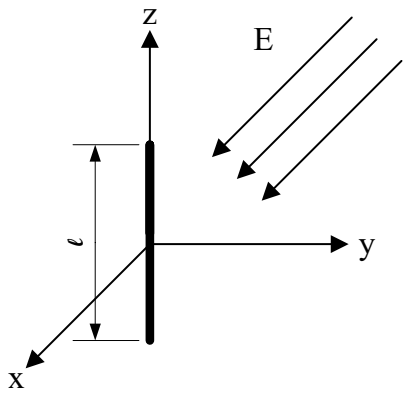

Figure 3.7: Infinitesimal dipole schematic. The dipole is aligned with the z-axis and is of length ℓ. The signal magnitude is a function of the angle formed by the impinging field and the length of the dipole.

parallel fields pointing in the anti-direction of the dipole. The signal reduces by a factor of $\cos\theta$ for fields that are not parallel with the dipole forming an angle θ with the dipole.

The receiving sensor model can be extended to an isotropic antenna by combining three infinitesimal dipoles all perpendicular to each other, e.g., Figure 3.7 could have a dipole on each axis. The voltage signal is then determined by summing the voltage for each independent dipole.

$$V(t) = \sum_{i}^{3} \ell_i \hat{\boldsymbol{t}}_{d_i} \cdot \tilde{\boldsymbol{E}}(\bar{\boldsymbol{p}}_{obs}, t) \tag{3.64}$$

where $\ell_1 = \ell_2 = \ell_3$.

The receiving sensor model can be further customized to a complex directional antenna by modifying the length of each dipole allowing for discretionary contributions from each direction which are different than the infinitesimal dipole model alone.

3.4 Summary

In this chapter, the simulation framework for phases 1 and 2 of Figure 3.2 were discussed. First, the governing equations for the propagation of an electromagnetic wave was presented in detail for both the wave equation formulation and vector potential formulation. It was

discovered that the wave equation formulation is not possible within the FEMLAB software hence requiring the vector potential formulation to be used. The weak form of the vector potential formulation was derived without the scalar potential term.

The details of the finite element simulation were discussed next. Specifics about the geometry definitions, spatial discretization, sampling rates, volume truncation and equation solvers were provided. Some issues specifically related to the FEMLAB application were also discussed as a warning to researchers who may choose to use the same platform in the future.

Finally, the transmitting and receiving models were discussed. The isotropic transmitter was described for three signal shapes from three different source types. The infinitesimal dipole was described for the receiving antenna and the triple dipole was presented as a receiving antenna that can approximate an isotropic receiving antenna.

Chapter 4

Simulation Performance Verification

In this chapter, a set of results using the finite element method provided in Chapter 3 are compared to an analytical solution of an electromagnetic wave travelling through the volume to verify the accuracy of the model solution. It is anticipated that a successful modelling of the simple problem will allow for expansion to a multi-path environment without a significant increase in modelling errors.

Figure 4.1 provides a schematic of the dimensions used in the verification. The region of interest is shown in a light grey and is defined to be 0.50m by 1.00m by 0.50m in the x, y and z directions respectively. An additional region in dark grey with dimensions 0.70m by 1.40m by 0.70m is placed around the region of interest for two purposes: (i) to act as an apron where the absorption boundary conditions affect the travelling wave explicitly and (ii) to act as the input region Ω_i. The input region overlaps the region of interest for 0.1 meters in order to ensure that the spatial derivatives are computed properly at the boundaries and edges.

The apron surrounding the region of interest is set to be 0.1m because it is slightly larger than the maximum element size. This ensures that the apron contains the first layer of elements where the absorbing boundary conditions affect the simulation. An additional 0.20m is added in the $-y$ direction for the input again to allow the spatial derivatives to be properly computed throughout. Finally, a single object has been added in the region of interest that is 0.25m by 0.05m by 0.25m and its center is located at (0.0, 0.2, 0.0).

Formulation 3.7 is used for the governing equations and the electrical properties have been set to be free space throughout.

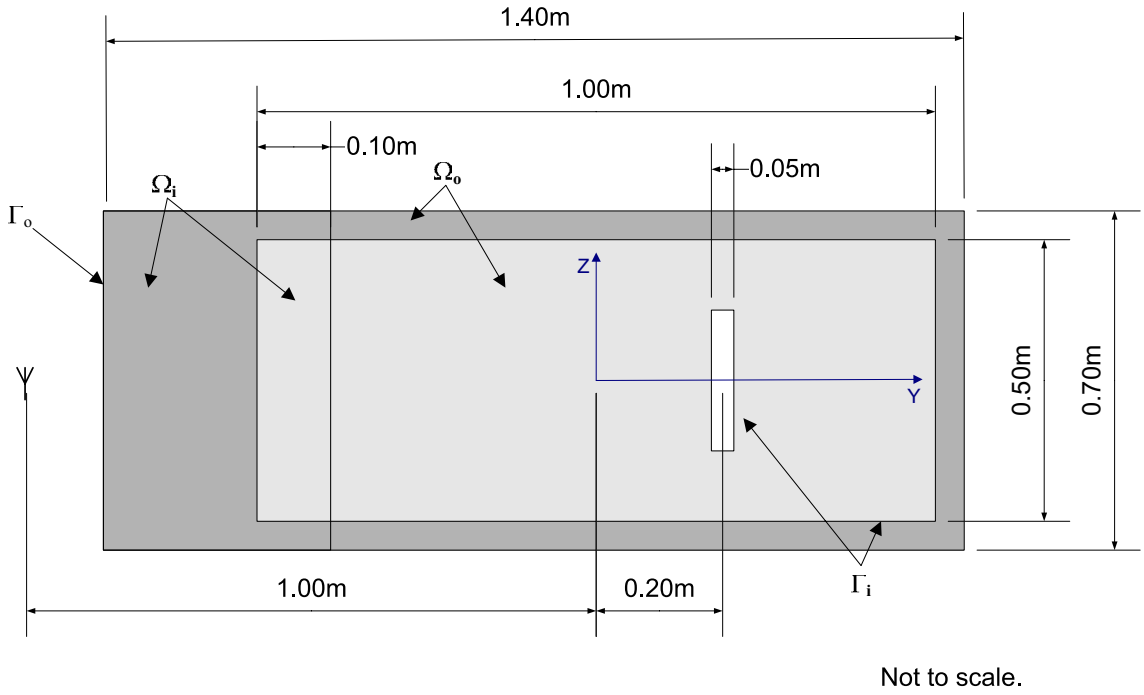

Figure 4.1: Schematic with dimensions used for model validation. The yz and xy plane views are symmetrical. The global coordinate frame for the yz plane is shown in its actual location. The white coloured region is an interference object which for these experiments is considered to have free space material properties to simplify the analytical model. The light grey region is the main volume of interest where the interaction of travelling waves occur. The dark grey region is the input region and the explicit absorption area to satisfy the equation formulation in FEMLAB. The source transmitter is considered to be somewhere to the left of this entire volume and the radiation field is applied to the input region using a Dirichlet condition. The receiving antennas are located at the positions listed in Table 4.3 which occur throughout the light grey volume of interest.

Parameter	**Gaussian Pulse**	**Neumann Pulse**	**Modulated Sine Wave**
t_0	3ns	3ns	3ns
τ	1ns	1ns	1ns
A_0	1	10^{-9}	1
f	-	-	GPS L1: 1.57542 GHz
ω	-	-	$2\pi f$
λ	-	-	c/f
k	-	-	$2\pi/\lambda$
Δt	0.05ns	0.05ns	0.05ns
h_{max}	$\lambda/3$	$\lambda/3$	$\lambda/3$

Table 4.1: Input signal parameters for verification.

The simulation was tested for a Gaussian pulse (equation 3.54), Neumann pulse (equation 3.55) and sinusoid modulated with a Gaussian pulse (equation 3.56) with three different types of source configurations. The electric field sources include sources at infinity (plane waves), line sources (cylindrical waves) and point sources (spherical waves). The parameters common to each source for the input signals are given in Table 4.1. The signal parameters were chosen to be comparable to the GPS frequency range. The sinusoid frequency is set to the GPS L1 frequency and the pulse width was arbitrarily chosen to be 1ns. The Gaussian and Neumann pulses do not have any direct connection with the GPS signals but were set to have similar pulse widths as was arbitrarily defined for the Gaussian modulated sinusoid[1]. The Neumann pulse also has a very small amplitude constant in order to normalize the signal so that it is similar in magnitude to the Gaussian pulse. All verification tests were run for a time period of $0 \leq t \leq 15$ns.

There are 15 test cases summarized in Table 4.2. The test cases vary by source type, signal shape and source location. A single source location is defined for the plane wave since the formulation presented in section 3.3 is only valid for an axis aligned plane wave. Future verification tests should be developed for oblique angled plane waves that would contribute to the realism of the simulation. For the line source, the source is parallel with

[1]It is interesting to note that the pulses implemented with these parameters have a maximum frequency component of approximately 1.5GHz. Although, they were not designed to have this property, it was useful to have all the pulses operating near the same frequency ranges when comparing their results.

No.	Source Type	Signal Shape	Source Location
1	Infinite	Gaussian Pulse	$y = -1.00$
2	Infinite	Neumann Pulse	$y = -1.00$
3	Infinite	Mod. Sinusoid	$y = -1.00$
4	Line	Gaussian Pulse	$y = -1.00, z = 0.00$
5	Line	Neumann Pulse	$y = -1.00, z = 0.00$
6	Line	Mod. Sinusoid	$y = -1.00, z = 0.00$
7	Point	Gaussian Pulse	$(0.00, -1.00, 0.00)$
8	Point	Neumann Pulse	$(0.00, -1.00, 0.00)$
9	Point	Mod. Sinusoid	$(0.00, -1.00, 0.00)$
10	Line	Gaussian Pulse	$y = -1.00, z = 0.25$
11	Line	Neumann Pulse	$y = -1.00, z = 0.25$
12	Line	Mod. Sinusoid	$y = -1.00, z = 0.25$
13	Point	Gaussian Pulse	$(0.00, -1.00, 0.25)$
14	Point	Neumann Pulse	$(0.00, -1.00, 0.25)$
15	Point	Mod. Sinusoid	$(0.00, -1.00, 0.25)$

Table 4.2: List of verification test cases.

the x-axis and is placed at two locations, (i) $y = -1.00, z = 0.00$ and (ii) $y = -1.00, z = 0.25$. The point source locations are similarly placed at (i) $(0.00, -1.00, 0.00)$ and (ii) $(0.00, -1.00, 0.25)$.

For each test case the time domain signal is sampled at 27 locations throughout the volume. The sampling locations are listed in Table 4.3. The electric field components E_x, E_y and E_z are collected at each sample location and compared against an analytically derived solution. The root-mean-square statistic is computed by the following formula.

$$RMS = \sqrt{\frac{1}{N}\sum_{i=1}^{N}\left(s_m\left(t_i\right) - s_r\left(t_i\right)\right)^2} \tag{4.1}$$

where $s_m\left(t_i\right)$ is the measured signal (FEM model solution) at time step t_i, $s_r\left(t_i\right)$ is the reference signal (analytical model solution) at time t_i and N is the number of time steps sampled. The signals that are expected to attenuate (cylindrical and spherical sources) are normalized so that the absolute maximum of the reference signal is 1.0. The normalization

Signal No.	**Signal Location**		
	x	y	z
1	0.0000	-0.4000	0.0000
2	0.1000	-0.4000	0.0000
3	0.0000	-0.4000	0.1000
4	0.0000	-0.3000	0.0000
5	0.1000	-0.3000	0.0000
6	0.0000	-0.3000	0.1000
7	0.0000	-0.2000	0.0000
8	0.1000	-0.2000	0.0000
9	0.0000	-0.2000	0.1000
10	0.0000	-0.1000	0.0000
11	0.1000	-0.1000	0.0000
12	0.0000	-0.1000	0.1000
13	0.0000	0.0000	0.0000
14	0.1000	0.0000	0.0000
15	0.0000	0.0000	0.1000
16	0.0000	0.1000	0.0000
17	0.1000	0.1000	0.0000
18	0.0000	0.1000	0.1000
19	0.0000	0.2000	0.0000
20	0.1000	0.2000	0.0000
21	0.0000	0.2000	0.1000
22	0.0000	0.3000	0.0000
23	0.1000	0.3000	0.0000
24	0.0000	0.3000	0.1000
25	0.0000	0.4000	0.0000
26	0.1000	0.4000	0.0000
27	0.0000	0.4000	0.1000

Table 4.3: List of sampling locations.

allows for the statistics of the three different source types to be compared easily.

The results are presented in the following sections in the order of increasing dimensionality of the source type.

4.1 Sources at Infinity: Plane Waves

The plane waves in this simulation were defined to be propagating in the $+y$ direction $\left(\bar{\boldsymbol{d}} = \begin{bmatrix} 0 & 1 & 0 \end{bmatrix}^T\right)$ with an E_z component. A source location was defined to be at $(0.0, -1.0, 0.0)$ but was only used as a reference location to calculate the spatial component of the wave. It was not expected that the plane waves would exhibit any sort of attenuation since the free space material was lossless so there was no attenuating factor added to the signal input model. The remaining signal properties are defined in Table 4.1.

The measured electric field signals for sampling location number 13 (global origin in Figure 4.1) are plotted for (i) Gaussian pulse in Figure 4.2, (ii) Neumann pulse in Figure 4.3 and (iii) modulated sinusoid in Figure 4.4. The RMS statistics are shown in Table C.1 on page 127 and are presented graphically in Figure 4.5. The statistics were normalized so that the absolute maximum of the reference signal was set to 1.00[2].

It is clear from Figures 4.2 and 4.3 that the Gaussian pulse and Neumann pulse signals do not match the reference value very well. The signals are attenuated quite drastically. The modulated sinusoid is also different from the reference, but here the more obvious error is the phase shift in the signal as the peaks in the signal are much less attenuated than the pulse signals. Further examples of the signal attenuation for the Neumann pulse are shown in Figures C.1 to C.6 in Appendix C (pages 128-130). The attenuation of the signal is due to the absorbing boundary conditions introduced at the boundaries in this particular formulation. Removing the absorbing boundary conditions allows for better agreement with the reference signal but the signal is fully reflected off of the boundary on the $+y$ axis.

The modulated sinusoid also exhibits some reflection of its signal off of the truncation boundary that is intersected by the $+y$ axis (see Figure 4.1). The additional oscillations that are seen past 8ns in the E_z component can be attributed to some partial reflection that

[2]For the plane wave source, the normalization of the signals only affects the Neumann pulse slightly as the references signals have a maximum amplitude at 1.00 or close to 1.00 for all observation points.

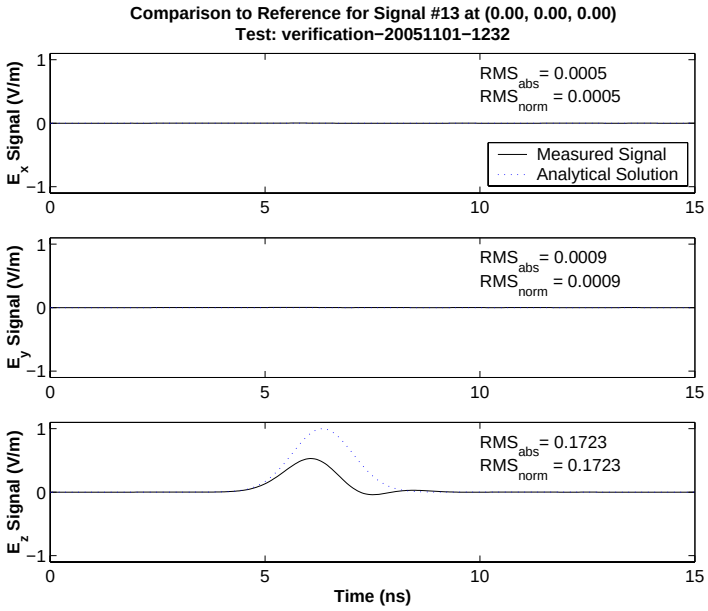

Figure 4.2: Electric field intensity for a plane wave with Gaussian pulse at location (0.00, 0.00, 0.00).

was expected with the absorbing boundary conditions that were implemented. In fact, it was surprising to see how well the absorbing boundary conditions worked for the Gaussian and Neumann pulses. However, they were not as successful for the modulated sinusoid in the E_x and E_y components. The oscillations in these components were not expected and were observed using a time animation to be generated directly at the boundary and propagate towards the middle.

Finally, Figure 4.5 shows that the error for the 27 sample locations increases as the sample number increases. The sample number corresponds roughly with the distances travelled by the signal in the y-direction. In fact, it can be seen that there are steps in the RMS error plots for Gaussian and Neumann pulse steps that correspond to the three signals at $y = -0.4$ followed by $y = -0.3$ etc. The modulated sinusoid has a more random error profile, although it is definitely increasing as the signal moves away from the source, the results do not show a smooth trend like the pulse signals. This is attributed to the fact that the signal moves in and out of phase with the reference signal as it propagates in the $+y$-direction.

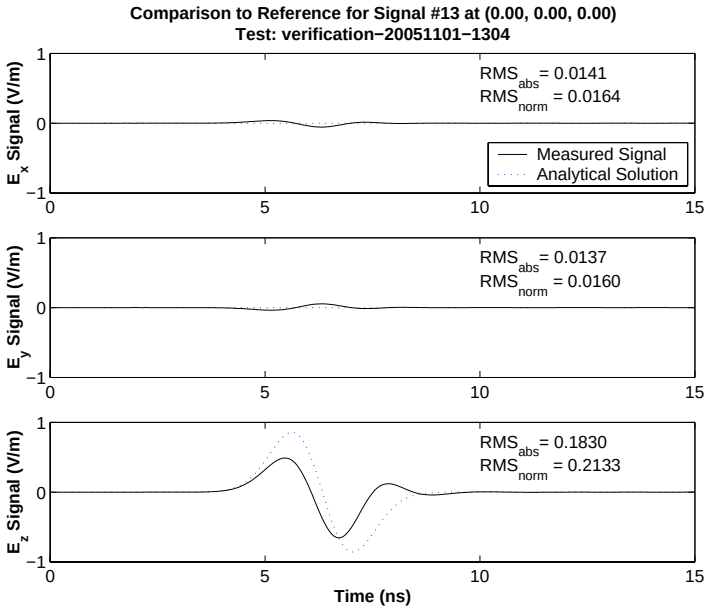

Figure 4.3: Electric field intensity for a plane wave with Neumann pulse at location (0.00, 0.00, 0.00).

The phase error is the most significant error present in this verification testing. At first analysis it was expected the phase error was a local phenomena that would be negligible for a group of sensors grouped near each other. In fact, this would be expected if an attenuating object is present not only reducing the magnitude of the signal but also slowing the phase velocity of the signal resulting in a signal that is out of phase with a reference signal in free space. However, it was discovered using the results in Chapter 5 that the phase error is a function of the vector finite elements that are used and are not a locally contained phenomena. More details on this issue are provided in Section 5.2.

4.2 Line Sources: Cylindrical Waves

The cylindrical waves in this simulation were defined to be propagating in the y and z directions $\left(\bar{\boldsymbol{d}} = \begin{bmatrix} 0 & 1 & 1 \end{bmatrix}^T\right)$ with E_z and E_y components. The source location was defined to be at (i) $y = -1.00, z = 0.00$ and (ii) $y = -1.00, z = 0.25$ which are lines that run parallel with the x axis. For a cylindrical wave, the signal attenuates as a function

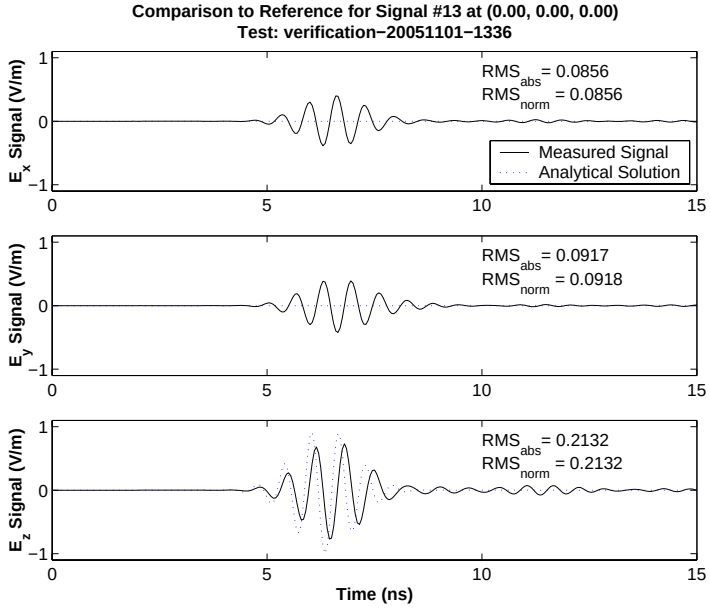

Figure 4.4: Electric field intensity for a plane wave with sinusoid modulated with a Gaussian pulse at location (0.00, 0.00, 0.00).

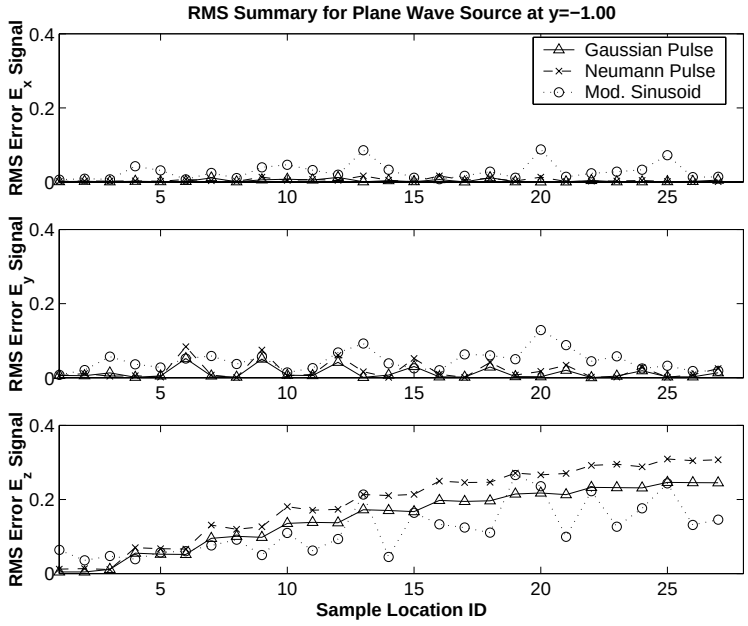

Figure 4.5: RMS summary for plane wave source at $y = -1.00$.

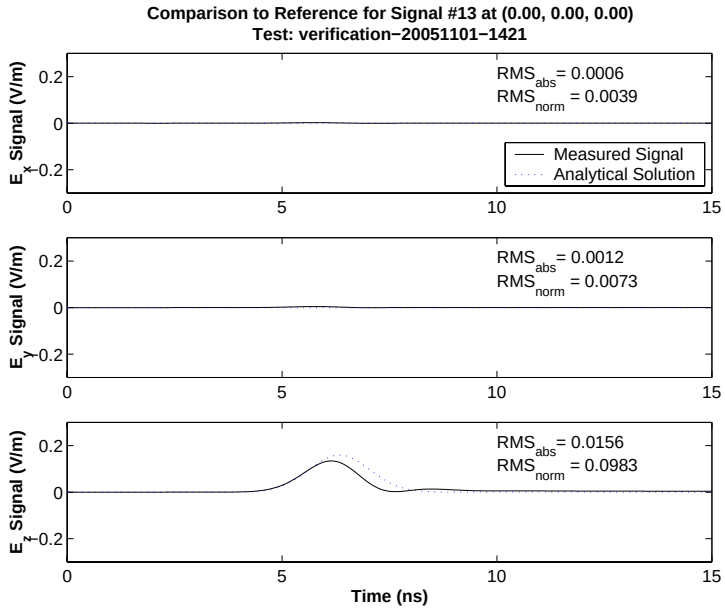

Figure 4.6: Electric field intensity for a cylindrical wave with Gaussian pulse.

of the distance from source to observation by a factor of $1/2\pi|\bar{\boldsymbol{r}}|$. The remaining signal properties are defined in Table 4.1.

The results for the first source location for sampling location number 6 (global origin in Figure 4.1) are plotted in Figure 4.6 for the Gaussian pulse, Figure 4.7 for the Neumann pulse and Figure 4.8 for the modulated sinusoid. The RMS statistics are shown in Table C.2 on page 131 and are presented graphically in Figure 4.9. The statistics are normalized so that the absolute maximum of the reference signal is set to 1.00. Similarly, the results for the second source location follow in Figure 4.10 for the Gaussian pulse, Figure 4.11 for the Neumann pulse and Figure 4.12 for the modulated sinusoid with the RMS statistics shown in Table C.3 (page 132) and Figure 4.13. Additional plots for the Neumann pulse at 6 other observation points are provided in Figures C.7 to C.12 in Appendix C (pages 133-135).

The results for the cylindrical wave are similar to that as the plane wave except that the errors observed previously are not as significant here. As mentioned above, it is expected that there will be some attenuation in the cylindrical wave as a function of distance from the source. Figures 4.9 and 4.13 show that there is some additional attenuation as the

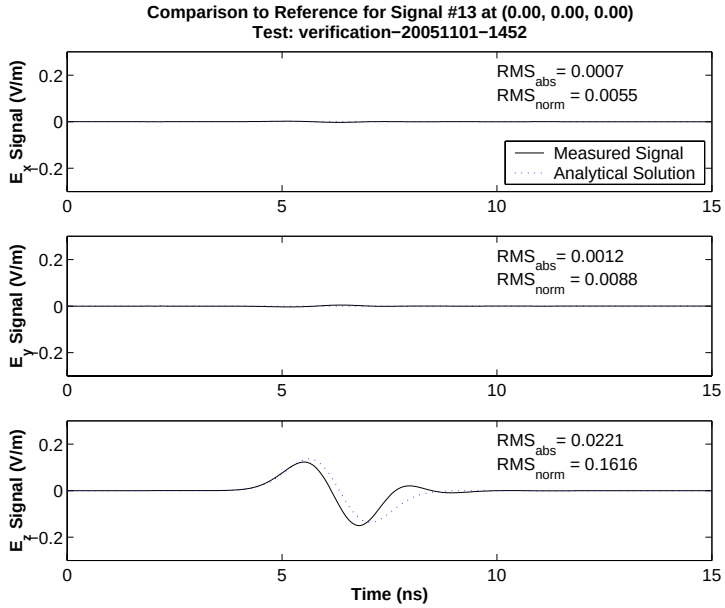

Figure 4.7: Electric field intensity for a cylindrical wave with Neumann pulse.

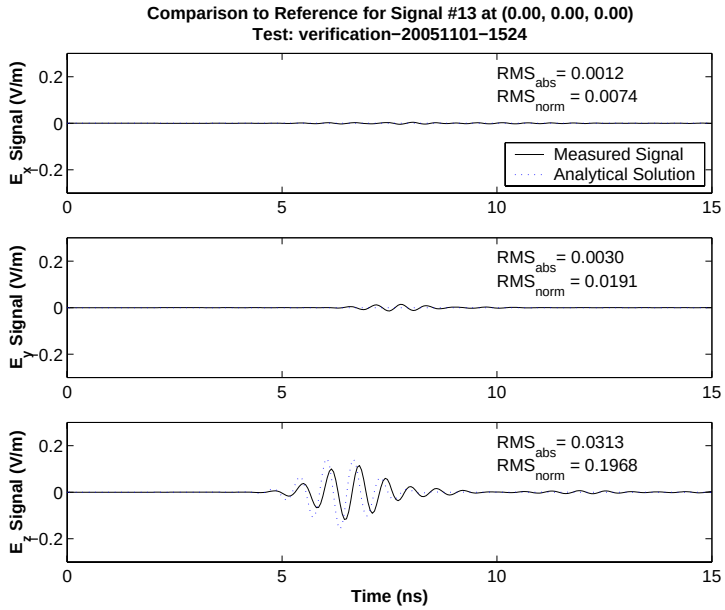

Figure 4.8: Electric field intensity for a cylindrical wave with sinusoid modulated with a Gaussian pulse.

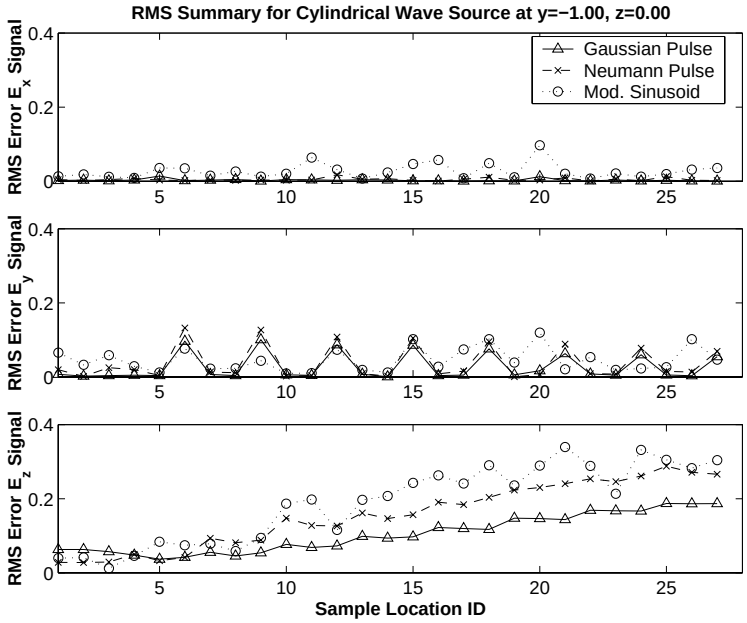

Figure 4.9: RMS summary for line source at $y = -1.00, z = 0.00$.

error curves show an upward trend as the index increases. The amount of error attributed to the additional attenuation is less than the plane wave by about 0.05 in the normalized RMS statistic for the Gaussian and Neumann statistics at the furthest distance away.

However, the modulated sinusoid shows some contradicting results which can be seen by observing that the error on the E_x and E_y components are much better but, the normalized RMS statistics in 4.9 are much higher than the previous plane wave experiment. The error in the E_x component is negligible for future signal processing procedures and the E_y component is only slightly out of phase of its reference but is in phase with the E_z component.

Similar observations can be made for the second set of line sources that were placed at $y = -1.00, z = 0.25$. The only significant difference between the two sets of experiments is in the E_y error. In Figure 4.13, the E_y error statistics start out very low (< 0.05), jump to approximately 0.2 and then gradually fall to a value less than 0.05. The jump in the error curves exists because the first three sampling points lie on the input boundary and are subject to the Dirichlet condition in the input region. The gradual decay in the error is due to a phase error that is introduced close to the source and is eventually removed as

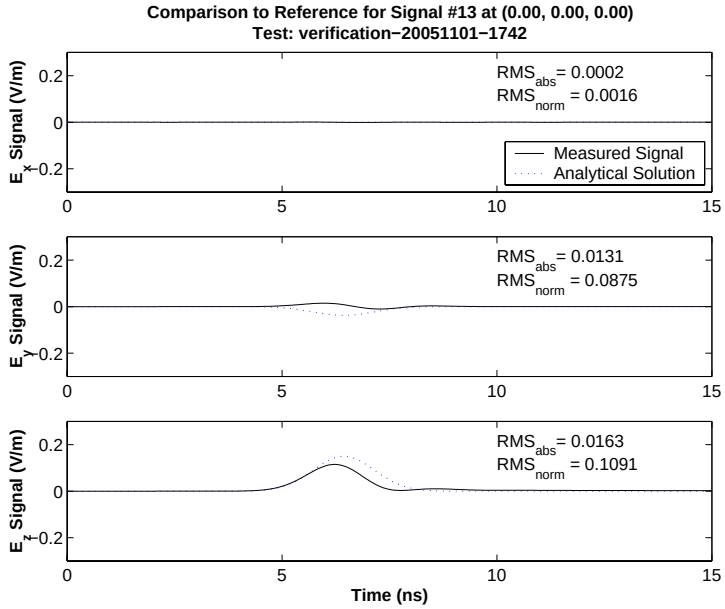

Figure 4.10: Electric field intensity for a cylindrical wave with Gaussian pulse and different source location.

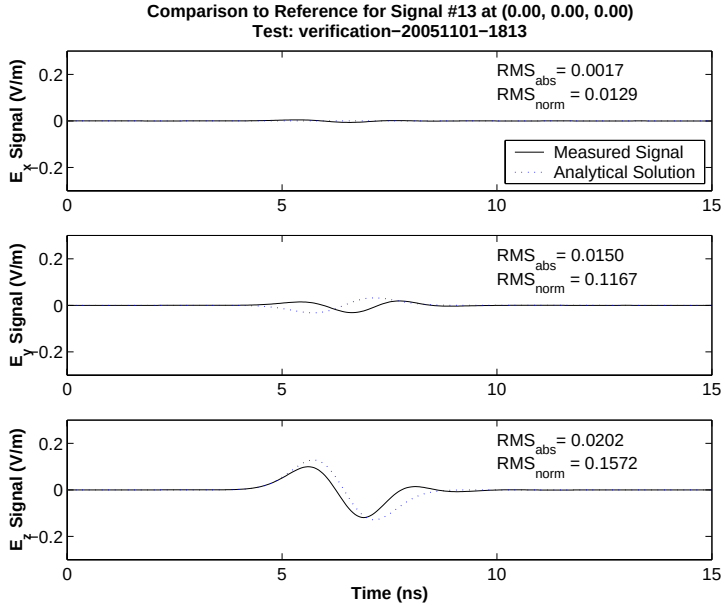

Figure 4.11: Electric field intensity for a cylindrical wave with Neumann pulse and different source location.

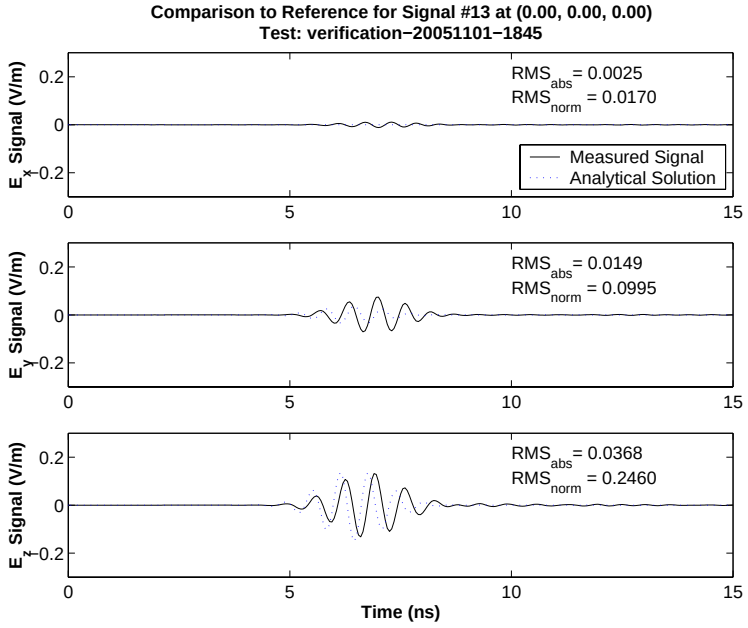

Figure 4.12: Electric field intensity for a cylindrical wave with sinusoid modulated with a Gaussian pulse and different source location.

the simulated and reference signals come into phase.

Similarly to the plane waves, the phase error is the most significant error in the verification. Details of the effect of this error are found in Section 5.2.

4.3 Point Sources: Spherical Waves

The cylindrical waves in this simulation were defined to be propagating uniformly in all directions $\left(\bar{\boldsymbol{d}} = \begin{bmatrix} 1 & 1 & 1 \end{bmatrix}^T\right)$ with E_x, E_y and E_z components. The source location was defined to be at (i) $(0.00, -1.00, 0.00)$ and (ii) $(0.00, -1.00, 0.25)$. For a spherical wave, the signal attenuates as a function of the distance from source to the observation point by a factor of $1/4\pi|\bar{\boldsymbol{r}}|^2$. The remaining signal properties are defined in Table 4.1.

The results for the first source location for sampling location number 6 (global origin in Figure 4.1) are plotted in Figure 4.14 for the Gaussian pulse, Figure 4.15 for the Neumann pulse and Figure 4.16 for the modulated sinusoid. The RMS statistics are shown in Table C.4 and are presented graphically in Figure 4.17. The results for the second source location

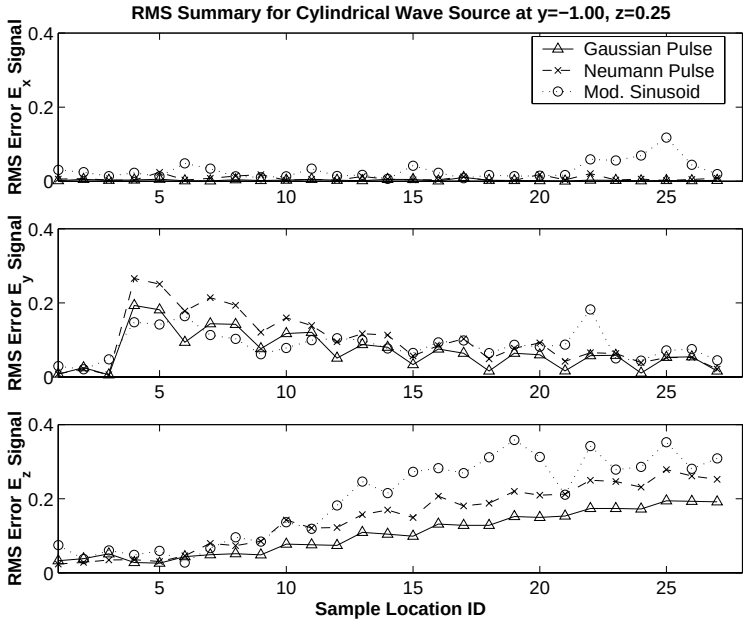

Figure 4.13: RMS summary for line source at $y = -1.00, z = 0.25$.

follow in Figure 4.18 for the Gaussian pulse, Figure 4.19 for the Neumann pulse and Figure 4.20 for the modulated sinusoid with the RMS statistics shown in Table C.5 and Figure 4.21. Additional plots for the Neumann pulse at 6 other observation points are provided in Figures C.13 to C.18 in Appendix C (pages 138-140).

The spherical wave shows similar properties as that of the cylindrical waves. However, there is one observation in both signals that has not yet been discussed. The E_y for the point source at $(0.00, 0.00, 0.00)$ has a very distinct pattern where every third observation point is significantly higher for the Gaussian pulse. These signals correspond to the observation points at $z = 0.10$. Clearly, an additional error is introduced in the z-direction and is likely caused by the absorbing boundary condition in that direction.

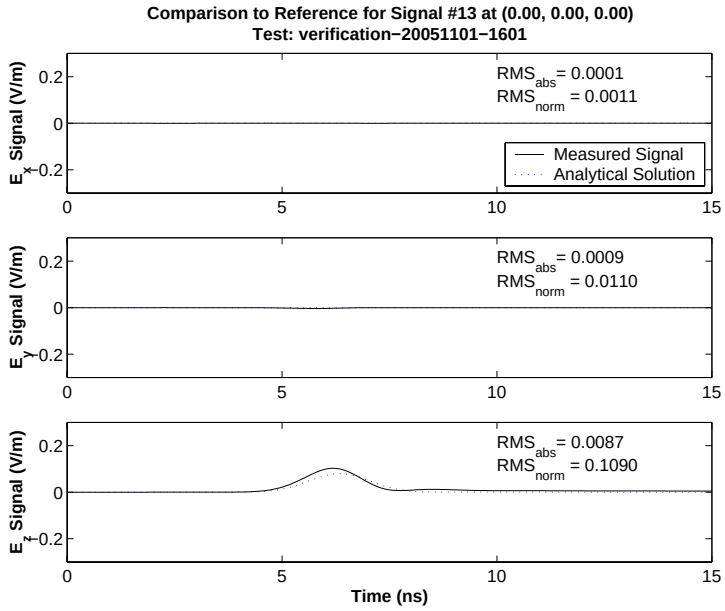

Figure 4.14: Electric field intensity for a spherical wave with Gaussian pulse.

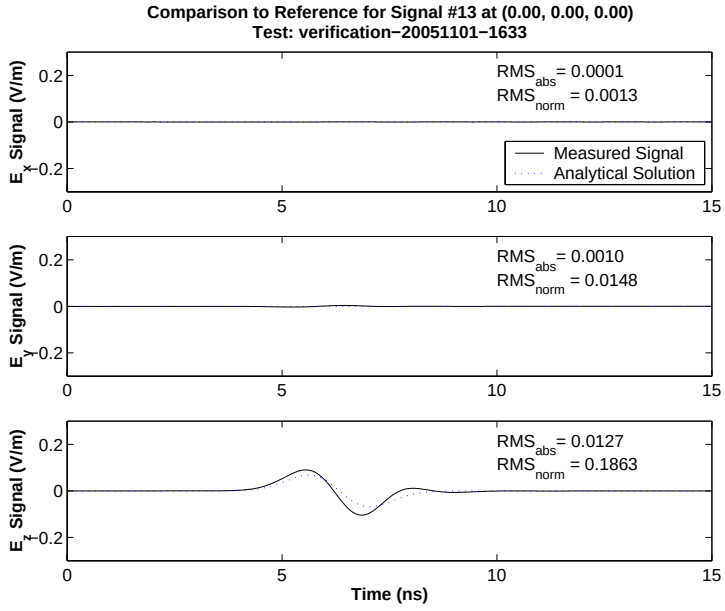

Figure 4.15: Electric field intensity for a spherical wave with Neumann pulse.

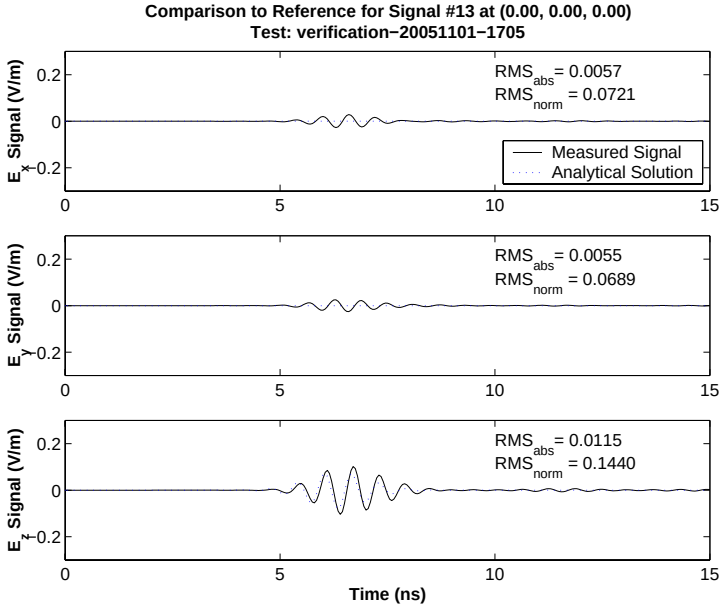

Figure 4.16: Electric field intensity for a spherical wave with sinusoid modulated with a Gaussian pulse.

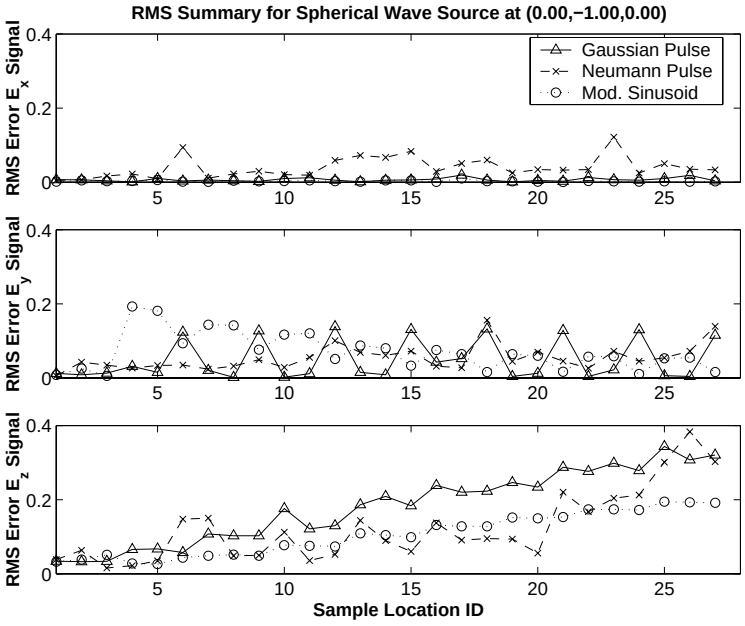

Figure 4.17: RMS summary for point source at $(0.00, -1.00, 0.00)$.

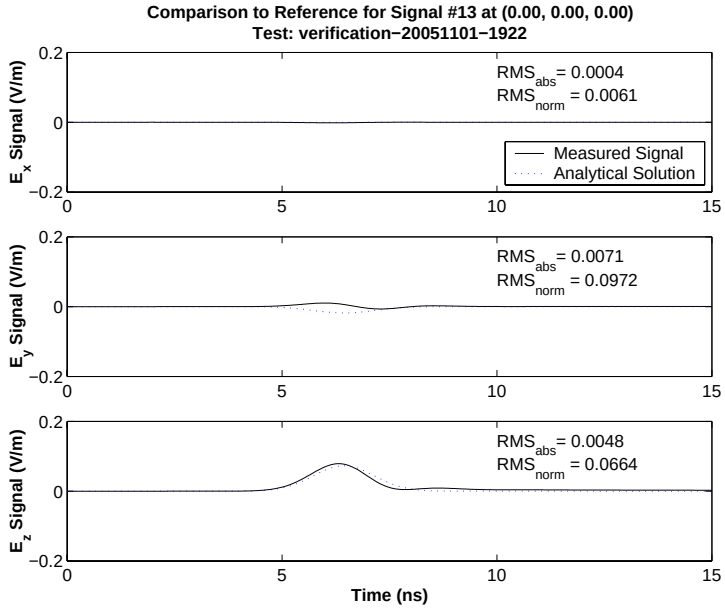

Figure 4.18: Electric field intensity for a spherical wave with Gaussian pulse and different source location.

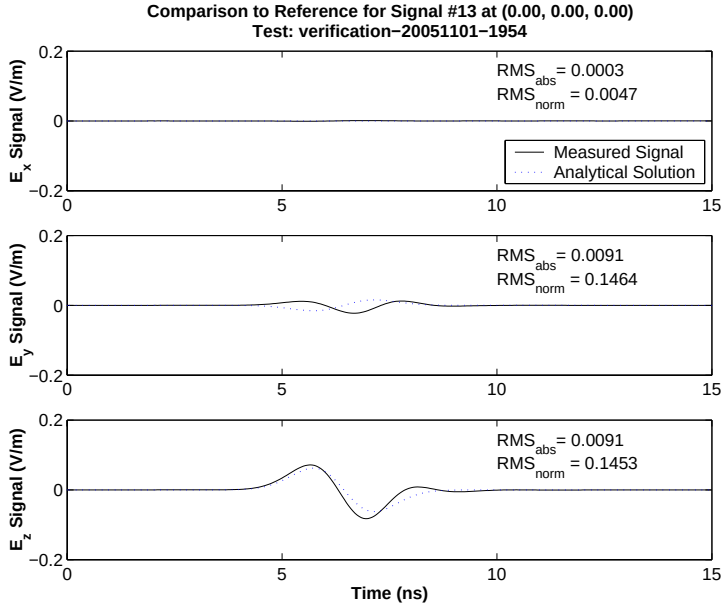

Figure 4.19: Electric field intensity for a spherical wave with Neumann pulse and different source location.

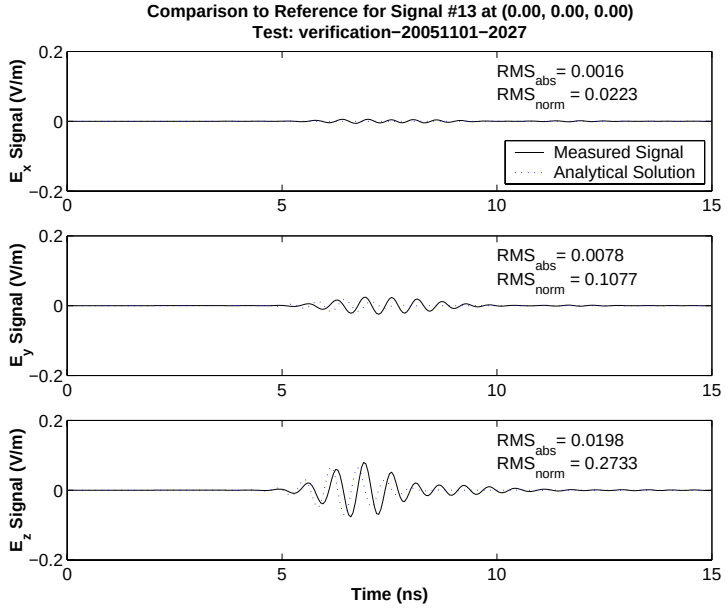

Figure 4.20: Electric field intensity for a spherical wave with sinusoid modulated with a Gaussian pulse and different source location.

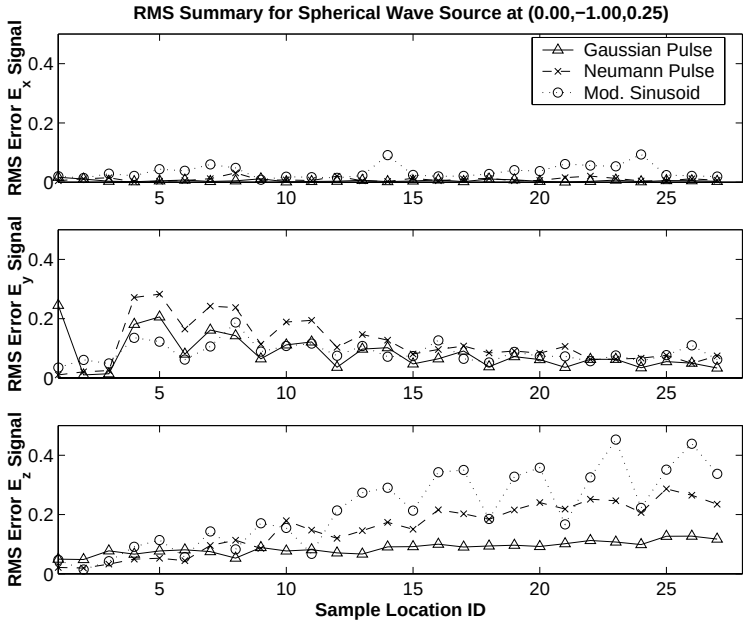

Figure 4.21: RMS summary for point source at $(0.00, -1.00, 0.25)$.

4.4 Verification Summary

Clearly the results of the finite element method presented here are not outstanding as they do not match the analytical solutions very well. It was first expected that the small errors introduced by the boundary conditions and the vector finite elements method would be negligible in the long run. However, the phase errors introduced by the vector finite elements (see Section 5.2) are not locally negligible.

In the future, additional volume truncation methods should be investigated such as the perfectly matched layer (see section 3.2). This method allows for the signal to be passed into a separate region where it is absorbed without affecting the region of interest as it does in the results presented here. Also, higher order vector elements need to be used in order to significantly reduce the phase error (see Section 5.2) that is introduced by the zeroth order elements used in the results presented in this chapter.

For the work in Chapter 5, a single signal shape should be chosen for use in the position measurement algorithm investigations. The Neumann pulse is the signal that should be chosen for two reasons. The Neumann pulse has a very distinct shape that can be used for easy identification in noisy data. Highly attenuated Gaussian pulses and noisy modulated sinusoids would be difficult to use as a first pass, although their efficiency should be investigated at a later date. Other future work would include reproducing this simulation with other finite element analysis tool sets to confirm the results obtained.

With phases 1 and 2 as described in Figure 3.2 completely described, Chapter 5 describes the algorithms and testing performed for phase 3 of the research. It also provides more details on the effect that the phase error has on the quality of the simulation framework.

Chapter 5

Position Determination using the Time Difference of Arrival Algorithm

This chapter introduces some of the concepts required for phase 3 of the simulation process shown in Figure 3.2 on page 33. First, two specific position determination algorithms using time difference of arrival are discussed. The chosen time difference of arrival algorithm is then implemented using the signals derived from phases 1 and 2 of the simulation process. Unfortunately, it is shown here that the quality of the simulation process is poor due to the order of the vector finite elements that are available within the FEMLAB software.

5.1 Time Difference of Arrival Algorithms, Theory and Performance

The time difference of arrival method (TDOA) was first introduced in section 2.2.1 on page 23. In this section, two methods of using the time difference of arrival is presented and the advantages and disadvantages of each method are discussed. The first method is a linearized approximate solver that solves the set of hyperbolic equations. The second method uses groups of sensors to generate a bearing line. Two or more groups of sensors can then be used to find the intersection (or near intersections) of the bearing lines to get a position determination. Finally, the method measuring the time difference of arrival between two signals at independent locations is discussed.

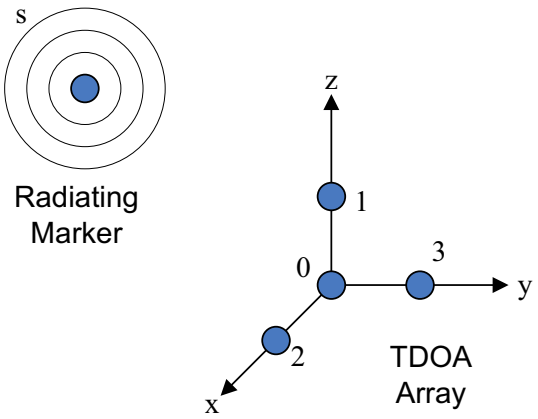

Figure 5.1: Example of time difference of arrival method.

5.1.1 Linearized Approximation Method

The closed form linearized approximation (LA) is well documented in the literature [7, 56, 58] but Mellen et al. [29] presents the most general and straightforward method of the group.

The Mellen method uses N antennas to receive signals from a given transmitting marker. The time delay between a pair of antennas creates a hyperbolic equation. With N antennas, a set of hyperbolic equations can be created for $N-1$ pairs of antennas where each pair includes the assigned reference antenna typically labelled as sensor 0. The intersection of the hyperbolic curves is the location of the source marker.

Figure 5.1 shows an example time difference of arrival configuration using the minimum 4 sensor system configuration with source marker s. The locations of a sensor array with N sensors are defined in equation 5.1.

$$\bar{\boldsymbol{p}}_0 = \begin{bmatrix} x_0 \\ y_0 \\ z_0 \end{bmatrix} = \begin{bmatrix} 0 \\ 0 \\ 0 \end{bmatrix}, \bar{\boldsymbol{p}}_i = \begin{bmatrix} x_i \\ y_i \\ z_i \end{bmatrix} \quad i = 1, \ldots, N \tag{5.1}$$

The location of the source signal is represented by

$$\bar{\boldsymbol{p}}_s = \begin{bmatrix} x_s \\ y_s \\ z_s \end{bmatrix}. \tag{5.2}$$

The time differences are taken with respect to the reference sensor marked as sensor 0. The time differences are represented mathematically to be

$$\tau_i = t_i - t_0 \quad i = 1, \ldots, N \tag{5.3}$$

where t_0 is the absolute time of arrival at sensor 0 and t_i is the absolute time of arrival at sensor i. Note that the absolute times of arrival are not actually determined and only the difference τ_i is computed.

The range difference d_i is the difference in distance travelled by the radiating signal to sensor i relative to sensor 0 and is computed using the speed of light.

$$d_i = c_0 \tau_i \quad i = 1, \ldots, N \tag{5.4}$$

The range differences d_i are also related to the difference in the Euclidean distance of the source from a given sensor and the Euclidean distance of the source from the reference sensor.

$$d_i = \sqrt{(x_i - x_s)^2 + (y_i - y_s)^2 + (z_i - z_s)^2} - \sqrt{x_s^2 + y_s^2 + z_s^2} \quad i = 1, \ldots, N \tag{5.5}$$

Rearranging equation 5.5 results in

$$x_i x_s + y_i y_s + z_i z_s + d_i \sqrt{x_s^2 + y_s^2 + z_s^2} = \frac{1}{2}\left(x_i^2 + y_i^2 + z_i^2 - d_i^2\right) \quad i = 1, \ldots, N \tag{5.6}$$

which results in $N - 1$ equations and three unknowns providing an over determined set of equations.

The over determined set of equations can be solved using a linearized least squares solution. First, the equation 5.6 needs to be represented in matrix form as follows.

$$\boldsymbol{A} = \begin{bmatrix} \bar{\boldsymbol{p}}_1{}^T \\ \vdots \\ \bar{\boldsymbol{p}}_N{}^T \end{bmatrix} = \begin{bmatrix} x_1 & y_1 & z_1 \\ \vdots & \vdots & \vdots \\ x_N & y_N & z_N \end{bmatrix} \tag{5.7}$$

$$\bar{\boldsymbol{b}} = \frac{1}{2} \begin{bmatrix} x_1^2 + y_1^2 + z_1^2 - d_1^2 \\ \vdots \\ x_N^2 + y_N^2 + z_N^2 - d_N^2 \end{bmatrix} \tag{5.8}$$

$$\bar{\boldsymbol{d}} = \begin{bmatrix} d_1 \\ \vdots \\ d_N \end{bmatrix} \tag{5.9}$$

The above matrix and vectors allow for equation 5.6 to be written as

$$\boldsymbol{A}\bar{\boldsymbol{p}}_s = \bar{\boldsymbol{b}} - \bar{\boldsymbol{d}}R_s, \tag{5.10}$$

where

$$R_s = \sqrt{x_s^2 + y_s^2 + z_s^2}. \tag{5.11}$$

This resembles a linear system of equations with four unknowns. The position of the sensor can be isolated by multiplying both sides by $\boldsymbol{A}^T$ and then multiplying by $\left(\boldsymbol{A}^T\boldsymbol{A}\right)^{-1}$ to get

$$\bar{\boldsymbol{p}}_s = \left(\boldsymbol{A}^T\boldsymbol{A}\right)^{-1}\boldsymbol{A}^T\bar{\boldsymbol{b}} - \left(\boldsymbol{A}^T\boldsymbol{A}\right)^{-1}\boldsymbol{A}^T\bar{\boldsymbol{d}}R_s. \tag{5.12}$$

This formulation can be rewritten as

$$\bar{\boldsymbol{p}}_s = \bar{\boldsymbol{\alpha}} - \bar{\boldsymbol{\beta}}R_s = \begin{bmatrix} \alpha_1 \\ \alpha_2 \\ \alpha_3 \end{bmatrix} - \begin{bmatrix} \beta_1 \\ \beta_2 \\ \beta_3 \end{bmatrix} R_s \tag{5.13}$$

where $\bar{\boldsymbol{\alpha}} = \left(\boldsymbol{A}^T\boldsymbol{A}\right)^{-1}\boldsymbol{A}^T\bar{\boldsymbol{b}}$ and $\bar{\boldsymbol{\beta}} = \left(\boldsymbol{A}^T\boldsymbol{A}\right)^{-1}\boldsymbol{A}^T\bar{\boldsymbol{d}}$. Equation 5.11 can be substituted into equation 5.13 which creates the quadratic equation

$$\left(\beta_1^2 + \beta_2^2 + \beta_3^2 - 1\right)R_s^2 - 2R_s\left(\alpha_1\beta_1 + \alpha_2\beta_2 + \alpha_3\beta_3\right) + \alpha_1^2 + \alpha_2^2 + \alpha_3^2. \tag{5.14}$$

	RMS	Mean	Std. Dev.	Max	Min
x	0.1713	0.0000	0.1746	0.2994	-0.2994
y	0.2817	0.2226	0.1759	0.4909	-0.1764
z	0.1758	-0.0253	0.1773	0.2882	-0.2467
3D	0.3736	0.3415	0.1545	0.5616	0.0594

Table 5.1: Sample statistics for the linearized approximation method. All statistics are in meters. The RMS statistics provides a general relationship that combines the trueness and precision. If the error distribution is Gaussian, the mean is an indicator of trueness (bias) while the standard deviation is an indicator of precision. The maximum and minimum errors provide information on the range of the data. Component errors are useful when trying to isolate specific error phenomena while the 3D distance error is useful as a general overall error statistic.

The quadratic equation has two solutions which can be found using the quadratic formula [52]. The solution for R_s can be substituted back into equation 5.13 which finally provides a solution for $\bar{\boldsymbol{p}}_s$.

Unfortunately, this method is not very accurate relative to the specifications provided in Chapter 1. The algorithm was tested using a four sensor system with the sensors in the array located at

$$\begin{aligned}
\bar{\boldsymbol{p}}_{a1} &= \begin{bmatrix} 0.00 & 0.00 & 0.00 \end{bmatrix}^T \\
\bar{\boldsymbol{p}}_{a2} &= \begin{bmatrix} 0.50 & 0.50 & 0.00 \end{bmatrix}^T \\
\bar{\boldsymbol{p}}_{a3} &= \begin{bmatrix} -0.50 & 0.50 & 0.00 \end{bmatrix}^T \\
\bar{\boldsymbol{p}}_{a4} &= \begin{bmatrix} 0.00 & 0.00 & 0.50 \end{bmatrix}^T .
\end{aligned} \tag{5.15}$$

The algorithm was tested for a configuration similar to the one introduced in Figure 3.1 on page 31. The source marker was tested at 27 locations that were uniformly distributed in a 3 by 3 by 3 grid that extends from -0.5 to 0.5 in the x- and z-axes and extends from -0.6 to -1.0 in the y-axis. The specific locations are listed in Table D.1 in Appendix D with the summary statistics presented in Table 5.1. The time differences of arrival were computed as exact values using the $c_0 = r_i/t_i$ and $\tau_i = t_i - t_0$ relationship. Table D.1 also

provides the computed positions using the algorithm and the errors between the actual and computed positions.

The overall distance root mean square error was found to be $RMS_{3D} = 0.374$m which is clearly unusable for the applications first described in Chapter 1 where centimeter ($RMS_{3D} = 0.010$m) and millimeter ($RMS_{3D} = 0.001$m) accuracy is sought. This algorithm was deemed to be particularly poor since the time differences that were computed are exact values and not measured values. Other array configurations were tested but met with similar results that are further supported by Smith et al. who present other results that support this conclusion [58]. It is also interesting to note that the there exists a significant bias in the y component. This error is typical of triangulation algorithms along the viewing axis, which is the y-axis in this case. However, the error along all axes are still too high for useful application of this algorithm.

5.1.2 Intersection of Headings Method

The intersection of headings (IH) method uses the time difference of arrivals for specific groups of sensors to compute a heading, also known as a bearing line [13, 26]. The bearing line is determined by using a quadruple sensor arrangement as shown in Figure 5.2. Two pairs of sensors, S_{12} and S_{34}, are located along the x- and y-axes of the local coordinate system respectively. The sensors are placed so that the midpoint between each pair is located at the origin of the local coordinate system. The time difference of arrival between the two sensors in a given pair defines a hyperboloid that can be approximated by a cone that has a vertex at the midpoint between the two sensors, an axis of symmetry along the line joining the two sensors and an apex angle given by

$$\theta = \cos^{-1}\left(\frac{c_0 \Delta t}{|\bar{\boldsymbol{p}}_i - \bar{\boldsymbol{p}}_j|}\right). \tag{5.16}$$

$\bar{\boldsymbol{p}}_i$ is the position for sensor i, $\bar{\boldsymbol{p}}_j$ is the position for sensor j where i and j are either 1 and 2 respectively or 3 and 4 respectively, c_0 is the speed of light and τ is the time difference between the sensors in the pair.

The apex of the angle can be interpreted to be the direction angle for the axis aligned with the given sensor pair. Specifically, the angle found for the sensor pair S_{12} is the angle formed with the x axis can be defined as α and the angle found with the second pair S_{34}

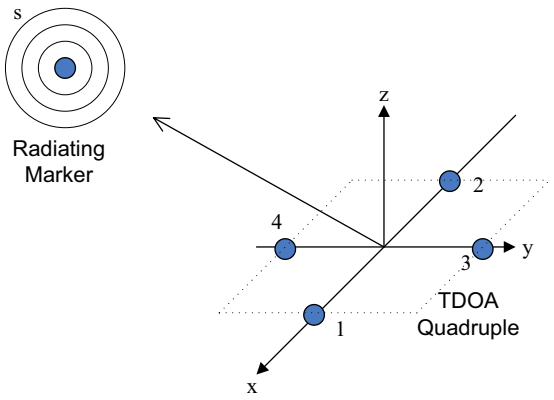

Figure 5.2: TDOA quadruple array.

can be defined as β which is the angle formed with the y-axis. The remaining direction angle γ associated with the z-axis can be found using the identity

$$\cos^2\alpha + \cos^2\beta + \cos^2\gamma = 1. \tag{5.17}$$

In Brandstein et al. [13] and in this thesis it is assumed that the angle formed with the $+z$-axis is always in the range $0 \leq \gamma \leq \pi/2$. The reason for this limitation is that it is assumed that the source is always received on the $+z$ side of the coordinate frame which is an appropriate assumption for the configuration investigated in Section 5.2.

The bearing line can now be defined in the local coordinate system via a parametric line equation passing through the origin and having a direction defined by the direction cosines $\bar{\boldsymbol{q}}' = \begin{bmatrix}\cos\alpha & \cos\beta & \cos\gamma\end{bmatrix}^T$ as

$$\bar{\boldsymbol{\ell}}' = r\bar{\boldsymbol{q}}' \tag{5.18}$$

where r is the parameter that defines the distance from the origin and the prime symbol ($'$) indicates the local coordinate frame. The parametric line equation can be converted into the global frame using a standard transformation

$$\bar{\boldsymbol{\ell}} = r\boldsymbol{R}\bar{\boldsymbol{q}}' + \bar{\boldsymbol{p}} \tag{5.19}$$

where $\boldsymbol{R}$ is the rotation matrix and $\bar{\boldsymbol{p}}$ is the location of the sensor midpoints in the global reference frame.

If two or more sensor quadruples are implemented at independent locations then the intersection or near intersection of these lines can be used to find the source location. For example, given two bearing lines, a and b, defined completely in the global coordinate system[1] by

$$\bar{\boldsymbol{\ell}}_a = r_a \bar{\boldsymbol{q}}_a + \bar{\boldsymbol{p}}_a \tag{5.20}$$

$$\bar{\boldsymbol{\ell}}_b = r_b \bar{\boldsymbol{q}}_b + \bar{\boldsymbol{p}}_b \tag{5.21}$$

then the shortest distance between the two lines [52] is given by

$$d_{ab} = |\,(\bar{\boldsymbol{p}}_a - \bar{\boldsymbol{p}}_b) \cdot \hat{\boldsymbol{n}}| \tag{5.22}$$

where $\hat{\boldsymbol{n}} = \bar{\boldsymbol{q}}_a \times \bar{\boldsymbol{q}}_b / |\bar{\boldsymbol{q}}_a \times \bar{\boldsymbol{q}}_b|$ [52].

The position of the source marker found at the midpoint of the two positions on the each line where the shortest distance between the two lines occurs. The positions on lines a and b are denoted by

$$\bar{\boldsymbol{\ell}}_a = {}_s\bar{\boldsymbol{p}}_{ab} \tag{5.23}$$

$$\bar{\boldsymbol{\ell}}_b = {}_s\bar{\boldsymbol{p}}_{ba} \tag{5.24}$$

where the subscript s denotes the source location. The two positions on each line are related by the vector that marks the shortest distance between the two lines.

$${}_s\bar{\boldsymbol{p}}_{ba} = {}_s\bar{\boldsymbol{p}}_{ab} + d_{ab}\,(\bar{\boldsymbol{q}}_a \times \bar{\boldsymbol{q}}_b) \tag{5.25}$$

This results in an over-constrained set of equations for the parameters r_a and r_b that can be solved for using a least squares algorithm such as the one presented in section A.4.

$$r_a \bar{\boldsymbol{q}}_a - r_b \bar{\boldsymbol{q}}_b = \bar{\boldsymbol{p}}_b - \bar{\boldsymbol{p}}_a - d_{ab}\,(\bar{\boldsymbol{q}}_a \times \bar{\boldsymbol{q}}_b) \tag{5.26}$$

The position of the source marker is then found by substituting r_a and r_b in equations 5.20 and 5.21 and finding the midpoint.

[1] This means that $\bar{\boldsymbol{q}} = \boldsymbol{R}\bar{\boldsymbol{q}}'$.

	RMS	Mean	Std. Dev.	Max	Min
x	0.0003	0.0000	0.0003	0.0007	-0.0007
y	0.0011	-0.0010	0.0004	-0.0003	-0.0020
z	0.0002	0.0000	0.0002	0.0004	-0.0004
3D	0.0011	0.0011	0.0004	0.0020	0.0006

Table 5.2: Sample statistics for the intersection of headings method. All statistics in meters. The statistics can be interpreted in the same manner as is discussed in Table 5.1. The triangulation error is present in the y-axis is the dominating error in the algorithm.

$$\bar{\boldsymbol{p}}_{src} = \tfrac{1}{2}\left(\bar{\boldsymbol{\ell}}_a|_{r_a} + \bar{\boldsymbol{\ell}}_{\boldsymbol{b}}|_{r_b}\right) \tag{5.27}$$

The method was tested using the same source positions given in Section 5.1.1. Two sensor quadruples were used with their midpoints located at $\bar{\boldsymbol{p}}_a = \begin{bmatrix}-0.15 & 0.00 & 0.00\end{bmatrix}^T$ and $\bar{\boldsymbol{p}}_a = \begin{bmatrix}0.15 & 0.00 & 0.00\end{bmatrix}^T$ and the quadruples were rotated 90° about the x axis so that the local $+z$ axis is aligned in the $-y$ direction of the global coordinate frame. The sensors in each quadruple were placed at the following locations in the local coordinate frame for both sensor groupings.

$$\begin{aligned}
\bar{\boldsymbol{p}}_1 &= \begin{bmatrix}0.05 & 0.00 & 0.00\end{bmatrix}^T \\
\bar{\boldsymbol{p}}_2 &= \begin{bmatrix}-0.05 & 0.00 & 0.00\end{bmatrix}^T \\
\bar{\boldsymbol{p}}_3 &= \begin{bmatrix}0.00 & 0.05 & 0.00\end{bmatrix}^T \\
\bar{\boldsymbol{p}}_4 &= \begin{bmatrix}0.00 & -0.05 & 0.00\end{bmatrix}^T.
\end{aligned} \tag{5.28}$$

The results for the 27 locations using exactly determined time differences is shown in Table D.2 in Appendix D while the summary statistics are provide in Table 5.2. An example plot showing the source located at $\bar{\boldsymbol{p}}_{src} = \begin{bmatrix}-0.50 & -1.00 & -0.50\end{bmatrix}^T$ with the sensors and bearing lines is given in Figure 5.3. The overall root mean square distance error was found to be $RMS_{3D} = 0.001$m. This is clearly a far superior result to the method presented in Section 5.1.1. As expected, the main contribution of error is found along the y-axis which is the viewing axis for this particular configuration.

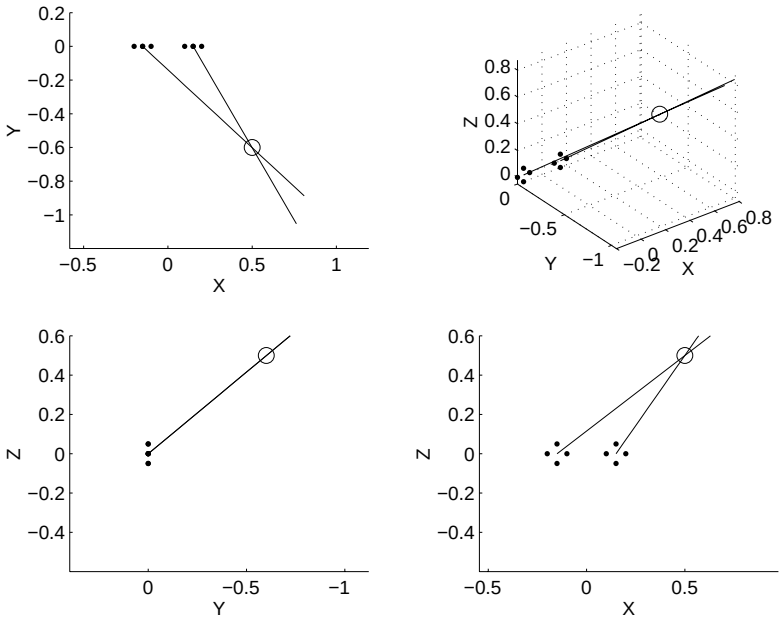

Figure 5.3: Computed bearing lines for an example source. The sensors are marked with a solid dot (•) while the source location (0.50,-0.6,0.50) is marked with an open circle (○). The bearing lines are shown leaving the center of the sensor quadruple and passing through the simulated marker position.

This method provides a reliable starting point in developing a position determination algorithm using the signals simulated using the framework in Chapter 3 that was verified in Chapter 4. However, before attempting to use this algorithm with the signals derived from the finite element model, the topic of determining the time difference of arrival between two signals needs to be discussed first. That topic is presented in the next section.

5.1.3 Computing the Time Difference of Arrival

In order to compute the time difference of arrival between two signals, the cross-correlation function will be used. Other methods such as the phase-lock loop [24, 65] can be tested in the future, but the cross-correlation method will suffice for the research presented in this thesis.

The cross-correlation method is based on the convolution between two signals [46, 66]. For real continuous time signals, the cross-correlation of one signal $s_i(t)$ with a second signal $s_j(t)$ is given by

$$\phi_{ij}(t) = s_i(t) \star s_j(t) \tag{5.29}$$

$$= s_i(-t) * s_j(t) \tag{5.30}$$

$$= \int_{-\infty}^{\infty} s_i(-\tau) s_j(t-\tau) d\tau \tag{5.31}$$

where $\star$ is the cross-correlation operator and $*$ is the convolution operator. The location of the peak value of the cross-correlation function corresponds to the time delay τ between the two signals[2]. The time delay can be negative or positive if the signal $s_i(t)$ leads or lags respectively.

In discrete time signals, the convolution integral becomes a sum and is given by

[2]It is important to note that peak detection of a signal is not trivial once presented with real data. This issue will need to be investigated thoroughly once this work moves from the simulation domain to a real prototype domain.

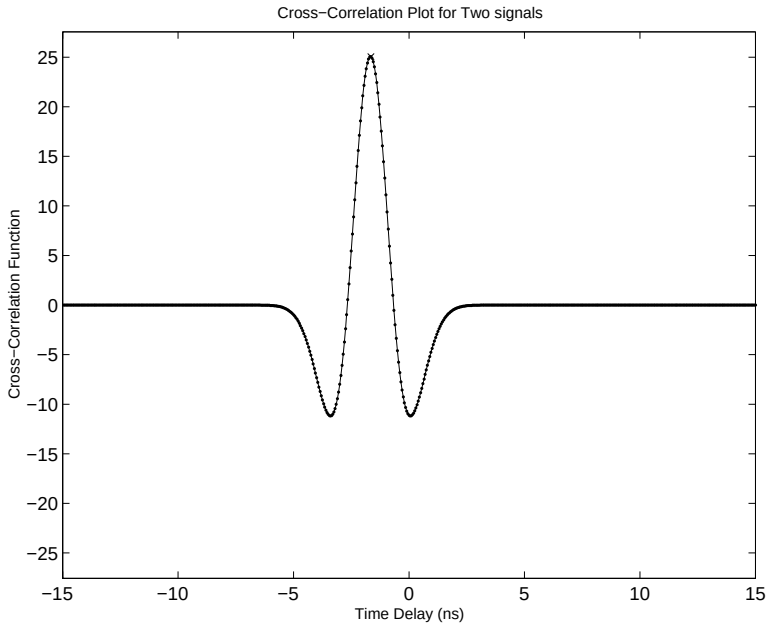

Figure 5.4: Sample Plot of the Cross-Correlation Function for Two Signals. $\Delta t = 0.05$ns.

$$\phi_{12}(n) = s_1(n) \star s_2(n) \tag{5.32}$$

$$= s_1(-n) * s_2(n) \tag{5.33}$$

$$= \sum_{k=-\infty}^{\infty} s_1(-n) s_2(n-k) \tag{5.34}$$

where n is the time step. Clearly, in realistic situations, the discrete signals are only available for a bounded set of time steps. For example, in this thesis the signals are collected over the time period $0 \leq t \leq 15$ns. The signals are sampled at every 0.05ns which results in a signal at sensor i defined by $s_i(n)$ for $n = 0 \ldots N$ where $N = 300$ and $t_n = n\Delta t$. The cross-correlation function can be redefined to be

$$\phi_{12}(n) = \sum_{k=-N}^{N} s_1(-n) s_2(n-k). \tag{5.35}$$

The cross-correlation function is computed using the `xcorr` function provided by MATLAB. The `xcorr` function uses the same formula in equation 5.35 to compute the cross-

	RMS	Mean	Std. Dev.	Max	Min
x	0.1158	-0.0000	0.1180	0.2647	-0.2647
y	0.2304	-0.0323	0.2325	0.3103	-0.4209
z	0.1180	-0.0000	0.1202	0.2402	-0.2402
3D	0.2836	0.2423	0.1503	0.4972	0.0106

Table 5.3: Sample statistics for the intersection of headings method using Cross-Correlation. All statistics in meters.

correlation function. A sample plot of the cross-correlation function for the two Neumann pulses shown in Figure 3.6 is given in Figure 5.4. The maximum point of the cross-correlation plot, i.e., time difference of arrival for the two signals, occurs at $\tau_{ij} = -1.6500$ns but the real time difference of arrival is calculated to be $\tau_{ij} = -1.6678$ns. Clearly an inherent error is now introduced into the time difference of arrival algorithm by the significant difference in the actual time difference of arrival and the measured time difference.

A similar set of tests to the ones presented in Sections 5.1.1 and 5.1.2 was performed using the maximum value of the cross-correlation function to determine the time difference. The intersection of headings method was used and the signals at the array locations were generated using equation 3.55. The summary statistics for the 27 source locations are presented in Table 5.3 and the detailed measured positions and error values are provided in Table D.3 in Appendix D.

Clearly, the performance is very poor using this method for determining the time difference of arrival. The actual time difference of arrival is between two of the time delay steps computed using the cross-correlation function. Specifically for the example in Figure 5.4 the function maximum if it were a continuous function occurs at a point between the discrete time delay value at -1.65ns and -1.70ns since these are two time steps present on either side of the actual value.

There are two options to improve the time difference of arrival computation. First, the time step could be reduced to a level where the granularity of the signal would match that of the capabilities of the algorithm. This is very impractical as it would significantly increase the amount of data required to compute the time difference of arrival. The second method would be to compute the peak of the correlation function using a weighted average method using a window of data that surrounds the maximum value of the signal. Figure

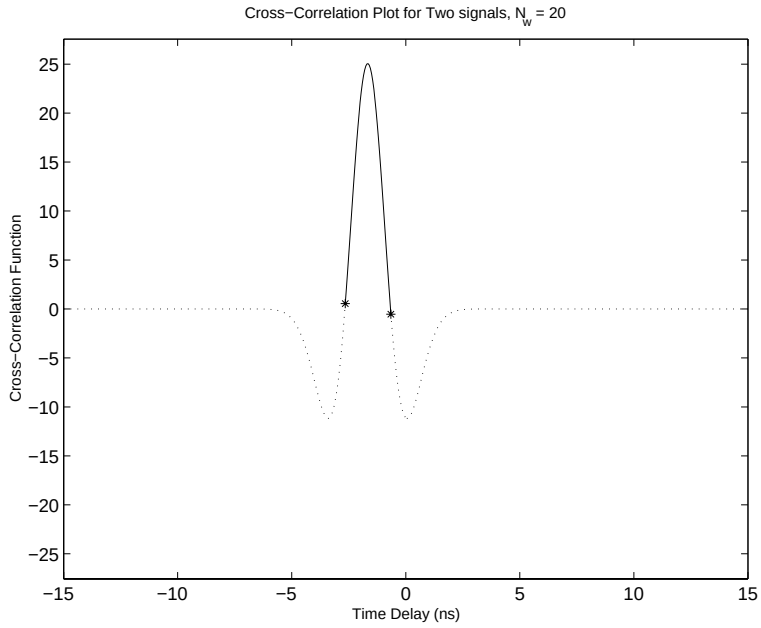

Figure 5.5: Example of Data Used in Weighted Average for Cross-Correlation Peak. $\Delta t = 0.05$ns.

5.5 shows the same cross-correlation plot as the one found in Figure 5.4. The points in the function marked with a solid line are used in the weighted average. In this example the window is of size $N_w = 20$ where the window includes N_w points on the left of the maximum, N_w points on the right of the maximum and the maximum point itself. This results in $2N_w + 1$ points used in the weighted average. The weighted average is computed using the formula in Equation 5.36.

$$\tau_{ij} = \frac{\sum_{n=n_{max}-N_w}^{n_{max}+N_w} \phi_{ij}(n)\Delta tn}{\sum_{n=n_{max}-N_w}^{n_{max}+N_w} \phi_{ij}(n)} \tag{5.36}$$

where n_{max} is the time delay corresponding with the maximum value of the correlation function.

This method has proven to be quite successful in improving the measurement accuracy as the test for the same 27 locations is repeated using the weighted average. Clearly the results are improved dramatically as the RMS values have fallen from 0.284m RMS to 0.015m RMS. The summary statistics are provided in Table 5.4 and the detailed measured and error values are provided in Table D.4 in Appendix D. Although these results do not

	RMS	Mean	Std. Dev.	Max	Min
x	0.0067	-0.0000	0.0068	0.0094	-0.0094
y	0.0122	-0.0001	0.0124	0.0136	-0.0228
z	0.0065	0.0000	0.0067	0.0102	-0.0102
3D	0.0154	0.0140	0.0065	0.0247	0.0018

Table 5.4: Sample statistics for the intersection of headings method using weighted cross-correlation. All statistics in meters.

match the desired level of accuracies needed by the applications discussed in Chapter 1, this method does provide a starting point for investigating algorithms that can be used in the position determination of radiating source. Further, the effect of reflecting and attenuating objects can be studied sufficiently with this level of accuracy.

Now that an accurate method of determining the time difference of arrival has been found, two different parameters should be investigated in order to determine their optimal values. These parameters are the sampling time step size and the size of the weighting window used in the weighted average. Figure 5.6 shows the results for three different time step sizes and several window sizes. The data plotted are the RMS values for the distance error using the same 27 locations presented previously with only the time step and window size changed.

It is clear that reducing the size of the time step can improve the level of accuracy for the algorithm. However, each curve has a minimum value that corresponds to the situation where most of the middle "hump" of the curve is used as is the case in Figure 5.5. The missing values for large windows for the smaller time steps are due to the fact that the computed time differences result in complex position vectors which are not valid. The minimum value for the smallest time step curve ($\Delta t = 0.01$ns) approaches the theoretical value given for the 3D RMS value in Table 5.2. The optimal window size occurs at $N_w = 10, 20, 100$ for the 0.1ns, 0.05ns and 0.01ns time steps respectively. However, these window sizes are likely only valid for the Neumann pulse signal described in this thesis using only the parameters defined in Table 4.1. Therefore, in the future a robust algorithm for determining the appropriate window size should be developed so that the entire middle "hump" is extracted for the weighted average.

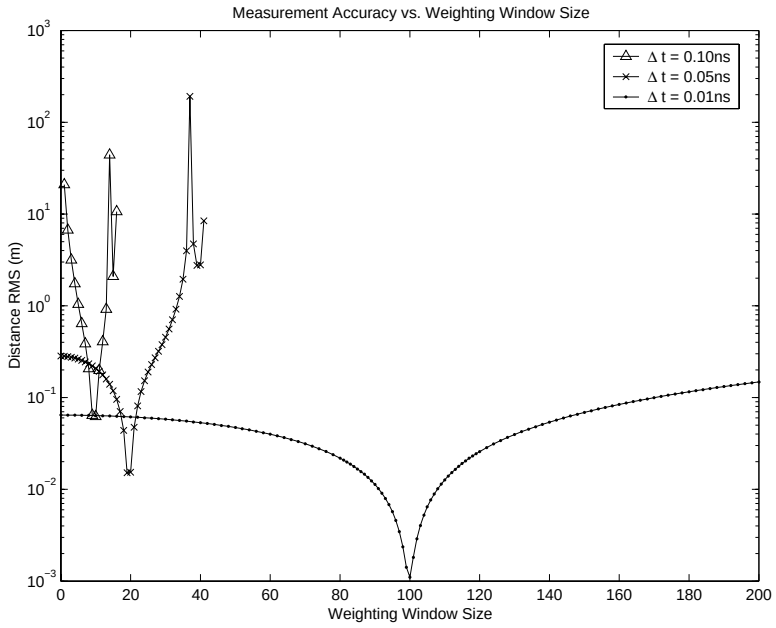

Figure 5.6: Performance of different sized windows used to determine weighted average cross-correlation peak.

5.2 Integration of Finite Element Simulator and Time Difference of Arrival Algorithm

In Section 5.1.2 the time difference of arrival method was demonstrated for the intersection of headings method using precisely computed time differences. Section 5.1.3 then described the performance of the intersection of headings method using time differences derived from numerical approximations of the analytical signals in free space. In this section, the performance of the intersection of headings algorithm is presented using signals generated from the finite element simulator presented in Chapter 3.

As was done in previous sections, the method was tested for 27 source locations. The finite element simulator was run 27 times for a completely free space arrangement. The signals were sampled at the same locations provided in Section 5.1.2 and were extracted using the isotropic antenna model provided in equation 3.64. The signals were sampled at $\Delta t = 0.05$ns and the cross-correlation weighting window was set to $N_w = 20$. The summary statistics are presented in 5.5 and the detailed measurement errors are presented

	RMS	Mean	Std. Dev.	Max	Min
x	0.2702	0.0192	0.2746	0.3876	-0.3885
y	0.3957	0.3086	0.2525	0.6332	-0.4300
z	0.2522	-0.0000	0.2570	0.3731	-0.4239
3D	0.5415	0.5123	0.1785	0.8212	0.1700

Table 5.5: Summary statistics for the intersection of headings method using signals for FEM simulator. All statistics in meters.

in Table D.5 of Appendix D.

Clearly, the performance of the combined finite element simulator and intersection of headings is very poor and does not fit in with the expected accuracy levels for the applications discussed in Chapter 1. Upon detailed examination it was discovered that the simulated signals have a definite phase error in them that is not common to all of the sensors in a given quadruple. Figure 5.7 shows an exploded view of the signals obtained from the finite element simulator and the reference signals that are expected based on the analytical definition. Similar results were found for the second quadruple and the exploded signal views are provided in Figure D.3 in Appendix D for completeness.

The reference signals show a much tighter grouping with very little difference in the phases. In fact, the phase differences for the pair S_{12} in the quadruple should be close to 0.05ns and the second pair S_{34} should have zero time difference. However, the actual differences are found to be 0.14ns and 0.04ns respectively. With the current configuration where the sensor pairs are separated by 0.1m the time difference error of 0.1ns results in the following angular error.

$$\theta_{err} = \cos^{-1}\left(\frac{(0.1\text{ns})\, c_0}{0.1\text{m}}\right) \tag{5.37}$$

$$= 72.6^\circ \tag{5.38}$$

At 1.0m from the sensors, the time difference error relates to a distance error of approximately $d_{err} = 1.0\text{m}\tan(\theta_{err}) = 3.18\text{m}$.

If sub-centimeter accuracy was set as the goal for up to 1.0m from the sensor, then the maximum acceptable angular error is

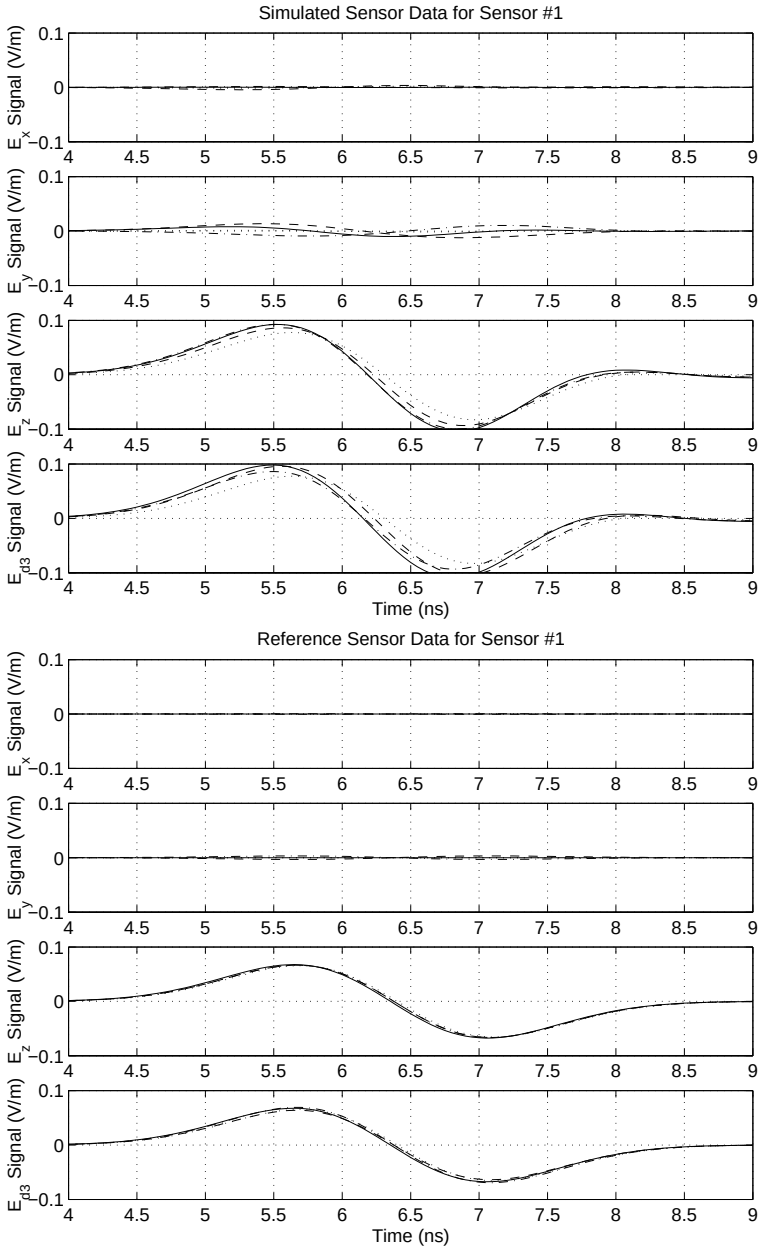

Figure 5.7: Sample of signals using FEM and analytical for a TDOA quadruple 1 for Source Location 5, (0.00, -1.00, 0.00), in exploded view. Full signals are shown in Figure D.1. The collection of plots show the signals generated by the FEM simulator and their associated reference signal. E_x, E_y and E_z are infinitesimal dipole signals aligned with the associated axis using the model in equation 3.63. E_{d3} is the signal using the isotropic receiving antenna model in equation 3.64. The signals are identified as: Sensor 1 - solid line, Sensor 2 - dotted line, Sensor 3 - dash-dot line and Sensor 4 - dashed line.

$$\theta_{err}^{max} = \tan^{-1}\left(\frac{0.01\text{m}}{1.0\text{m}}\right) \tag{5.39}$$

$$= 0.57^{\circ}, \tag{5.40}$$

and at 2.0m from the sensor,

$$\theta_{err}^{max} = \tan^{-1}\left(\frac{0.01\text{m}}{2.0\text{m}}\right) \tag{5.41}$$

$$= 0.29^{\circ}. \tag{5.42}$$

Each of these angular errors result in a maximum time differences of the sensor pairs separated by 0.1m to be[3]

$$\tau_{err}^{max} = \frac{0.01\text{m}\cos\left(0.57^{\circ}\right)}{c_0} \tag{5.43}$$

$$= 0.033\text{ns}. \tag{5.44}$$

The Neumann pulse that was used for the simulations has a maximum frequency of approximately 1.5GHz which results in a signal period of $T = 1/f = 0.66$ns. Therefore, the maximum phase error that could be endured for *sub-centimeter* accuracy is

$$\delta_{err}^{max} = \frac{0.033\text{ns}}{0.66\text{ns}}360^{\circ} \tag{5.45}$$

$$= 18^{\circ}. \tag{5.46}$$

For *sub-millimeter* accuracy the maximum time difference error becomes $\tau_{err}^{max} = 0.0033$ns and the maximum phase error is $\delta_{err}^{max} = 1.8^{\circ}$.

The physical dimensions of the sensor quadruples could be changed so that the baseline distance between the sensor pairs is increased and there is a better angular measurement provided. However, there is no guarantee that the time difference of arrival errors would not

[3]The maximum error in the time differences for maximum error of 0.01m at 1.0m from the sensor and 2.0m from the sensors only differ by small amounts at the picosecond level hence resulting in a maximum τ of 0.033ns.

increase from additional phase error that could occur with the sensors located at different locations. Therefore, it is important to investigate the source of the phase error introduced into the system.

In Section 3.2.2, the vector element was introduced to help correct the error of spurious solutions and provide a simpler and more accurate technique to apply the boundary conditions. However, the vector elements can introduce a phase error [33, 36]. The two main factors that are involved in determining the size of the phase error are (i) order of the vector element and (ii) density of unknowns (i.e., element size). In these simulations, a zeroth order vector element is used[4] and the maximum vector size is set to $\lambda_{min}/3$ where λ_{min} is related to the maximum frequency of the Neumann pulse which was previously defined as being approximately 1.5GHz corresponding to $\lambda_{min} \approx 0.2$m.

For an unstructured mesh[5] using tetrahedral vector elements the resulting phase cannot be defined by an analytical expression but can be determined numerically [44]. In Jiao et al. [33] the relationship of phase error relative to the density of unknowns is provided graphically. The density of unknowns is a value given in *unknowns per cube wavelength* or mathematically as u/λ_u^3 where u is the number of unknowns. This peculiar expression is essentially a normalization of the density relative to the minimum wavelength λ_{min}. For example, in the simulations presented in Chapter 4 and in this section the volume is 0.5m by 1.0m by 0.5m resulting in a volume that is 0.25m^3. However, the dimensions can be rewritten to be a function of wavelength, i.e., the length in the x dimension for a minimum wavelength of $\lambda_{min} = 0.2$m is $0.5\text{m}/(0.2\text{m}/\lambda_u) = 2.5\lambda_u$ where λ_u is considered a unit of wavelength. Returning to the examples used in this section, the volume of interest now has dimensions of $2.5\lambda_u$ by $5\lambda_u$ by $2.5\lambda_u$ resulting in a volume of $31.25\lambda_u^3$. However, the additional volume of the input region and surrounding apron shown in Figure 4.1 needs to be taken into account so that the actual simulated volume is 0.7m by 1.4m by 0.7m or in wavelength units is $3.5\lambda_u$ by $7\lambda_u$ by $3.5\lambda_u$ giving a total volume of $85.75\lambda_u^3$. In these simulations, the number of degrees of freedom (dof), i.e., unknowns, was approximately 120,000. However, these include all the degrees of freedom for both the electric field and vector potential. Therefore, if only the degrees of freedom for the electric field are considered then the density of unknowns can be approximated to be $\rho_u \approx 60,000u/85.75\lambda_u^3 = 700u/\lambda_u^3$.

Returning to the graphical relationship provide by Jiao et al. the mean phase error

[4]FEMLAB 3.1 is limited to zeroth order vector elements.

[5]An unstructured mesh has nodes that are not uniformly distributed.

for the zeroth order elements with unknown density $1170u/\lambda_u^3$ is approximately $30-40°$. The same density with the first order elements has a mean phase error of $10-15°$ and the second order elements are in the $2-3°$ range. If the element size is changed so that it is a maximum of $\lambda_{min}/5$ then the mean phase error for the zeroth order mean phase error is reduced to $20-30°$ (electrical field dof = 250,000; $\rho_u \approx 2900u/\lambda_u^3$). Further, if the element size is even further reduced to $\lambda_{min}/10$ then the zeroth order mean phase error is reduced $8-12°$ (electrical field dof = 2,200,000; $\rho_u \approx 25,700u/\lambda_u^3$) however the number of degrees of freedom causes the linear system of equations to be larger than can be handled by FEMLAB on an above average desktop computer[6].

This caveat causes the research to come to a set of cross-roads. There are three main options that can be pursued. First, the next release of FEMLAB can be evaluated to see to if it gains the ability to generate models using higher-order vector elements. The second option is that time based position localization algorithms can be ignored and only spatially based systems will be investigated. However, this seems illogical as both types of systems should be compared or possibly hybridized in order to generate an effective solution. Finally, a custom set of finite element code could be generated that handles higher order elements. Further, the wave equation formulation could also be implemented so that the methods themselves can be compared. The first or third options seem the most plausible but all three options are beyond the topics that are presented in thesis.

5.3 Summary

In this chapter, two methods of determining the position of a marker using the time difference of arrival for a radiating signal was described. It was found that the linearized approximation method was very inaccurate and not suitable for the applications discussed in Chapter 1. However, the intersection of headings method provides a moderately accurate method. Tests here showed that precise time difference of arrival methods result in an RMS position error of approximately 1mm for a set of 27 prescribed location. The position error was worsened when the cross-correlation method was used to determine the time difference of arrival. However, a weighted average was introduced which improved the

[6]A machine with a Pentium 4 2.8GHz processor and 2GB of RAM with Linux Red Fedora Core 2 was used for these simulations.

error significantly. The section concluded with a description of the effect the size of the time step and the size of the averaging window has on the accuracy of the time difference of arrival method for precisely computed signals. Finally, the time difference of arrival method was tested using signals generated by the finite element simulator. However, the phase error introduced by zeroth order vector element proved to be too large for any type of effective position measurement system simulation to be valid. It is expected that higher order elements would improve the simulation significantly so that the framework would become useful.

Chapter 6

Conclusions and Future Work

This thesis set out to create a model framework that could be implemented to investigate the theoretical performance of a spatial measurement system using radio frequency based technology. The ultimate goal was to create a tool that would allow a metrology researcher the ability to design a new spatial measurement system that could be used in biomechanics, computer-assisted surgery or industrial measurement. This final chapter summarizes the conclusions and lists the future work that exists for this line of research.

6.1 Summary of Conclusions

There were four main areas from which conclusions are drawn for this thesis. These four areas include (i) the design of the wave propagation simulation, (ii) the performance of the wave propagation simulation, (iii) the quality of the localization algorithms using time difference of arrival and (iv) the integration of the wave propagation simulation and time difference of arrival algorithms.

6.1.1 Design of the Wave Propagation Simulation

The proposed model was provided in Chapter 3. A key item for success in developing the model was in the formulation of the governing equations. FEMLAB was not capable of solving a time domain electromagnetic wave propagation problem using the wave equation formulation because it does not contain the associated time stepping algorithms required

to solve the model. The alternative formulation used the magnetic vector potential which when formulated using the weak form is limited to having only first order temporal and spatial derivatives that can be solved using the FEMLAB software.

Another key decision in the design was with respect to the type of finite element used to generate the finite element equations. The vector finite element was chosen to avoid the spurious errors that can occur in finite element simulations of electromagnetic waves. However, it was shown in section 5.2 that the zeroth order vector elements, the only order of vector elements available in FEMLAB, introduced phase errors to the propagating wave. These phase errors can be reduced by (i) reducing the maximum size of the vector elements (i.e., increasing the density of finite elements) or (ii) increasing the order of the vector element to second or third order. However, with both methods the number of degrees of freedom will increase resulting in a larger system of equations that would be required to be solved.

Finally, one last observation about the design is in reference to the source transmitter model and sensor receiver model. Neither model represents any available physical antenna but they do provide an appropriate approximation of real antennas for study. However, if in future work researchers want to compare the simulations to a prototype then the antenna transmission and reception models will require some detailed study in order to improve the realism of the simulation.

6.1.2 Performance of the Wave Propagation Simulation

The finite element method was tested for several free space cases in Chapter 4. Two major observations were made in this chapter. First, the signals were attenuated as a function of distance from the source location. Although it was expected that the line and point sources should be attenuated they had additional levels of attenuation in their extracted signals. This was found to be attributed to the absorbing boundary conditions as the boundary conditions could be removed (i.e., not applied) and the signals propagated through the volume properly only to be reflected at the truncation boundaries. The second major observation had to do with the phase of the signals. It was quite obvious that the phase of the simulated signals did not match those of the reference signals. It was first expected that the phase error would be a localized error and would only affect the position determination algorithms slightly, however this proved to be incorrect as tests in Chapter 5 showed that

the phase errors had a significant effect.

6.1.3 Quality of the Localization Algorithms using Time Difference of Arrival

The time difference of arrival algorithms for two different methods was presented. The intersection of headings method was found to be more accurate within the framework that was tested. However, the intersection of headings method requires significantly more sensors (minimum of 8 sensors) than the linearized approximation method (minimum of 4 sensors). This leads to the conclusion that the linearized approximation method is still useful in applications such as triangulating the location of a cellular phone. The location of a cellular phone can be found using the time difference of arrival of the signals arriving at a set of cellular phone transmission towers. The linearized approximation method becomes useful since the towers are not easily grouped into the sensor quadruple arrangement required by the intersection of headings method. However, for the applications originally presented in Chapter 1 and the concept introduced in Chapter 3 (Figure 3.1), the intersection of headings method is more appropriate than the less accurate linearized approximation method.

Prior to pushing forward with the algorithm as presented in section 5.1 it should be further investigated because the algorithm was implemented using perfect input data and was only accurate to 1mm. Hence, some attention should be paid in the future to improving the algorithm so that it can perform at an accuracy better than 1mm within the test volume that was investigated in Chapter 5.

Lastly, the method of using the cross-correlation function to determine time delay between to signals needs to be enhanced using a weighted average technique. It was shown that the time delay value typically needs to be resolved down to a level that is less than discrete time delays found using the `xcorr` function provided by MATLAB. The weighted average improved the accuracy of the time delay computation but further investigation into the size of the weighted average window will be required as different signal types (i.e., Gaussian pulse or sinusoid) will have different cross-correlation function shapes.

6.1.4 Integration of the Wave Propagation Simulation and Time Difference of Arrival Algorithms

The final set of observations made in this thesis was in regards to the integration of the finite element simulator and the intersection of headings algorithm. Signals from the finite element simulator for a free space domain were extracted and input into the intersection of headings algorithm. The accuracy of the simulation was found to be very poor with the RMS statistic approaching 0.5m which was significantly higher than the centimeter or millimeter accuracy required for the applications presented in Chapter 1 such as biomechanics or image-guided surgery. It was determined that the most significant source of error was the phase error introduced by the zeroth order vector finite elements. The phase error can be as high as 30 - 40° using the geometry presented in Chapter 4. It was reported that for sub-centimeter and sub-millimeter accuracy that the maximum allowable phase error was 18° and 1.8° respectively which is clearly not met by the phase errors introduced by the zeroth order vector finite elements and the associated density. However, if FEMLAB was to introduce a vector element of order two then the phase error can be reduced to 2 - 3°, hence allowing studies of system design with sub-centimeter accuracy. Further accuracy can be obtained by decreasing the maximum allowable size of the element up to the computational limits of the desktop computer being used for the simulation.

6.2 Future Work

The modelling framework was found to contain a significant source of error in the phase of the wave propagating through the volume, however, the framework would become very useful should the following improvements be made.

1. Introduce higher order vector finite elements by upgrading to the latest version of FEMLAB, should they include the enhancement, or by developing a custom collection of finite element code. An alternative method would be to research a new finite element that would eliminate or reduce the amount of phase error that is introduced by the current vector finite elements. This alternative solution would likely also involve the creation of a custom collection of finite element code.

2. Implement alternate volume truncation methods such as the PML in order to re-

duce the amount of unwanted attenuation in the signal that propagates through the volume.

Should the above two improvements become available, get implemented and found to work, other improvements to the framework that could also be beneficial include (i) investigating the methods of solving the linear sets of equations, (ii) investigating the precision of the intersection of headings algorithm, and (iii) investigating the time difference of arrival algorithm with cross-correlation or other methods including the phase lock loop. It would be useful if the methods used to solve the finite element equations were improved so that they are solved faster and used less memory. However, these improvements are very much dependent on the properties of the matrices generated from the linear system of equations. It would also be useful to investigate why the intersection of headings method is only accurate to 1mm with perfect input data. It would be important to understand whether it is simply a numerical precision error or if there is a limitation in the algorithm that is not immediately recognizable. Also, the method of finding the time difference of arrival between two signals should also be investigated. It is expected that the methods presented here may have some difficulties when more realistic signals with noise and systematic errors are introduced into the model.

Finally, one concept that has not been explored in this thesis is how well the models developed in Chapter 3 represent reality. Maxwell's equations have been used extensively since their inception, but their ability to model reality in each application needs to be challenged every time. This can be investigated using a prototype where the model is extended to account for noise and errors that accompany any real world implementation.

6.3 Closing Remarks

In closing, items 1 and 2 and the short list of other suggested improvements shown in the previous section should allow this modelling framework to be useful for accurately simulating the time domain wave propagation of an electromagnetic field using the finite element method. If these suggestions are found to be successful, then the opportunity to investigate the concept first introduced at the beginning of this thesis in Figure 1.1 would become reality. In fact, there are many other configurations and experiments that could be completed in the virtual prototype domain that could lead to a successful implementation of

a radio frequency spatial measurement system for use in medicine, research and industrial applications.

Appendix A

Selected Mathematical Concepts

In this appendix a selection of mathematical concepts are presented for the convenience of the reader. The concepts presented are by no means complete and the reader is directed to associated references for details.

A.1 Tensors

Occasionally, throughout this thesis there are references to tensors and tensor transformations. Although explaining this concept is well beyond the scope of this thesis a few concepts are defined here. A more detailed explanation can be found in Danielson [23].

A.1.1 Order of a Tensor

In general a tensor is a linear function that transforms a given scalar, vector, matrix or higher order number object into a similar or different form [23]. For tensors of zeroth to second order, the transformations closely resemble those of vector and matrix operations. For example, a zeroth order tensor is simply a scalar. The scalar variable can be multiplied (dotted) into any other tensor to produced a scaled version of the original tensor. On the other hand, a first order tensor is a linear function that transforms a vector into a scalar. For example, consider the vectors $\bar{\boldsymbol{a}}$ and $\bar{\boldsymbol{b}}$ the dot product of the two vectors generates a scalar ψ

$$\psi = \bar{\boldsymbol{a}} \cdot \bar{\boldsymbol{b}}. \tag{A.1}$$

Therefore, any vector $\bar{\boldsymbol{a}}$ is a tensor of order one if it is understood that it is to be dotted into another vector [23].

Similarly, matrices are tensors of order two as they are linear transformations that map a vector into another vector. For example, a rotation matrix $\boldsymbol{A}$ will rotate a vector from one reference frame to another.

$$\boldsymbol{A} \cdot \bar{\boldsymbol{a}} = \bar{\boldsymbol{b}} \tag{A.2}$$

Higher order tensors can also be defined.

A.1.2 Properties of a Tensor

Again, the properties of tensors resemble those of matrix and vector algebra. Transposes and inverses are defined for tensors. Tensors can be symmetric, antisymmetric (skew) and orthogonal. Eigenvalues and eigenvectors can also be found for tensors. For second order tensors these operations and properties resemble matrix operations and properties but they can be generalized for higher order tensors.

A.2 Matrix-Vector Algebra

The matrix-vector algebra used in this thesis is well documented in the literature with Riley et al. [52] used as the main reference. However, for easy reference a selection of algebraic vector identities are shown here as listed in Riley, Balanis [5] and Jin [36].

$$\bar{\boldsymbol{a}} \cdot \bar{\boldsymbol{b}} \times \bar{\boldsymbol{c}} = \bar{\boldsymbol{b}} \cdot \bar{\boldsymbol{c}} \times \bar{\boldsymbol{a}} = \bar{\boldsymbol{c}} \cdot \bar{\boldsymbol{a}} \times \bar{\boldsymbol{b}} \tag{A.3}$$

$$\bar{\boldsymbol{a}} \times \left(\bar{\boldsymbol{b}} \times \bar{\boldsymbol{c}}\right) = \left(\bar{\boldsymbol{a}} \cdot \bar{\boldsymbol{c}}\right) \bar{\boldsymbol{b}} - \left(\bar{\boldsymbol{a}} \cdot \bar{\boldsymbol{b}}\right) \bar{\boldsymbol{c}} \tag{A.4}$$

$$\begin{aligned} \left(\bar{\boldsymbol{a}} \times \bar{\boldsymbol{b}}\right) \cdot \left(\bar{\boldsymbol{c}} \times \bar{\boldsymbol{d}}\right) &= \bar{\boldsymbol{a}} \cdot \bar{\boldsymbol{b}} \times \bar{\boldsymbol{c}} \times \bar{\boldsymbol{d}} \\ &= \bar{\boldsymbol{a}} \cdot \left(\bar{\boldsymbol{b}} \cdot \bar{\boldsymbol{d}} \bar{\boldsymbol{c}} - \bar{\boldsymbol{b}} \cdot \bar{\boldsymbol{c}} \bar{\boldsymbol{d}}\right) \\ &= \left(\bar{\boldsymbol{a}} \cdot \bar{\boldsymbol{c}}\right) \left(\bar{\boldsymbol{b}} \cdot \bar{\boldsymbol{d}}\right) - \left(\bar{\boldsymbol{a}} \cdot \bar{\boldsymbol{d}}\right) \left(\bar{\boldsymbol{b}} \cdot \bar{\boldsymbol{c}}\right) \end{aligned} \tag{A.5}$$

A.3 Vector Calculus

A summary of the four vector calculus operators is provided. This work is a summary of material collected from the works of Bina [11], Balanis [5], Danielson [23] and Schey [57].

Consider three types of variables $\in \mathbb{R}^3$ that vary in space (x, y, z): (i) the scalar or zeroth order tensor ψ, (ii) the vector or first order tensor $\bar{\boldsymbol{a}}$ and (iii) the matrix or second order tensor $\boldsymbol{A}$ with components for the first and second order tensors defined as

$$\bar{\boldsymbol{a}} = \begin{bmatrix} a_1 \\ a_2 \\ a_3 \end{bmatrix}, \tag{A.6}$$

$$\boldsymbol{A} = \begin{bmatrix} A_{11} & A_{12} & A_{13} \\ A_{21} & A_{22} & A_{23} \\ A_{31} & A_{32} & A_{33} \end{bmatrix}. \tag{A.7}$$

Row i of the matrix $\boldsymbol{A}$ is identified by $\boldsymbol{A}_{i\bullet}$ and column j of matrix $\boldsymbol{A}$ is identified by $\boldsymbol{A}_{\bullet j}$.

A.3.1 Gradient (∇)

$$\nabla\psi = \begin{bmatrix} \dfrac{\partial\psi}{\partial x} \\ \dfrac{\partial\psi}{\partial y} \\ \dfrac{\partial\psi}{\partial z} \end{bmatrix} \tag{A.8}$$

$$\begin{aligned} \nabla\bar{\boldsymbol{a}} &= \begin{bmatrix} \nabla a_1 & \nabla a_2 & \nabla a_3 \end{bmatrix} \\ &= \begin{bmatrix} \dfrac{\partial a_1}{\partial x} & \dfrac{\partial a_2}{\partial x} & \dfrac{\partial a_3}{\partial x} \\ \dfrac{\partial a_1}{\partial y} & \dfrac{\partial a_2}{\partial y} & \dfrac{\partial a_3}{\partial y} \\ \dfrac{\partial a_1}{\partial z} & \dfrac{\partial a_2}{\partial z} & \dfrac{\partial a_3}{\partial z} \end{bmatrix} \end{aligned} \tag{A.9}$$

A.3.2 Divergence ($\nabla\cdot$)

$$\nabla \cdot \bar{\boldsymbol{a}} = \frac{\partial a_1}{\partial x} + \frac{\partial a_2}{\partial y} + \frac{\partial a_3}{\partial z} \tag{A.10}$$

$$\begin{aligned} \nabla \cdot \boldsymbol{A} &= \begin{bmatrix} \nabla \cdot \boldsymbol{A}_{\bullet 1} \\ \nabla \cdot \boldsymbol{A}_{\bullet 2} \\ \nabla \cdot \boldsymbol{A}_{\bullet 3} \end{bmatrix} \\ &= \begin{bmatrix} \dfrac{\partial a_{11}}{\partial x} + \dfrac{\partial a_{21}}{\partial y} + \dfrac{\partial a_{31}}{\partial z} \\ \dfrac{\partial a_{12}}{\partial x} + \dfrac{\partial a_{22}}{\partial y} + \dfrac{\partial a_{32}}{\partial z} \\ \dfrac{\partial a_{13}}{\partial x} + \dfrac{\partial a_{23}}{\partial y} + \dfrac{\partial a_{33}}{\partial z} \end{bmatrix} \end{aligned} \tag{A.11}$$

A.3.3 Curl ($\nabla\times$)

$$\nabla \times \bar{\boldsymbol{a}} = \begin{bmatrix} \dfrac{\partial a_3}{\partial y} - \dfrac{\partial a_2}{\partial z} \\ \dfrac{\partial a_1}{\partial z} - \dfrac{\partial a_3}{\partial x} \\ \dfrac{\partial a_2}{\partial x} - \dfrac{\partial a_1}{\partial y} \end{bmatrix} \tag{A.12}$$

$$\begin{aligned} \nabla \times \boldsymbol{A} &= \begin{bmatrix} \nabla \times \boldsymbol{A}_{\bullet 1} \\ \nabla \times \boldsymbol{A}_{\bullet 2} \\ \nabla \times \boldsymbol{A}_{\bullet 3} \end{bmatrix} \\ &= \begin{bmatrix} \dfrac{\partial A_{31}}{\partial y} - \dfrac{\partial A_{21}}{\partial z} & \dfrac{\partial A_{32}}{\partial y} - \dfrac{\partial A_{22}}{\partial z} & \dfrac{\partial A_{33}}{\partial y} - \dfrac{\partial A_{23}}{\partial z} \\ \dfrac{\partial A_{11}}{\partial z} - \dfrac{\partial A_{31}}{\partial x} & \dfrac{\partial A_{12}}{\partial z} - \dfrac{\partial A_{32}}{\partial x} & \dfrac{\partial A_{13}}{\partial z} - \dfrac{\partial A_{33}}{\partial x} \\ \dfrac{\partial A_{21}}{\partial x} - \dfrac{\partial A_{11}}{\partial y} & \dfrac{\partial A_{22}}{\partial x} - \dfrac{\partial A_{12}}{\partial y} & \dfrac{\partial A_{23}}{\partial x} - \dfrac{\partial A_{13}}{\partial y} \end{bmatrix} \end{aligned} \tag{A.13}$$

A.3.4 Laplacian (∇^2)

$$\begin{aligned} \nabla^2\psi &= \nabla\cdot\nabla\psi \\ &= \frac{\partial^2\psi}{\partial x^2}+\frac{\partial^2\psi}{\partial y^2}+\frac{\partial^2\psi}{\partial z^2} \end{aligned} \tag{A.14}$$

$$\begin{aligned} \nabla^2\bar{\boldsymbol{a}} &= \nabla\cdot\nabla\bar{\boldsymbol{a}} \\ &= \begin{bmatrix} \nabla^2 a_1 \\ \nabla^2 a_2 \\ \nabla^2 a_3 \end{bmatrix} \\ &= \begin{bmatrix} \dfrac{\partial^2 a_1}{\partial x^2}+\dfrac{\partial^2 a_1}{\partial y^2}+\dfrac{\partial^2 a_1}{\partial z^2} \\ \dfrac{\partial^2 a_2}{\partial x^2}+\dfrac{\partial^2 a_2}{\partial y^2}+\dfrac{\partial^2 a_2}{\partial z^2} \\ \dfrac{\partial^2 a_3}{\partial x^2}+\dfrac{\partial^2 a_3}{\partial y^2}+\dfrac{\partial^2 a_3}{\partial z^2} \end{bmatrix} \end{aligned} \tag{A.15}$$

A.3.5 Vector Calculus Identities

Divergence Gradient Identity

$$\nabla\cdot(\nabla\bar{\boldsymbol{a}})=0 \tag{A.16}$$

Curl-Curl Identity

$$\nabla\times\nabla\times\bar{\boldsymbol{a}}=\nabla(\nabla\cdot\bar{\boldsymbol{a}})-\nabla^2\bar{\boldsymbol{a}} \tag{A.17}$$

Green's First Vector Theorem

$$\begin{aligned} \iiint_V \left[u(\nabla\times\bar{\boldsymbol{a}})\cdot(\nabla\times\bar{\boldsymbol{b}})-\bar{\boldsymbol{a}}\cdot(\nabla\times u\nabla\times\bar{\boldsymbol{b}})\right]\partial V \\ = \oiint_S u\left(\bar{\boldsymbol{a}}\times\nabla\times\bar{\boldsymbol{b}}\right)\cdot\hat{\boldsymbol{n}}\partial S \end{aligned} \tag{A.18}$$

A.4 Least Squares Algorithm

For the given over determined linear system of equations problem of the form

$$\boldsymbol{A}\bar{\boldsymbol{x}}=\bar{\boldsymbol{b}}, \tag{A.19}$$

a solution for the unknown vector $\bar{\boldsymbol{x}} \in \mathbb{R}^n$, where $\boldsymbol{A} \in \mathbb{R}^{m \times n}$, $\bar{\boldsymbol{b}} \in \mathbb{R}^m$ and $m \leq n$ is found by using a least squares approach [67] as follows. First, multiply each side of the equation by the transpose of $\boldsymbol{A}$ to get

$$\boldsymbol{A}^T \boldsymbol{A} \bar{\boldsymbol{x}} = \boldsymbol{A}^T \bar{\boldsymbol{b}}. \tag{A.20}$$

The $\boldsymbol{A}^T \boldsymbol{A}$ term can be inverted resulting in an expression for the unknown $\bar{\boldsymbol{x}}$.

$$\bar{\boldsymbol{x}} = \left(\boldsymbol{A}^T \boldsymbol{A}\right)^{-1} \boldsymbol{A}^T \bar{\boldsymbol{b}}. \tag{A.21}$$

Appendix B

Comparison of Vector Calculus and Tensor Notations

Show that

$$\nabla^2 \tilde{\boldsymbol{E}} = \nabla \cdot \left(\nabla \tilde{\boldsymbol{E}} \right). \tag{B.1}$$

Let $\tilde{\boldsymbol{E}}$ be expanded to its vector form $\tilde{\boldsymbol{E}} = \begin{bmatrix} \tilde{\boldsymbol{E}}_x & \tilde{\boldsymbol{E}}_y & \tilde{\boldsymbol{E}}_z \end{bmatrix}^T$.

Starting with the left hand side, the Laplacian of a vector (equation A.15) is expanded out to general component form,

$$\begin{aligned} L.H.S. &= \nabla^2 \tilde{\boldsymbol{E}} \\ &= \begin{bmatrix} \nabla^2 \tilde{\boldsymbol{E}}_x \\ \nabla^2 \tilde{\boldsymbol{E}}_y \\ \nabla^2 \tilde{\boldsymbol{E}}_z \end{bmatrix} \\ &= \begin{bmatrix} \dfrac{\partial^2 \tilde{\boldsymbol{E}}_x}{\partial x^2} + \dfrac{\partial^2 \tilde{\boldsymbol{E}}_x}{\partial y^2} + \dfrac{\partial^2 \tilde{\boldsymbol{E}}_x}{\partial z^2} \\ \dfrac{\partial^2 \tilde{\boldsymbol{E}}_y}{\partial x^2} + \dfrac{\partial^2 \tilde{\boldsymbol{E}}_y}{\partial y^2} + \dfrac{\partial^2 \tilde{\boldsymbol{E}}_y}{\partial z^2} \\ \dfrac{\partial^2 \tilde{\boldsymbol{E}}_z}{\partial x^2} + \dfrac{\partial^2 \tilde{\boldsymbol{E}}_z}{\partial y^2} + \dfrac{\partial^2 \tilde{\boldsymbol{E}}_z}{\partial z^2} \end{bmatrix}. \end{aligned} \tag{B.2}$$

Now, the right hand side of equation B.1 is expanded out into component form using the gradient of a vector (equation A.9) and the divergence of a second order tensor (equation A.11),

$$
\begin{aligned}
R.H.S. &= \nabla \cdot \left(\nabla \tilde{\boldsymbol{E}} \right) \\
&= \nabla \cdot \begin{bmatrix} \dfrac{\partial \tilde{\boldsymbol{E}}_x}{\partial x} & \dfrac{\partial \tilde{\boldsymbol{E}}_y}{\partial x} & \dfrac{\partial \tilde{\boldsymbol{E}}_z}{\partial x} \\ \dfrac{\partial \tilde{\boldsymbol{E}}_x}{\partial y} & \dfrac{\partial \tilde{\boldsymbol{E}}_y}{\partial y} & \dfrac{\partial \tilde{\boldsymbol{E}}_z}{\partial y} \\ \dfrac{\partial \tilde{\boldsymbol{E}}_x}{\partial z} & \dfrac{\partial \tilde{\boldsymbol{E}}_y}{\partial z} & \dfrac{\partial \tilde{\boldsymbol{E}}_z}{\partial z} \end{bmatrix} \qquad \text{(B.3)} \\
&= \begin{bmatrix} \dfrac{\partial^2 \tilde{\boldsymbol{E}}_x}{\partial x^2} + \dfrac{\partial^2 \tilde{\boldsymbol{E}}_x}{\partial y^2} + \dfrac{\partial^2 \tilde{\boldsymbol{E}}_x}{\partial z^2} \\ \dfrac{\partial^2 \tilde{\boldsymbol{E}}_y}{\partial x^2} + \dfrac{\partial^2 \tilde{\boldsymbol{E}}_y}{\partial y^2} + \dfrac{\partial^2 \tilde{\boldsymbol{E}}_y}{\partial z^2} \\ \dfrac{\partial^2 \tilde{\boldsymbol{E}}_z}{\partial x^2} + \dfrac{\partial^2 \tilde{\boldsymbol{E}}_z}{\partial y^2} + \dfrac{\partial^2 \tilde{\boldsymbol{E}}_z}{\partial z^2} \end{bmatrix} = L.H.S. \qquad \text{(B.4)}
\end{aligned}
$$

Appendix C

Tables of Statistics for Verification Runs

Some additional results from the data presented in Chapter 4 are presented here. The detailed RMS statistics for the 27 sampling locations for each source type; infinite, line and point; are presented in that order. After each table of RMS statistics, the signals at 6 selected sampling locations are plotted for the given source type and the Neumann pulse.

	Gaussian Pulse			Neumann Pulse			Mod. Sinusoid		
No.	E_x	E_y	E_z	E_x	E_y	E_z	E_x	E_y	E_z
1	0.0008	0.0060	0.0044	0.0015	0.0052	0.0120	0.0059	0.0079	0.0638
2	0.0021	0.0052	0.0043	0.0026	0.0112	0.0133	0.0087	0.0205	0.0356
3	0.0005	0.0131	0.0111	0.0022	0.0038	0.0108	0.0070	0.0566	0.0472
4	0.0018	0.0010	0.0551	0.0030	0.0052	0.0699	0.0423	0.0363	0.0388
5	0.0010	0.0048	0.0522	0.0019	0.0016	0.0671	0.0312	0.0276	0.0571
6	0.0016	0.0515	0.0516	0.0067	0.0837	0.0661	0.0071	0.0518	0.0604
7	0.0108	0.0047	0.0951	0.0032	0.0072	0.1309	0.0238	0.0584	0.0755
8	0.0005	0.0016	0.1006	0.0017	0.0005	0.1196	0.0105	0.0369	0.0916
9	0.0055	0.0500	0.0977	0.0128	0.0745	0.1264	0.0394	0.0569	0.0499
10	0.0073	0.0069	0.1353	0.0043	0.0053	0.1805	0.0463	0.0139	0.1096
11	0.0052	0.0056	0.1382	0.0066	0.0088	0.1707	0.0320	0.0262	0.0619
12	0.0123	0.0417	0.1371	0.0044	0.0604	0.1732	0.0196	0.0677	0.0933
13	0.0005	0.0009	0.1723	0.0164	0.0160	0.2133	0.0856	0.0918	0.2132
14	0.0036	0.0072	0.1703	0.0048	0.0009	0.2104	0.0328	0.0386	0.0448
15	0.0008	0.0303	0.1669	0.0007	0.0520	0.2137	0.0114	0.0253	0.1640
16	0.0064	0.0022	0.1974	0.0162	0.0092	0.2495	0.0075	0.0203	0.1328
17	0.0003	0.0015	0.1946	0.0049	0.0009	0.2456	0.0166	0.0630	0.1238
18	0.0114	0.0288	0.1963	0.0100	0.0413	0.2465	0.0277	0.0605	0.1100
19	0.0004	0.0029	0.2148	0.0025	0.0072	0.2714	0.0116	0.0502	0.2662
20	0.0002	0.0027	0.2173	0.0130	0.0170	0.2663	0.0877	0.1289	0.2356
21	0.0003	0.0203	0.2128	0.0011	0.0338	0.2702	0.0136	0.0877	0.0996
22	0.0040	0.0003	0.2325	0.0021	0.0016	0.2920	0.0234	0.0443	0.2222
23	0.0004	0.0044	0.2317	0.0027	0.0016	0.2950	0.0274	0.0575	0.1264
24	0.0007	0.0187	0.2312	0.0041	0.0278	0.2881	0.0330	0.0246	0.1759
25	0.0009	0.0024	0.2460	0.0010	0.0012	0.3092	0.0723	0.0321	0.2434
26	0.0016	0.0021	0.2453	0.0004	0.0078	0.3048	0.0131	0.0179	0.1313
27	0.0049	0.0134	0.2450	0.0008	0.0246	0.3070	0.0135	0.0184	0.1453

Table C.1: RMS of measured signal for an infinite source at $y = -1.00$. The statistics are presented for a signal that is normalized so that the maximum value of the reference is set to 1.00. All statistics are in meters.

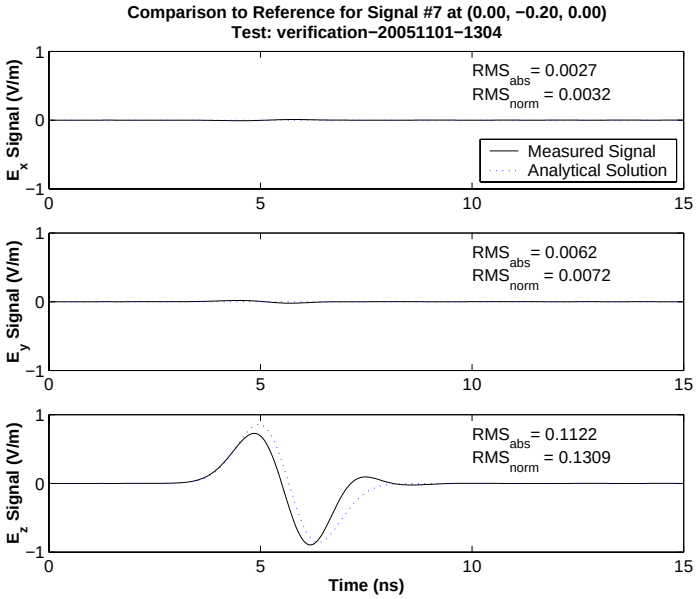

Figure C.1: Electric field intensity for a plane wave with Neumann pulse at observation point 7 with the signal originating at $y = -1.00$.

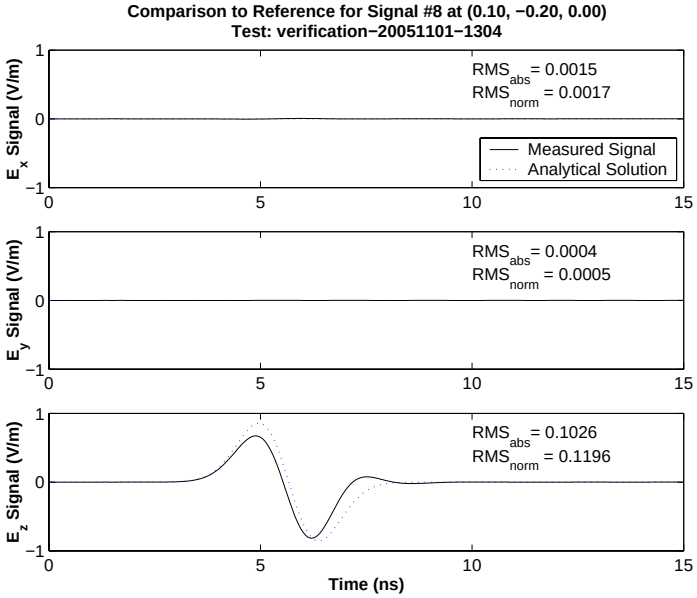

Figure C.2: Electric field intensity for a plane wave with Neumann pulse at observation point 8 with the signal originating at $y = -1.00$.

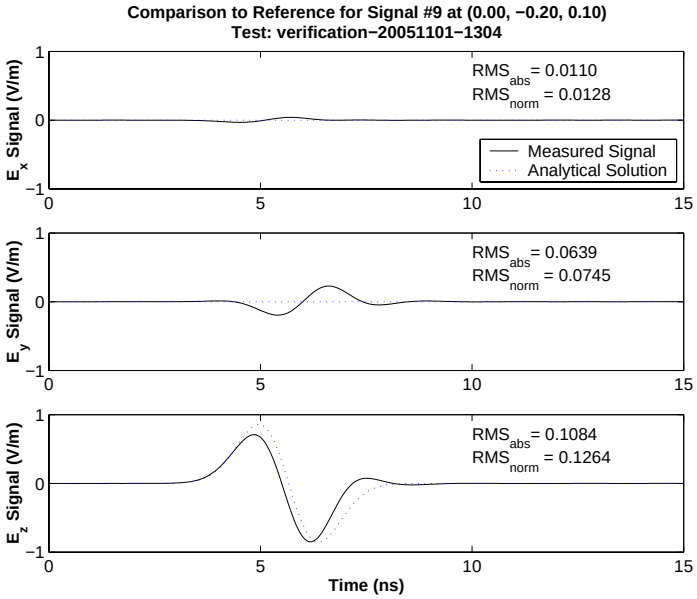

Figure C.3: Electric field intensity for a plane wave with Neumann pulse at observation point 9 with the signal originating at $y = -1.00$.

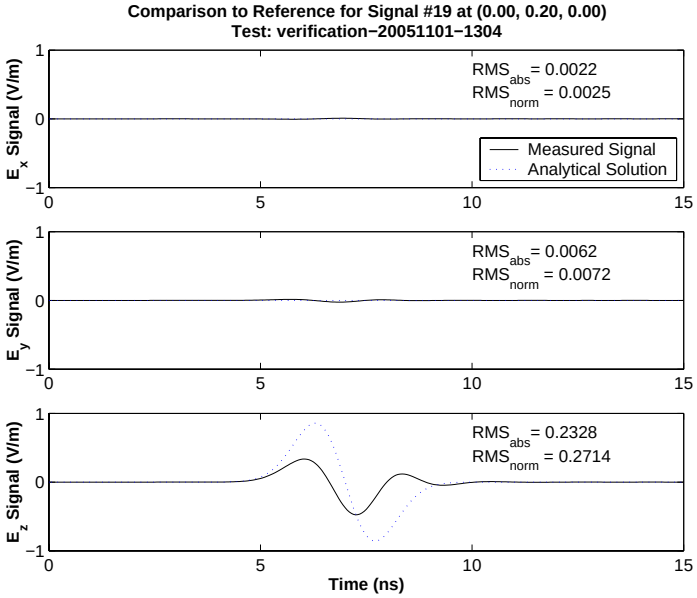

Figure C.4: Electric field intensity for a plane wave with Neumann pulse at observation point 19 with the signal originating at $y = -1.00$.

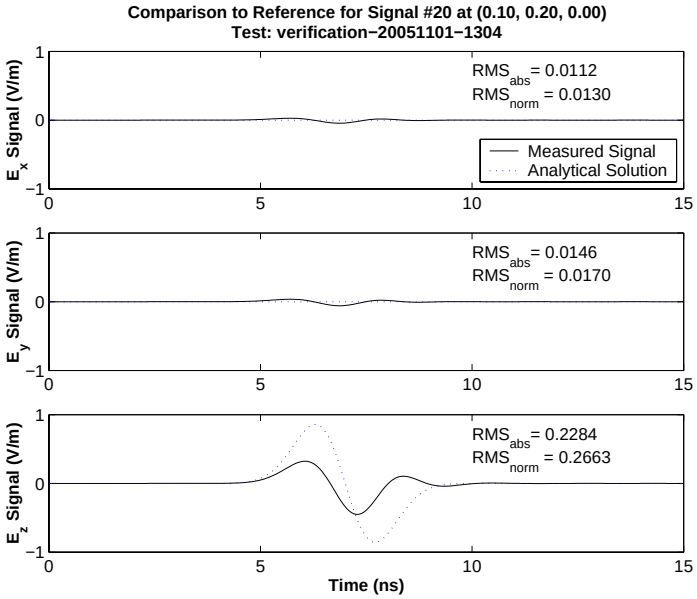

Figure C.5: Electric field intensity for a plane wave with Neumann pulse at observation point 20 with the signal originating at $y = -1.00$.

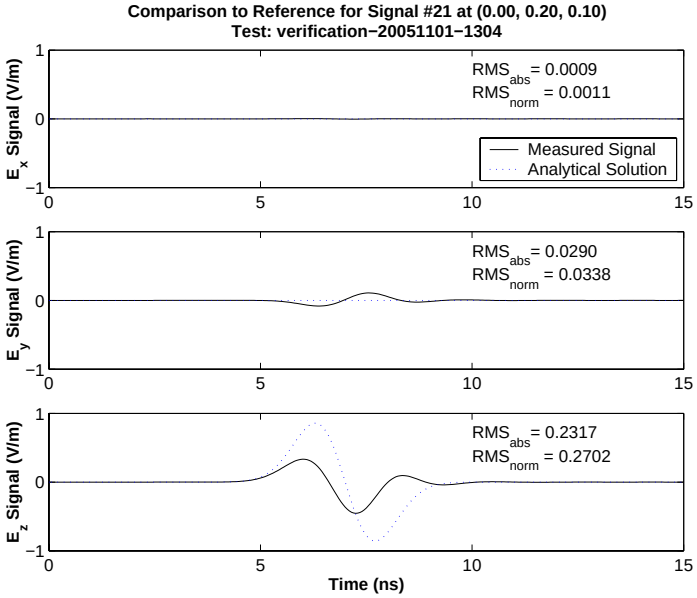

Figure C.6: Electric field intensity for a plane wave with Neumann pulse at observation point 21 with the signal originating at $y = -1.00$.

	Gaussian Pulse			Neumann Pulse			Mod. Sinusoid		
No.	E_x	E_y	E_z	E_x	E_y	E_z	E_x	E_y	E_z
1	0.0020	0.0071	0.0629	0.0044	0.0194	0.0282	0.0132	0.0656	0.0395
2	0.0029	0.0023	0.0629	0.0019	0.0015	0.0277	0.0183	0.0327	0.0411
3	0.0012	0.0037	0.0570	0.0045	0.0249	0.0292	0.0120	0.0585	0.0121
4	0.0032	0.0045	0.0477	0.0076	0.0198	0.0498	0.0092	0.0288	0.0457
5	0.0141	0.0038	0.0366	0.0030	0.0040	0.0324	0.0358	0.0118	0.0837
6	0.0015	0.0965	0.0420	0.0018	0.1323	0.0415	0.0348	0.0765	0.0743
7	0.0028	0.0067	0.0553	0.0037	0.0129	0.0932	0.0151	0.0224	0.0784
8	0.0045	0.0037	0.0454	0.0023	0.0116	0.0814	0.0264	0.0234	0.0584
9	0.0006	0.1006	0.0538	0.0033	0.1268	0.0882	0.0125	0.0437	0.0945
10	0.0044	0.0057	0.0767	0.0025	0.0023	0.1473	0.0200	0.0095	0.1864
11	0.0036	0.0042	0.0686	0.0031	0.0035	0.1278	0.0635	0.0107	0.1980
12	0.0024	0.0866	0.0724	0.0174	0.1079	0.1263	0.0312	0.0738	0.1158
13	0.0039	0.0073	0.0983	0.0055	0.0088	0.1616	0.0074	0.0191	0.1968
14	0.0034	0.0006	0.0937	0.0067	0.0024	0.1463	0.0232	0.0123	0.2069
15	0.0011	0.0858	0.0970	0.0024	0.1046	0.1568	0.0462	0.1017	0.2428
16	0.0013	0.0037	0.1221	0.0007	0.0084	0.1907	0.0574	0.0279	0.2630
17	0.0005	0.0050	0.1194	0.0052	0.0158	0.1840	0.0079	0.0741	0.2407
18	0.0012	0.0755	0.1170	0.0108	0.0954	0.2038	0.0484	0.1019	0.2905
19	0.0007	0.0056	0.1473	0.0023	0.0005	0.2232	0.0104	0.0388	0.2358
20	0.0121	0.0168	0.1462	0.0029	0.0063	0.2302	0.0967	0.1196	0.2891
21	0.0017	0.0630	0.1435	0.0088	0.0887	0.2407	0.0203	0.0206	0.3396
22	0.0010	0.0080	0.1686	0.0010	0.0087	0.2537	0.0071	0.0533	0.2884
23	0.0033	0.0050	0.1674	0.0054	0.0077	0.2462	0.0209	0.0188	0.2133
24	0.0010	0.0599	0.1667	0.0017	0.0779	0.2611	0.0121	0.0230	0.3315
25	0.0027	0.0054	0.1870	0.0122	0.0149	0.2876	0.0196	0.0265	0.3050
26	0.0010	0.0031	0.1863	0.0027	0.0134	0.2713	0.0315	0.1014	0.2826
27	0.0007	0.0546	0.1866	0.0020	0.0692	0.2660	0.0355	0.0468	0.3043

Table C.2: RMS of measured signal for a line source at $y = -1.00, z = 0.00$. The statistics are presented for a signal that is normalized so that the maximum value of the reference is set to 1.00. All statistics are in meters.

	Gaussian Pulse			Neumann Pulse			Mod. Sinusoid		
No.	E_x	E_y	E_z	E_x	E_y	E_z	E_x	E_y	E_z
1	0.0016	0.0077	0.0327	0.0056	0.0080	0.0235	0.0302	0.0292	0.0746
2	0.0049	0.0250	0.0382	0.0071	0.0220	0.0283	0.0243	0.0206	0.0375
3	0.0025	0.0057	0.0513	0.0029	0.0061	0.0347	0.0135	0.0478	0.0604
4	0.0034	0.1930	0.0279	0.0029	0.2657	0.0353	0.0225	0.1478	0.0482
5	0.0053	0.1813	0.0261	0.0241	0.2505	0.0306	0.0130	0.1416	0.0590
6	0.0013	0.0937	0.0437	0.0032	0.1779	0.0460	0.0480	0.1642	0.0279
7	0.0007	0.1437	0.0487	0.0077	0.2140	0.0796	0.0337	0.1130	0.0665
8	0.0038	0.1419	0.0514	0.0141	0.1933	0.0732	0.0128	0.1028	0.0961
9	0.0018	0.0764	0.0484	0.0178	0.1204	0.0851	0.0105	0.0614	0.0844
10	0.0028	0.1170	0.0775	0.0026	0.1593	0.1427	0.0130	0.0782	0.1368
11	0.0052	0.1204	0.0757	0.0048	0.1387	0.1208	0.0335	0.0993	0.1187
12	0.0025	0.0509	0.0738	0.0026	0.0951	0.1221	0.0141	0.1044	0.1818
13	0.0016	0.0875	0.1091	0.0129	0.1167	0.1572	0.0170	0.0995	0.2460
14	0.0050	0.0803	0.1043	0.0055	0.1129	0.1695	0.0059	0.0768	0.2151
15	0.0048	0.0333	0.0986	0.0037	0.0567	0.1491	0.0417	0.0649	0.2726
16	0.0008	0.0755	0.1315	0.0039	0.0847	0.2067	0.0229	0.0933	0.2823
17	0.0100	0.0639	0.1279	0.0120	0.1028	0.1805	0.0081	0.0980	0.2692
18	0.0026	0.0162	0.1282	0.0011	0.0489	0.1879	0.0162	0.0641	0.3116
19	0.0019	0.0638	0.1520	0.0024	0.0775	0.2198	0.0137	0.0866	0.3583
20	0.0017	0.0599	0.1496	0.0182	0.0921	0.2093	0.0146	0.0817	0.3126
21	0.0006	0.0164	0.1532	0.0038	0.0424	0.2121	0.0165	0.0872	0.2104
22	0.0030	0.0574	0.1737	0.0204	0.0652	0.2499	0.0593	0.1821	0.3417
23	0.0024	0.0586	0.1737	0.0033	0.0633	0.2462	0.0559	0.0502	0.2783
24	0.0011	0.0107	0.1724	0.0056	0.0387	0.2311	0.0692	0.0444	0.2855
25	0.0021	0.0531	0.1942	0.0019	0.0524	0.2784	0.1177	0.0716	0.3523
26	0.0016	0.0544	0.1930	0.0047	0.0525	0.2613	0.0440	0.0752	0.2805
27	0.0022	0.0159	0.1915	0.0082	0.0214	0.2522	0.0196	0.0451	0.3088

Table C.3: RMS of measured signal for a line source at $y = -1.00, z = 0.25$. The statistics are presented for a signal that is normalized so that the maximum value of the reference is set to 1.00. All statistics are in meters.

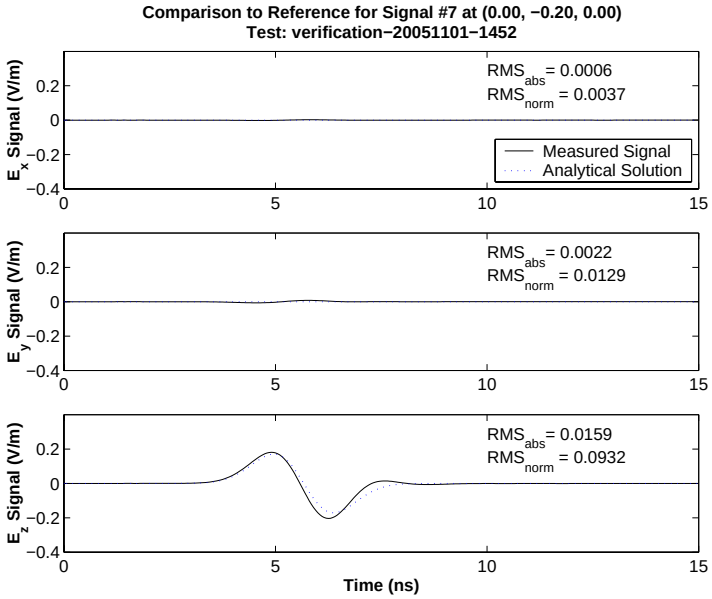

Figure C.7: Electric field intensity for a cylindrical wave with Neumann pulse at observation point 7 with the signal originating at $y = -1.00, z = 0.00$.

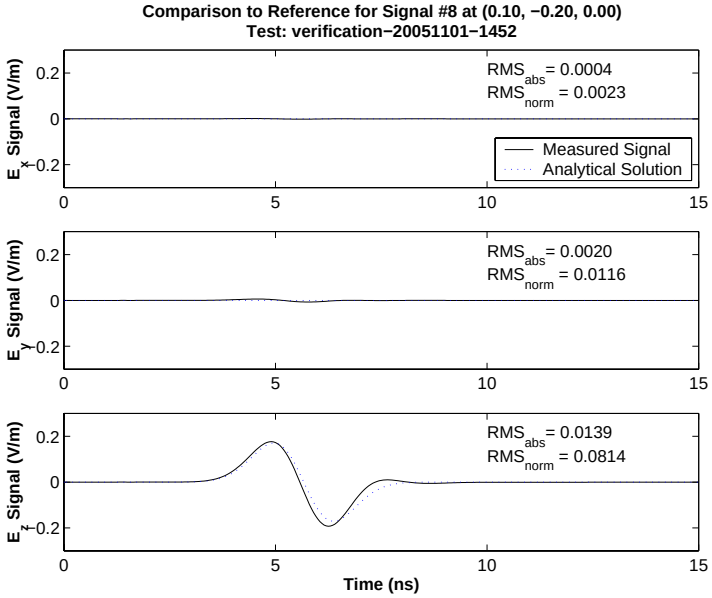

Figure C.8: Electric field intensity for a cylindrical wave with Neumann pulse at observation point 8 with the signal originating at $y = -1.00, z = 0.00$.

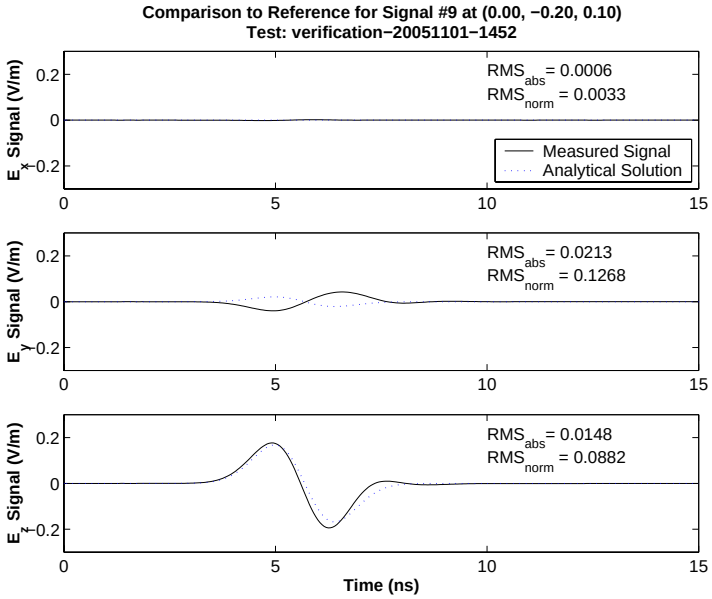

Figure C.9: Electric field intensity for a cylindrical wave with Neumann pulse at observation point 9 with the signal originating at $y = -1.00, z = 0.00$.

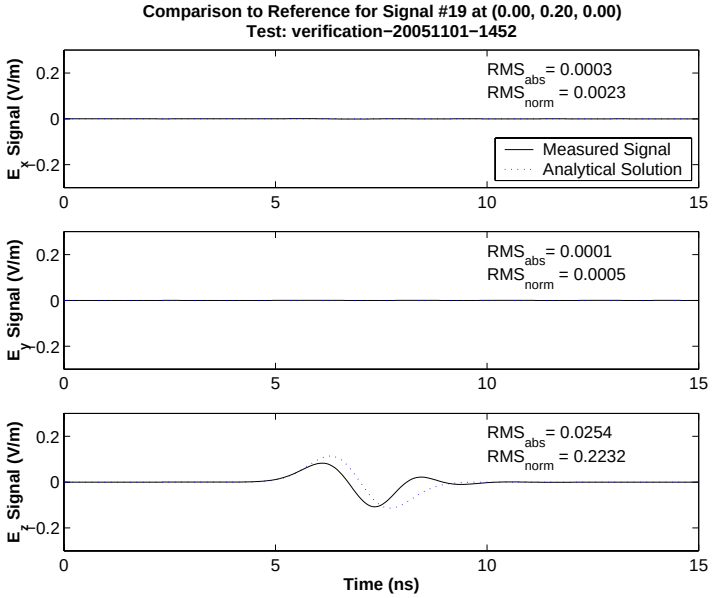

Figure C.10: Electric field intensity for a cylindrical wave with Neumann pulse at observation point 19 with the signal originating at $y = -1.00, z = 0.00$.

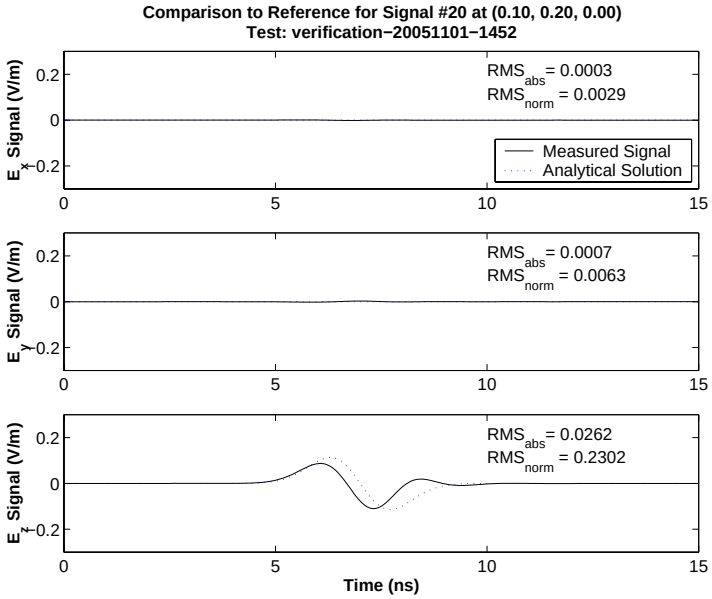

Figure C.11: Electric field intensity for a cylindrical wave with Neumann pulse at observation point 20 with the signal originating at $y = -1.00, z = 0.00$.

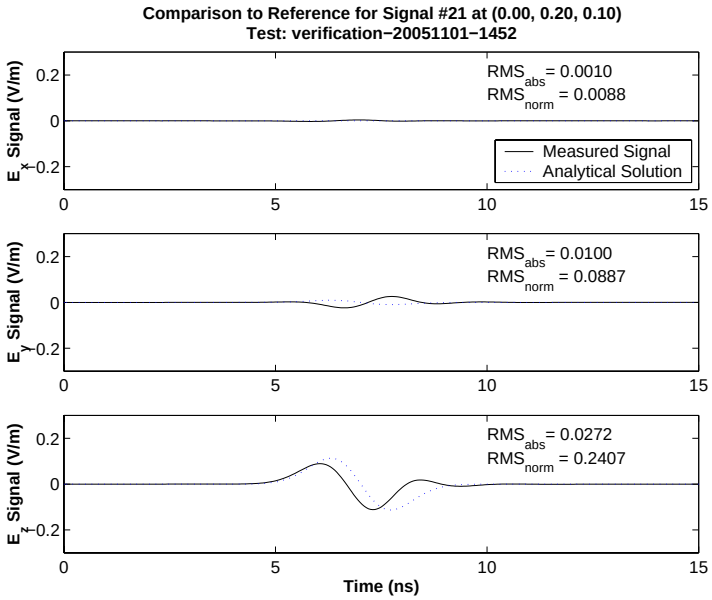

Figure C.12: Electric field intensity for a cylindrical wave with Neumann pulse at observation point 21 with the signal originating at $y = -1.00, z = 0.00$.

	Gaussian Pulse			Neumann Pulse			Mod. Sinusoid		
No.	E_x	E_y	E_z	E_x	E_y	E_z	E_x	E_y	E_z
1	0.0068	0.0123	0.0338	0.0048	0.0057	0.0385	0.0016	0.0077	0.0327
2	0.0064	0.0085	0.0325	0.0065	0.0424	0.0631	0.0049	0.0250	0.0382
3	0.0038	0.0129	0.0335	0.0166	0.0343	0.0156	0.0025	0.0057	0.0513
4	0.0009	0.0312	0.0657	0.0223	0.0264	0.0218	0.0034	0.1930	0.0279
5	0.0103	0.0149	0.0670	0.0091	0.0335	0.0349	0.0053	0.1813	0.0261
6	0.0034	0.1236	0.0575	0.0938	0.0346	0.1475	0.0013	0.0937	0.0437
7	0.0058	0.0205	0.1075	0.0109	0.0235	0.1501	0.0007	0.1437	0.0487
8	0.0039	0.0014	0.1026	0.0222	0.0320	0.0485	0.0038	0.1419	0.0514
9	0.0024	0.1270	0.1025	0.0296	0.0493	0.0498	0.0018	0.0764	0.0484
10	0.0098	0.0018	0.1759	0.0204	0.0285	0.1122	0.0028	0.1170	0.0775
11	0.0120	0.0116	0.1212	0.0188	0.0554	0.0359	0.0052	0.1204	0.0757
12	0.0054	0.1384	0.1297	0.0588	0.1005	0.0524	0.0025	0.0509	0.0738
13	0.0013	0.0148	0.1863	0.0721	0.0689	0.1440	0.0016	0.0875	0.1091
14	0.0054	0.0085	0.2089	0.0666	0.0608	0.0897	0.0050	0.0803	0.1043
15	0.0059	0.1309	0.1836	0.0834	0.0721	0.0600	0.0048	0.0333	0.0986
16	0.0085	0.0426	0.2385	0.0288	0.0316	0.1373	0.0008	0.0755	0.1315
17	0.0192	0.0522	0.2203	0.0506	0.0275	0.0909	0.0100	0.0639	0.1279
18	0.0057	0.1321	0.2230	0.0598	0.1557	0.0950	0.0026	0.0162	0.1282
19	0.0009	0.0041	0.2464	0.0251	0.0446	0.0937	0.0019	0.0638	0.1520
20	0.0048	0.0125	0.2338	0.0340	0.0695	0.0556	0.0017	0.0599	0.1496
21	0.0025	0.1281	0.2875	0.0328	0.0452	0.2203	0.0006	0.0164	0.1532
22	0.0126	0.0040	0.2765	0.0340	0.0262	0.1674	0.0030	0.0574	0.1737
23	0.0067	0.0218	0.2985	0.1215	0.0720	0.2039	0.0024	0.0586	0.1737
24	0.0055	0.1300	0.2784	0.0246	0.0449	0.2125	0.0011	0.0107	0.1724
25	0.0099	0.0060	0.3437	0.0502	0.0544	0.3014	0.0021	0.0531	0.1942
26	0.0184	0.0041	0.3074	0.0350	0.0721	0.3832	0.0016	0.0544	0.1930
27	0.0036	0.1152	0.3204	0.0334	0.1393	0.3025	0.0022	0.0159	0.1915

Table C.4: RMS of measured signal for a point source at $(0.00, -1.00, 0.00)$. The statistics are presented for a signal that is normalized so that the maximum value of the reference is set to 1.00. All statistics are in meters.

	Gaussian Pulse			Neumann Pulse			Mod. Sinusoid		
No.	E_x	E_y	E_z	E_x	E_y	E_z	E_x	E_y	E_z
1	0.0168	0.2452	0.0493	0.0047	0.0102	0.0212	0.0200	0.0346	0.0464
2	0.0104	0.0103	0.0482	0.0113	0.0203	0.0192	0.0141	0.0611	0.0141
3	0.0031	0.0139	0.0772	0.0151	0.0249	0.0324	0.0288	0.0485	0.0421
4	0.0016	0.1810	0.0662	0.0011	0.2715	0.0495	0.0213	0.1356	0.0913
5	0.0045	0.2057	0.0770	0.0033	0.2826	0.0526	0.0438	0.1226	0.1136
6	0.0072	0.0803	0.0809	0.0055	0.1650	0.0440	0.0383	0.0620	0.0562
7	0.0025	0.1614	0.0747	0.0117	0.2422	0.0953	0.0598	0.1058	0.1430
8	0.0045	0.1425	0.0528	0.0312	0.2374	0.1132	0.0482	0.1871	0.0827
9	0.0114	0.0643	0.0886	0.0064	0.1136	0.0856	0.0084	0.0887	0.1705
10	0.0010	0.1113	0.0768	0.0074	0.1884	0.1789	0.0183	0.1076	0.1544
11	0.0025	0.1215	0.0813	0.0055	0.1941	0.1474	0.0168	0.1156	0.0675
12	0.0032	0.0358	0.0706	0.0202	0.1033	0.1196	0.0147	0.0746	0.2136
13	0.0061	0.0972	0.0664	0.0047	0.1464	0.1453	0.0223	0.1077	0.2733
14	0.0020	0.1020	0.0909	0.0024	0.1274	0.1737	0.0913	0.0716	0.2902
15	0.0039	0.0473	0.0916	0.0132	0.0808	0.1504	0.0245	0.0738	0.2132
16	0.0075	0.0646	0.0996	0.0051	0.0961	0.2155	0.0197	0.1270	0.3430
17	0.0020	0.0907	0.0902	0.0101	0.1077	0.2024	0.0211	0.0646	0.3500
18	0.0107	0.0375	0.0938	0.0129	0.0844	0.1837	0.0280	0.0522	0.1847
19	0.0081	0.0718	0.0964	0.0051	0.0907	0.2152	0.0404	0.0879	0.3276
20	0.0026	0.0619	0.0921	0.0060	0.0834	0.2402	0.0375	0.0730	0.3579
21	0.0007	0.0354	0.1015	0.0153	0.1061	0.2181	0.0615	0.0726	0.1666
22	0.0027	0.0627	0.1122	0.0204	0.0622	0.2516	0.0562	0.0561	0.3250
23	0.0072	0.0625	0.1070	0.0129	0.0630	0.2465	0.0533	0.0759	0.4522
24	0.0017	0.0344	0.0985	0.0039	0.0664	0.2067	0.0935	0.0571	0.2222
25	0.0054	0.0551	0.1264	0.0048	0.0760	0.2864	0.0239	0.0770	0.3514
26	0.0049	0.0497	0.1269	0.0114	0.0493	0.2649	0.0211	0.1099	0.4388
27	0.0028	0.0332	0.1170	0.0061	0.0743	0.2345	0.0189	0.0617	0.3370

Table C.5: RMS of measured signal for a point source at $(0.00, -1.00, 0.25)$. The statistics are presented for a signal that is normalized so that the maximum value of the reference is set to 1.00. All statistics are in meters.

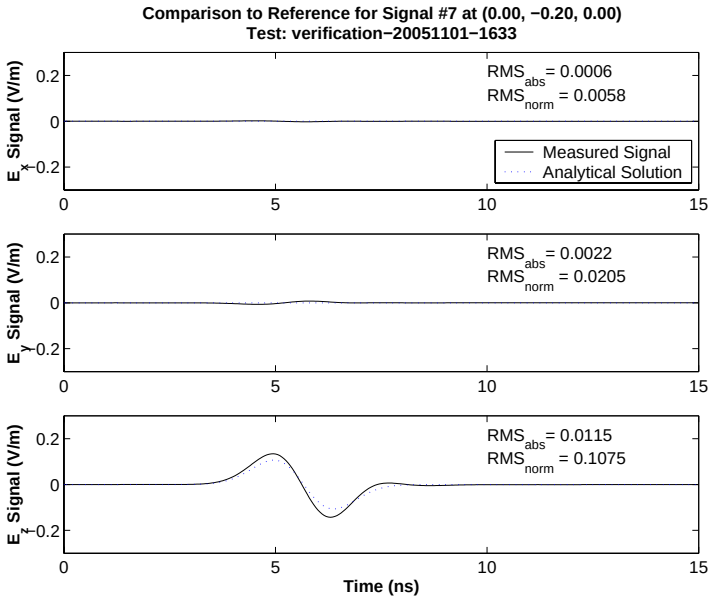

Figure C.13: Electric field intensity for a spherical wave with Neumann pulse at observation point 7 with the signal originating at $(0.00, -1.00, 0.00)$.

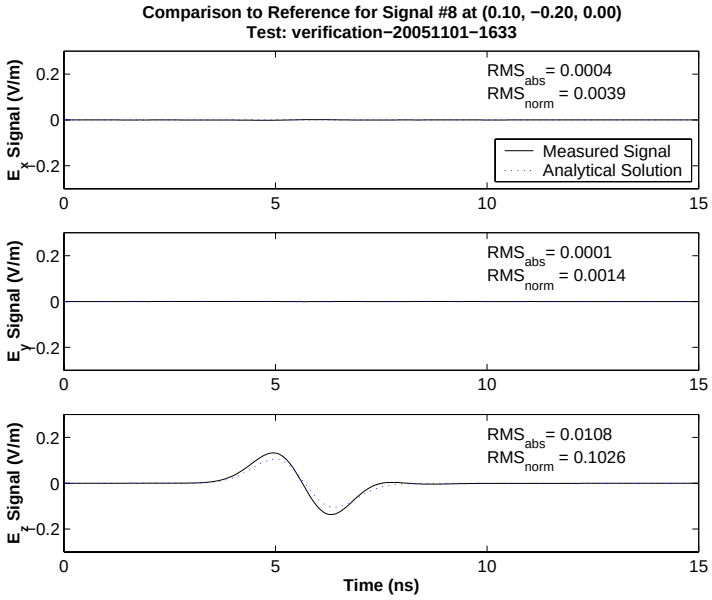

Figure C.14: Electric field intensity for a spherical wave with Neumann pulse at observation point 8 with the signal originating at $(0.00, -1.00, 0.00)$.

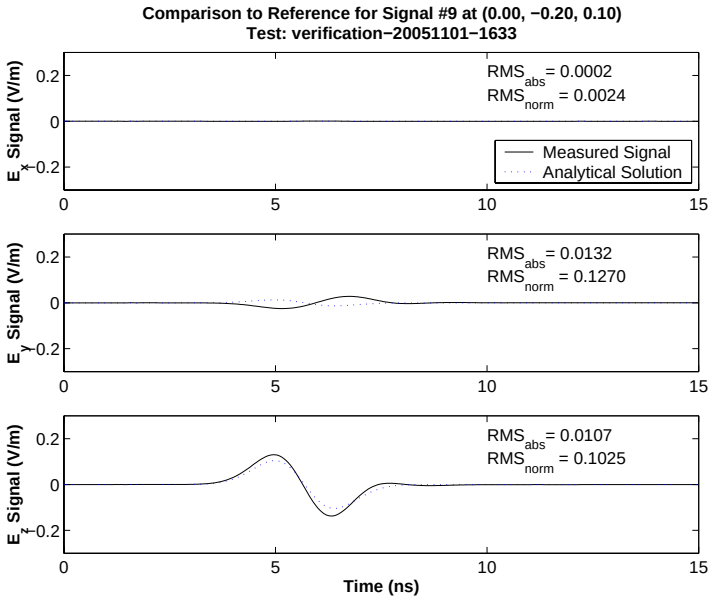

Figure C.15: Electric field intensity for a spherical wave with Neumann pulse at observation point 9 with the signal originating at $(0.00, -1.00, 0.00)$.

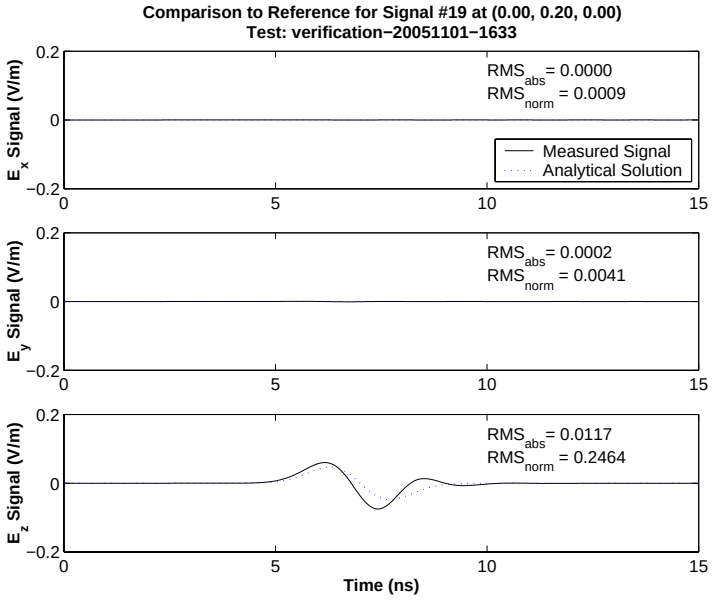

Figure C.16: Electric field intensity for a spherical wave with Neumann pulse at observation point 19 with the signal originating at $(0.00, -1.00, 0.00)$.

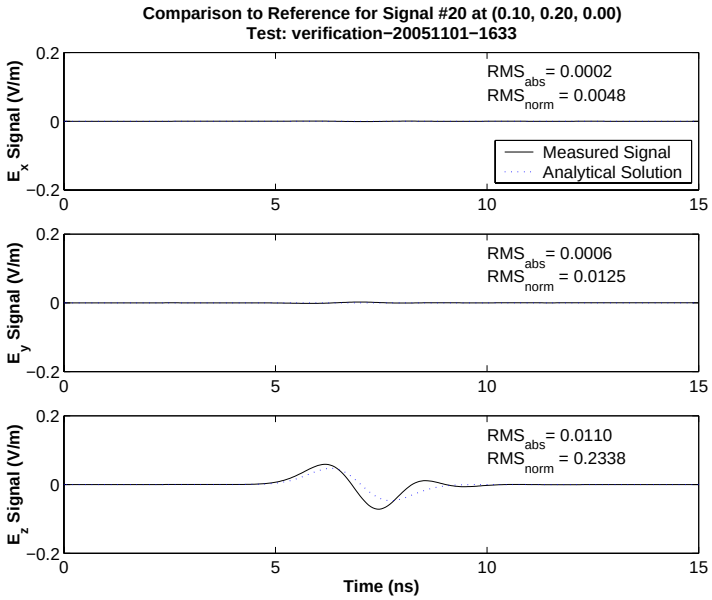

Figure C.17: Electric field intensity for a spherical wave with Neumann pulse at observation point 20 with the signal originating at $(0.00, -1.00, 0.00)$.

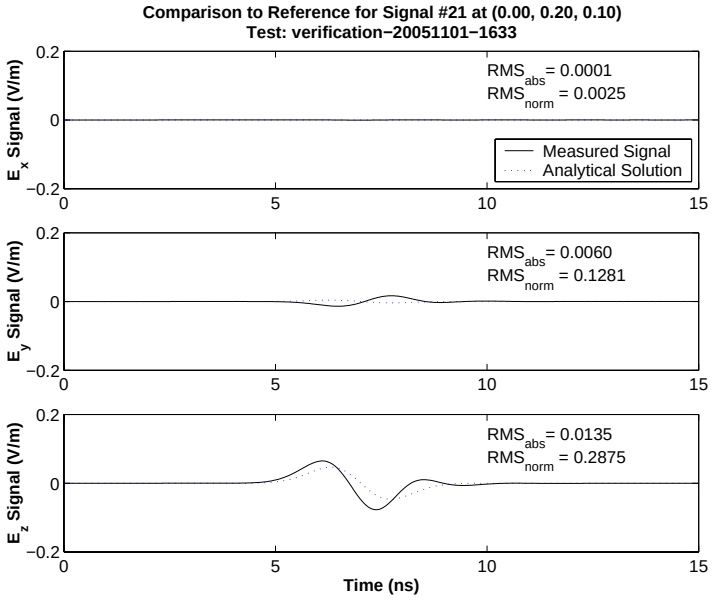

Figure C.18: Electric field intensity for a spherical wave with Neumann pulse at observation point 21 with the signal originating at $(0.00, -1.00, 0.00)$.

Appendix D

Position Error Statistics for Time Difference of Arrival Algorithms

This appendix provides the detailed data from the experiments described in Chapter 5. First, five tables of position error data is presented for the linear approximation solution of the TDOA algorithm and the intersection of headings methods. At the end of the appendix are 3 sets of plots showing the phase error that is introduced by the zeroth order vector finite elements.

	Actual Position			Measured Position			Error		
No.	x_{act}	y_{act}	z_{act}	x_{meas}	y_{meas}	z_{meas}	x_{err}	y_{err}	z_{err}
1	-0.5000	-1.0000	-0.5000	-0.3106	-0.7273	-0.3059	0.1894	0.2727	0.1941
2	0.0000	-1.0000	-0.5000	0.0000	-0.6012	-0.2118	0.0000	0.3988	0.2882
3	0.5000	-1.0000	-0.5000	0.3106	-0.7273	-0.3059	-0.1894	0.2727	0.1941
4	-0.5000	-1.0000	0.0000	-0.2838	-0.6920	0.0442	0.2162	0.3080	0.0442
5	0.0000	-1.0000	0.0000	0.0000	-0.5413	0.0674	0.0000	0.4587	0.0674
6	0.5000	-1.0000	0.0000	0.2838	-0.6920	0.0442	-0.2162	0.3080	0.0442
7	-0.5000	-1.0000	0.5000	-0.2006	-0.5689	0.3003	0.2994	0.4311	-0.1997
8	0.0000	-1.0000	0.5000	0.0000	-0.5091	0.2655	0.0000	0.4909	-0.2345
9	0.5000	-1.0000	0.5000	0.2006	-0.5689	0.3003	-0.2994	0.4311	-0.1997
10	-0.5000	-0.8000	-0.5000	-0.4086	-0.7007	-0.4075	0.0914	0.0993	0.0925
11	0.0000	-0.8000	-0.5000	0.0000	-0.5199	-0.2304	0.0000	0.2801	0.2696
12	0.5000	-0.8000	-0.5000	0.4086	-0.7007	-0.4075	-0.0914	0.0993	0.0925
13	-0.5000	-0.8000	0.0000	-0.4534	-0.7495	0.0093	0.0466	0.0505	0.0093
14	0.0000	-0.8000	0.0000	0.0000	-0.4555	0.0671	0.0000	0.3445	0.0671
15	0.5000	-0.8000	0.0000	0.4534	-0.7495	0.0093	-0.0466	0.0505	0.0093
16	-0.5000	-0.8000	0.5000	-0.2115	-0.4865	0.3052	0.2885	0.3135	-0.1948
17	0.0000	-0.8000	0.5000	0.0000	-0.4320	0.2567	0.0000	0.3680	-0.2433
18	0.5000	-0.8000	0.5000	0.2115	-0.4865	0.3052	-0.2885	0.3135	-0.1948
19	-0.5000	-0.6000	-0.5000	-0.7376	-0.7764	-0.7403	-0.2376	-0.1764	-0.2403
20	0.0000	-0.6000	-0.5000	0.0000	-0.4447	-0.2706	0.0000	0.1553	0.2294
21	0.5000	-0.6000	-0.5000	0.7376	-0.7764	-0.7403	0.2376	-0.1764	-0.2403
22	-0.5000	-0.6000	0.0000	-0.4534	-0.5643	0.0092	0.0466	0.0357	0.0092
23	0.0000	-0.6000	0.0000	0.0000	-0.3820	0.0641	0.0000	0.2180	0.0641
24	0.5000	-0.6000	0.0000	0.4534	-0.5643	0.0092	-0.0466	0.0357	0.0092
25	-0.5000	-0.6000	0.5000	-0.2322	-0.4012	0.3130	0.2678	0.1988	-0.1870
26	0.0000	-0.6000	0.5000	0.0000	-0.3712	0.2533	0.0000	0.2288	-0.2467
27	0.5000	-0.6000	0.5000	0.2322	-0.4012	0.3130	-0.2678	0.1988	-0.1870

Table D.1: Measurement errors using linearized approximation method. The summary statistics are provided in Table 5.1. All values are in meters.

	Actual Position			Measured Position			Error		
No.	x_{act}	y_{act}	z_{act}	x_{meas}	y_{meas}	z_{meas}	x_{err}	y_{err}	z_{err}
1	-0.5000	-1.0000	-0.5000	-0.4997	-1.0008	-0.4997	0.0003	-0.0008	0.0003
2	0.0000	-1.0000	-0.5000	0.0000	-1.0015	-0.5001	0.0000	-0.0015	-0.0001
3	0.5000	-1.0000	-0.5000	0.4997	-1.0008	-0.4997	-0.0003	-0.0008	0.0003
4	-0.5000	-1.0000	0.0000	-0.4996	-1.0005	-0.0001	0.0004	-0.0005	-0.0001
5	0.0000	-1.0000	0.0000	0.0000	-1.0016	-0.0000	0.0000	-0.0016	-0.0000
6	0.5000	-1.0000	0.0000	0.4996	-1.0005	-0.0001	-0.0004	-0.0005	-0.0001
7	-0.5000	-1.0000	0.5000	-0.4998	-1.0009	0.4998	0.0002	-0.0009	-0.0002
8	0.0000	-1.0000	0.5000	0.0000	-1.0014	0.5003	0.0000	-0.0014	0.0003
9	0.5000	-1.0000	0.5000	0.4998	-1.0009	0.4998	-0.0002	-0.0009	-0.0002
10	-0.5000	-0.8000	-0.5000	-0.4995	-0.8009	-0.4995	0.0005	-0.0009	0.0005
11	0.0000	-0.8000	-0.5000	0.0000	-0.8020	-0.5003	0.0000	-0.0020	-0.0003
12	0.5000	-0.8000	-0.5000	0.4995	-0.8009	-0.4995	-0.0005	-0.0009	0.0005
13	-0.5000	-0.8000	0.0000	-0.4991	-0.8002	-0.0003	0.0009	-0.0002	-0.0003
14	0.0000	-0.8000	0.0000	0.0000	-0.8021	-0.0000	0.0000	-0.0021	-0.0000
15	0.5000	-0.8000	0.0000	0.4991	-0.8002	-0.0003	-0.0009	-0.0002	-0.0003
16	-0.5000	-0.8000	0.5000	-0.4997	-0.8011	0.4997	0.0003	-0.0011	-0.0003
17	0.0000	-0.8000	0.5000	0.0000	-0.8016	0.5005	0.0000	-0.0016	0.0005
18	0.5000	-0.8000	0.5000	0.4997	-0.8011	0.4997	-0.0003	-0.0011	-0.0003
19	-0.5000	-0.6000	-0.5000	-0.4990	-0.6013	-0.4991	0.0010	-0.0013	0.0009
20	0.0000	-0.6000	-0.5000	0.0000	-0.6025	-0.5007	0.0000	-0.0025	-0.0007
21	0.5000	-0.6000	-0.5000	0.4990	-0.6013	-0.4991	-0.0010	-0.0013	0.0009
22	-0.5000	-0.6000	0.0000	-0.4980	-0.5999	-0.0006	0.0020	0.0001	-0.0006
23	0.0000	-0.6000	0.0000	0.0000	-0.6031	-0.0001	0.0000	-0.0031	-0.0001
24	0.5000	-0.6000	0.0000	0.4980	-0.5999	-0.0006	-0.0020	0.0001	-0.0006
25	-0.5000	-0.6000	0.5000	-0.4995	-0.6016	0.4995	0.0005	-0.0016	-0.0005
26	0.0000	-0.6000	0.5000	0.0000	-0.6017	0.5010	0.0000	-0.0017	0.0010
27	0.5000	-0.6000	0.5000	0.4995	-0.6016	0.4995	-0.0005	-0.0016	-0.0005

Table D.2: Measurement errors using intersection of headings method. The summary statistics are provided in Table 5.2. All values are in meters.

	Actual Position			Measured Position			Error		
No.	x_{act}	y_{act}	z_{act}	x_{meas}	y_{meas}	z_{meas}	x_{err}	y_{err}	z_{err}
1	-0.5000	-1.0000	-0.5000	-0.6211	-1.3256	-0.7402	-0.1211	-0.3256	-0.2402
2	0.0000	-1.0000	-0.5000	0.0000	-0.8811	-0.4500	0.0000	0.1189	0.0500
3	0.5000	-1.0000	-0.5000	0.6211	-1.3256	-0.7402	0.1211	-0.3256	-0.2402
4	-0.5000	-1.0000	0.0000	-0.3667	-0.6897	0.0000	0.1333	0.3103	0.0000
5	0.0000	-1.0000	0.0000	0.0000	-0.9894	0.0000	0.0000	0.0106	0.0000
6	0.5000	-1.0000	0.0000	0.3667	-0.6897	0.0000	-0.1333	0.3103	0.0000
7	-0.5000	-1.0000	0.5000	-0.6211	-1.3256	0.7402	-0.1211	-0.3256	0.2402
8	0.0000	-1.0000	0.5000	0.0000	-0.8811	0.4500	0.0000	0.1189	-0.0500
9	0.5000	-1.0000	0.5000	0.6211	-1.3256	0.7402	0.1211	-0.3256	0.2402
10	-0.5000	-0.8000	-0.5000	-0.3418	-0.5477	-0.3314	0.1582	0.2523	0.1686
11	0.0000	-0.8000	-0.5000	0.0000	-0.8811	-0.4500	0.0000	-0.0811	0.0500
12	0.5000	-0.8000	-0.5000	0.3418	-0.5477	-0.3314	-0.1582	0.2523	0.1686
13	-0.5000	-0.8000	0.0000	-0.7647	-1.2209	0.0000	-0.2647	-0.4209	0.0000
14	0.0000	-0.8000	0.0000	0.0000	-0.9894	0.0000	0.0000	-0.1894	0.0000
15	0.5000	-0.8000	0.0000	0.7647	-1.2209	0.0000	0.2647	-0.4209	0.0000
16	-0.5000	-0.8000	0.5000	-0.3418	-0.5477	0.3314	0.1582	0.2523	-0.1686
17	0.0000	-0.8000	0.5000	0.0000	-0.8811	0.4500	0.0000	-0.0811	-0.0500
18	0.5000	-0.8000	0.5000	0.3418	-0.5477	0.3314	-0.1582	0.2523	-0.1686
19	-0.5000	-0.6000	-0.5000	-0.5310	-0.6625	-0.5190	-0.0310	-0.0625	-0.0190
20	0.0000	-0.6000	-0.5000	0.0000	-0.7867	-0.6000	0.0000	-0.1867	-0.1000
21	0.5000	-0.6000	-0.5000	0.5310	-0.6625	-0.5190	0.0310	-0.0625	-0.0190
22	-0.5000	-0.6000	0.0000	-0.3903	-0.4772	0.0000	0.1097	0.1228	0.0000
23	0.0000	-0.6000	0.0000	0.0000	-0.4773	0.0000	0.0000	0.1227	0.0000
24	0.5000	-0.6000	0.0000	0.3903	-0.4772	0.0000	-0.1097	0.1228	0.0000
25	-0.5000	-0.6000	0.5000	-0.5310	-0.6625	0.5190	-0.0310	-0.0625	0.0190
26	0.0000	-0.6000	0.5000	0.0000	-0.7867	0.6000	0.0000	-0.1867	0.1000
27	0.5000	-0.6000	0.5000	0.5310	-0.6625	0.5190	0.0310	-0.0625	0.0190

Table D.3: Measurement errors using intersection of headings method with cross correlation. The summary statistics are provided in Table 5.3. All values are in meters.

	Actual Position			Measured Position			Error		
No.	x_{act}	y_{act}	z_{act}	x_{meas}	y_{meas}	z_{meas}	x_{err}	y_{err}	z_{err}
1	-0.5000	-1.0000	-0.5000	-0.4944	-0.9864	-0.4898	0.0056	0.0136	0.0102
2	0.0000	-1.0000	-0.5000	-0.0000	-1.0080	-0.5030	-0.0000	-0.0080	-0.0030
3	0.5000	-1.0000	-0.5000	0.4944	-0.9864	-0.4898	-0.0056	0.0136	0.0102
4	-0.5000	-1.0000	0.0000	-0.5094	-1.0228	0.0000	-0.0094	-0.0228	0.0000
5	0.0000	-1.0000	0.0000	0.0000	-1.0018	0.0000	0.0000	-0.0018	0.0000
6	0.5000	-1.0000	0.0000	0.5094	-1.0228	0.0000	0.0094	-0.0228	0.0000
7	-0.5000	-1.0000	0.5000	-0.4944	-0.9864	0.4898	0.0056	0.0136	-0.0102
8	0.0000	-1.0000	0.5000	-0.0000	-1.0080	0.5030	-0.0000	-0.0080	0.0030
9	0.5000	-1.0000	0.5000	0.4944	-0.9864	0.4898	-0.0056	0.0136	-0.0102
10	-0.5000	-0.8000	-0.5000	-0.5090	-0.8151	-0.5097	-0.0090	-0.0151	-0.0097
11	0.0000	-0.8000	-0.5000	0.0000	-0.7974	-0.5026	0.0000	0.0026	-0.0026
12	0.5000	-0.8000	-0.5000	0.5090	-0.8151	-0.5097	0.0090	-0.0151	-0.0097
13	-0.5000	-0.8000	0.0000	-0.4911	-0.7868	0.0000	0.0089	0.0132	0.0000
14	0.0000	-0.8000	0.0000	0.0000	-0.7938	-0.0000	0.0000	0.0062	-0.0000
15	0.5000	-0.8000	0.0000	0.4911	-0.7868	0.0000	-0.0089	0.0132	0.0000
16	-0.5000	-0.8000	0.5000	-0.5090	-0.8151	0.5097	-0.0090	-0.0151	0.0097
17	0.0000	-0.8000	0.5000	0.0000	-0.7974	0.5026	0.0000	0.0026	0.0026
18	0.5000	-0.8000	0.5000	0.5090	-0.8151	0.5097	0.0090	-0.0151	0.0097
19	-0.5000	-0.6000	-0.5000	-0.4909	-0.5888	-0.4912	0.0091	0.0112	0.0088
20	0.0000	-0.6000	-0.5000	0.0000	-0.5943	-0.4964	0.0000	0.0057	0.0036
21	0.5000	-0.6000	-0.5000	0.4909	-0.5888	-0.4912	-0.0091	0.0112	0.0088
22	-0.5000	-0.6000	0.0000	-0.5065	-0.6083	0.0000	-0.0065	-0.0083	0.0000
23	0.0000	-0.6000	0.0000	-0.0000	-0.6098	0.0000	-0.0000	-0.0098	0.0000
24	0.5000	-0.6000	0.0000	0.5065	-0.6083	0.0000	0.0065	-0.0083	0.0000
25	-0.5000	-0.6000	0.5000	-0.4909	-0.5888	0.4912	0.0091	0.0112	-0.0088
26	0.0000	-0.6000	0.5000	0.0000	-0.5943	0.4964	0.0000	0.0057	-0.0036
27	0.5000	-0.6000	0.5000	0.4909	-0.5888	0.4912	-0.0091	0.0112	-0.0088

Table D.4: Measurement errors using intersection of headings method with weighted cross correlation. The summary statistics are provided in Table 5.4. All values are in meters.

	Actual Position			Measured Position			Error		
No.	x_{act}	y_{act}	z_{act}	x_{meas}	y_{meas}	z_{meas}	x_{err}	y_{err}	z_{err}
1	-0.5000	-1.0000	-0.5000	-0.1124	-0.4207	-0.1384	0.3876	0.5793	0.3616
2	0.0000	-1.0000	-0.5000	0.0161	-0.4751	-0.1816	0.0161	0.5249	0.3184
3	0.5000	-1.0000	-0.5000	0.1115	-0.3668	-0.1502	-0.3885	0.6332	0.3498
4	-0.5000	-1.0000	0.0000	-0.1586	-0.4290	-0.0324	0.3414	0.5710	-0.0324
5	0.0000	-1.0000	0.0000	0.0275	-0.3841	0.0443	0.0275	0.6159	0.0443
6	0.5000	-1.0000	0.0000	0.1503	-0.4918	0.0010	-0.3497	0.5082	0.0010
7	-0.5000	-1.0000	0.5000	-0.1648	-0.5751	0.0761	0.3352	0.4249	-0.4239
8	0.0000	-1.0000	0.5000	0.0570	-0.7083	0.2096	0.0570	0.2917	-0.2904
9	0.5000	-1.0000	0.5000	0.1736	-0.4534	0.1852	-0.3264	0.5466	-0.3148
10	-0.5000	-0.8000	-0.5000	-0.1511	-0.3801	-0.1477	0.3489	0.4199	0.3523
11	0.0000	-0.8000	-0.5000	0.0591	-0.4898	-0.1269	0.0591	0.3102	0.3731
12	0.5000	-0.8000	-0.5000	0.1247	-0.3786	-0.2100	-0.3753	0.4214	0.2900
13	-0.5000	-0.8000	0.0000	-0.1544	-0.5063	0.0072	0.3456	0.2937	0.0072
14	0.0000	-0.8000	0.0000	0.0164	-0.5649	-0.0438	0.0164	0.2351	-0.0438
15	0.5000	-0.8000	0.0000	0.1852	-0.3683	-0.0537	-0.3148	0.4317	-0.0537
16	-0.5000	-0.8000	0.5000	-0.1892	-0.6085	0.1892	0.3108	0.1915	-0.3108
17	0.0000	-0.8000	0.5000	-0.0130	-0.8667	0.2759	-0.0130	-0.0667	-0.2241
18	0.5000	-0.8000	0.5000	0.1379	-0.4102	0.3113	-0.3621	0.3898	-0.1887
19	-0.5000	-0.6000	-0.5000	-0.2672	-0.4862	-0.2421	0.2328	0.1138	0.2579
20	0.0000	-0.6000	-0.5000	0.1233	-1.0300	-0.4136	0.1233	-0.4300	0.0864
21	0.5000	-0.6000	-0.5000	0.1129	-0.2009	-0.1608	-0.3871	0.3991	0.3392
22	-0.5000	-0.6000	0.0000	-0.1719	-0.3312	-0.0218	0.3281	0.2688	-0.0218
23	0.0000	-0.6000	0.0000	-0.0096	-0.3211	-0.0031	-0.0096	0.2789	-0.0031
24	0.5000	-0.6000	0.0000	0.3564	-0.7467	-0.0466	-0.1436	-0.1467	-0.0466
25	-0.5000	-0.6000	0.5000	-0.1322	-0.2464	0.1567	0.3678	0.3536	-0.3433
26	0.0000	-0.6000	0.5000	-0.0018	-0.3595	0.1259	-0.0018	0.2405	-0.3741
27	0.5000	-0.6000	0.5000	0.3918	-0.6698	0.3890	-0.1082	-0.0698	-0.1110

Table D.5: Measurement errors from intersection of headings method using signals from FEM simulator. The summary statistics are provided in Table 5.5. All values are in meters.

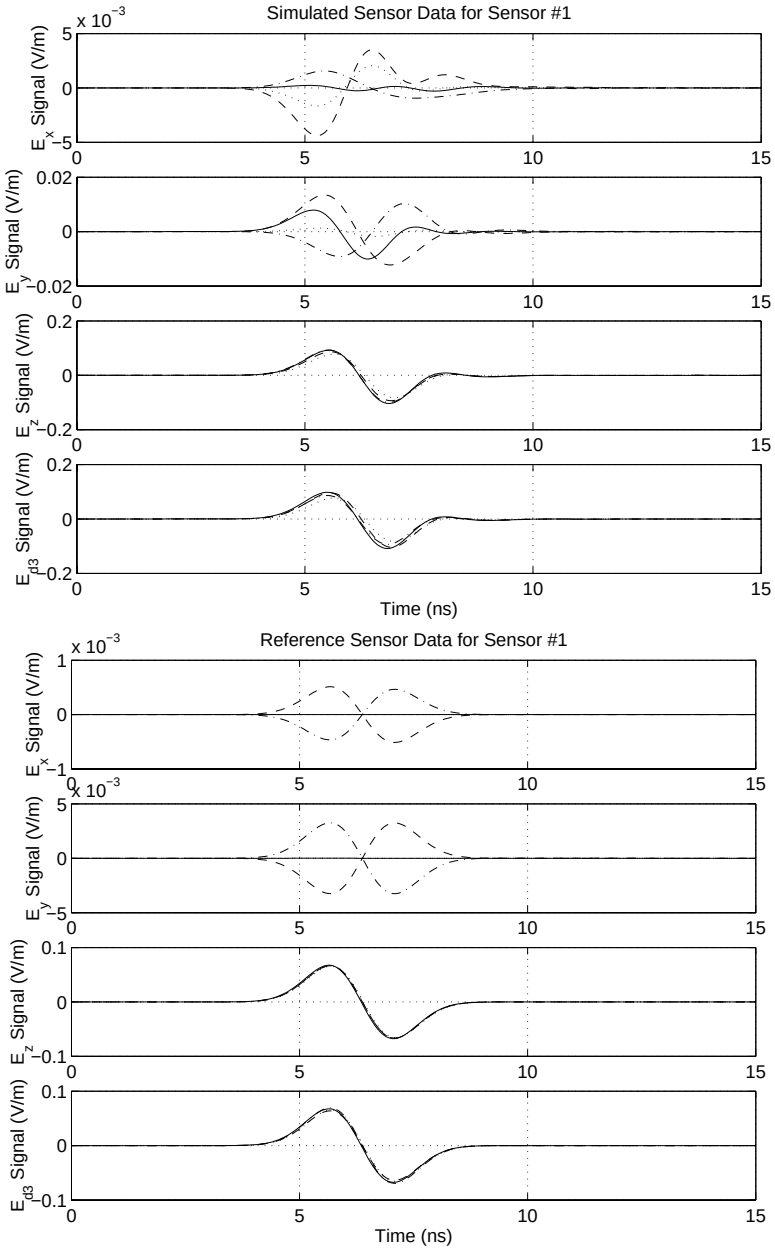

Figure D.1: Sample of signals using FEM and analytical for a TDOA quadruple 1 for Source Location 5, (0.00, -1.00, 0.00). The exploded view is provided in Figure 5.7.

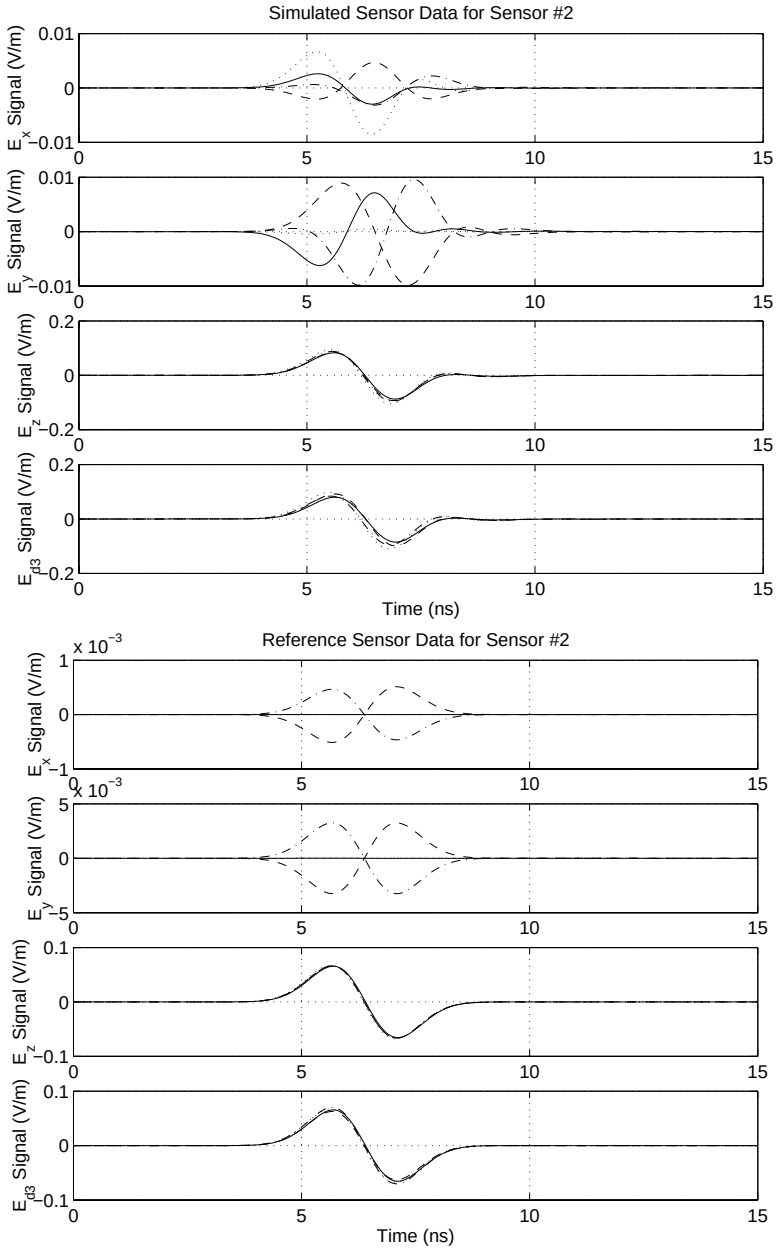

Figure D.2: Sample of signals using FEM and analytical for a TDOA quadruple 2 for Source Location 5, (0.00, -1.00, 0.00). The exploded view is provided in Figure D.3.

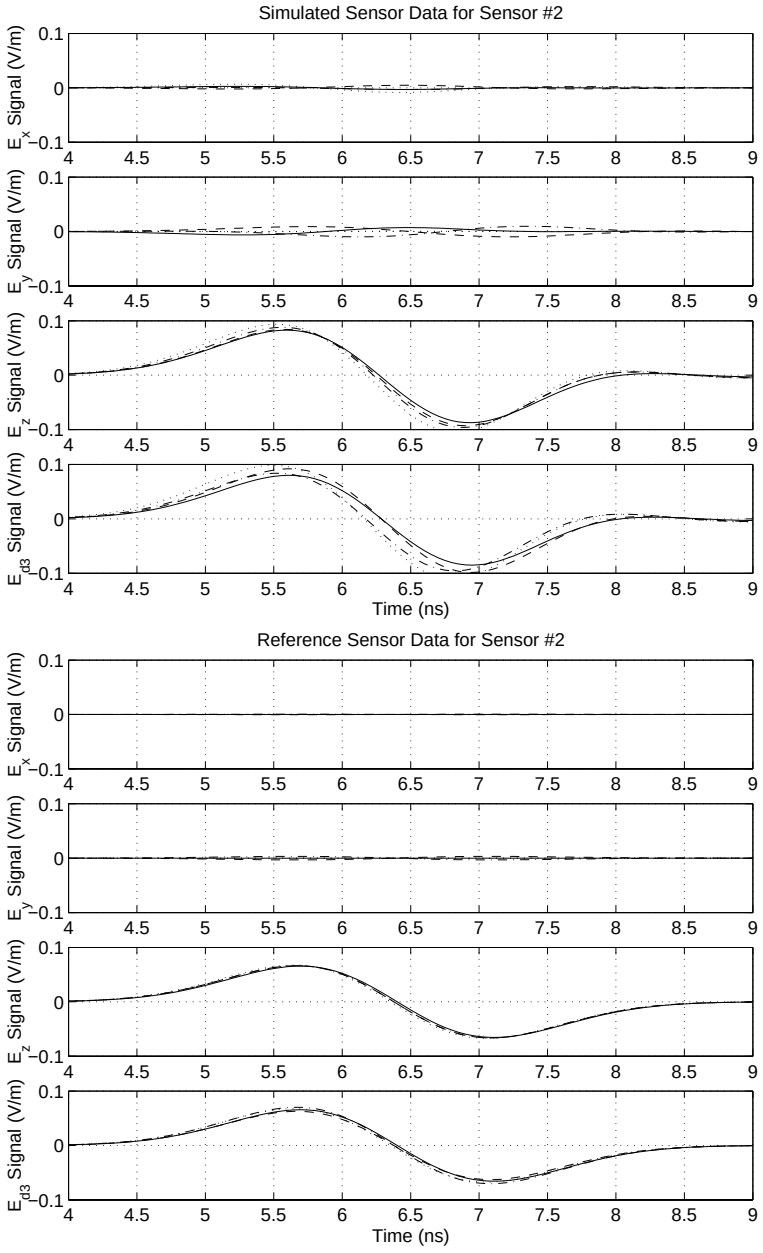

Figure D.3: Sample of signals using FEM and analytical for a TDOA quadruple 2 for Source Location 5, (0.00, -1.00, 0.00), in exploded view. Full signals are shown in Figure D.2.

References

[1] Ansoft Corporation website. Internet http://www.ansoft.com/, October 2005.

[2] Ansys Inc. corporate website. Internet http://www.ansys.com/, October 2005.

[3] Ascension Technology Corporation corporate website. Internet http://www.ascension-tech.com/, October 2004.

[4] Paramvir Bahl and Venkata N. Padmanabhan. RADAR: An in-building RF-based user location and tracking system. In *INFOCOM 2000, Nineteenth Annual Joint Conference of the IEEE Computer and Communications Societies*, volume 2, pages 775 –784, March 2000.

[5] Constantine A. Balanis. *Advanced Engineering Electromagnetics*. John Wiley & Sons, New York, 1989.

[6] Constantine A. Balanis. *Antenna Theory, Analysis and Design*. John Wiley & Sons, New York, 1997.

[7] John D. Bard, Frederic M. Ham, and W. Linwood Jones. An algebraic solution to the time difference of arrival equations. In *Bringing Together Education, Science and Technology*, pages 313–319. IEEE Southeastcon '96, April 1996.

[8] Jean-Pierre Berenger. A perfectly matched layer for the absorption of electromagnetic waves. *Journal of Computational Physics*, 114:185–200, 1994.

[9] Jean-Pierre Berenger. Three-dimensional perfectly matched layer for the absorption of electromagnetic waves. *Journal of Computational Physics*, 127:363–379, 1996.

[10] David Betounes. *Partial Differential Equations for Computational Science With Maple and Vector Analysis*. Springer-Verlag, 1998.

[11] Craig R. Bina. GEOL C15-0 Supplementary Material: Vector Differential Operators. Internet http://www.earth.northwestern.edu/people/craig/teach/315-0/vect_op/, 1996. Accessed February 1, 2005.

[12] William E. Boyse and Andrew A. Seidl. A hybrid finite element method for 3-D scattering using nodal and edge elements. *IEEE Transactions on Antennas and Propagation*, 42(10):1436–1442, October 1994.

[13] Michael S. Brandstein, John E. Adcock, and Harvey F. Silverman. A closed-form location estimator for use with room environment microphone arrays. *IEEE Transactions on Speech and Audio Processing*, 5(1):45–50, January 1997.

[14] David Brandwood. *Fourier Transforms in Radar and Signal Processing*. Artech House, Boston, MA, 2003.

[15] Eli Brookner. Phased arrays for the new millenium. In *Proceedings of the Eighteenth National Radio Science Conference*, volume 1, pages 1–13, Mansoura, Egypt, March 2001.

[16] Y.T. Chan and K.C. Ho. An efficient closed-form localization solution from time difference of arrival measurements. In *IEEE International Conference on Accoustics, Speech, and Signal Processing*, volume 2, pages 393–396, April 1994.

[17] Daniel Charles. Do maps have morals? *Technology Review: MIT's Magazine of Innovation*, 108(6):77–79, June 2005.

[18] Y. H. Cho, M.-L. Ha, W. Choi, C. Pyo, and Y.-S. Kwon. Floating-patch MEMS antennas on HRS substrate for millimetre-wave applications. *Electronics Letters*, 41(1):5–6, January 2005.

[19] Comsol: FEMLAB - Multiphysics Modelling. Internet http://www.comsol.com/, October 2004.

[20] Comsol, Inc. *FEMLAB 3 Electromagnetics Module User's Guide*, version 3.1 edition, October 2004.

[21] Comsol, Inc. *FEMLAB 3 Modelling Guide*, version 3.1 edition, October 2004.

[22] Comsol, Inc. *FEMLAB 3 User's Guide*, version 3.1 edition, October 2004.

[23] Donald A. Danielson. *Vectors and Tensors in Engineering and Physics*. Westview Press, second edition, 2003.

[24] W. Alan Davis and Krishna K. Agarwal. *Radio Frequency Circuit Design*. John Wiley & Sons, Toronto, 2001.

[25] Franco De Flaviis, Massimo G. Noro, G. Franceschetti Rodolfo E. Diaz, and Nicolaos G. Alexopoulos. A time-domain vector potential formulation for the solution of electromagnetic problems. *IEEE Microwave and Guided Wave Letters*, 8(9):310–312, September 1998.

[26] Kutluyil Doğançay. Emitter localization using clustering-based bearing association. *IEEE Transactions on Aerospace and Electronic Systems*, 41(2):525–536, April 2005.

[27] Herbert Edelsbrunner. *Geometry and Topology for Mesh Generation*. Cambridge University Press, New York, 2001.

[28] Faro Technologies Inc. corporate website. Internet http://www.faro.com/, October 2004.

[29] II G. Mellen, , M. Pachter, and J. Racquet. Closed-form solution for determining emitter location using time difference of arrival measurements. *IEEE Transactions on Aerospace and Electronic Systems*, 39(3):1056–1058, July 2003.

[30] Günter W Hein. From GPS and GLONASS via EGNOS to GALILEO - positioning and navigation in the 3rd millenium. *Survey Ireland*, 16, Winter 1999.

[31] Jeffrey Hightower and Gaetano Borriello. Location systems for ubiquitous computing. *Computer*, 34(8):57–66, August 2001.

[32] R. J. James. A history of radar. *IEE Review*, 35(9):343–349, October 1989.

[33] Dan Jiao, A. Arif Ergin, Balasubramaniam Shanker, Eric Michielssen, and Jian-Ming Jin. A fast higher-order time-domain finite element-boundary integral method for 3-D

electromagnetic scattering analysis. *IEEE Transactions on Antennas and Propagation*, 50(9):1192–1202, September 2002.

[34] Dan Jiao and Jian-Ming Jin. An effective algorithm for implementing perfectly matched layers in time-domain finite-element simulation of open-region EM problems. *IEEE Transactions on Antennas and Propagation*, 50(11):1615–1623, November 2002.

[35] Dan Jiao, Jian-Ming Jin, Eric Michielssen, and Douglas J. Riley. Time-domain finite-element simulation of three-dimensional scattering and radiation problems using perfectly matched layers. *IEEE Transactions on Antennas and Propagation*, 51(2):296–305, February 2003.

[36] Jianming Jin. *The Finite Element Method in Electromagnetics*. John Wiley & Sons, second edition, 2002.

[37] Walter Pereira Carpes Jr., Lionel Pichon, and Adel Razek. A 3D finite element method for the modelling of bounded and unbounded electromagnetic problems in the time domain. *International Journal of Numerical Modelling: Electronic Networks, Devices and Fields*, 13:527–540, 2000.

[38] Victor N. Kaliakin. *Introduction to Approximate Solution Techniques, Numerical Modelling, and Finite Element Methods*. Marcel Dekker, Inc., New York, 2002.

[39] Elliott D. Kaplan, editor. *Understanding GPS Principles and Applications*. Artech House, Boston, 1996.

[40] Norvald Kjerstad. The role of LORAN-C in present and future navigation: from a norwegian nautical perspective. *Journal of Navigation*, 55(2):185–195, 2002.

[41] Karl S. Kunz and Raymond J. Luebbers. *The Finite Difference Time Domain Method for Electromagnetics*. CRC Press, Ann Arbour, MI, 1993.

[42] Jin-Fa Lee, Robert Lee, and Andreas Cangellaris. Time domain finite-element methods. *IEEE Transactions on Antennas and Propagation*, 45(3):430–442, March 1997.

[43] Peter Monk. *Finite Element for Maxwell's Equations*. Clarendon Press, Oxford, 2003.

[44] Peter Monk and Kevin Parrott. Phase-accuracy comparisons and improved far-field estimates for 3-D edge elements on tetrahedral meshes. *Journal of Computational Physics*, 170:614–641, 2001.

[45] Northern Digital Inc. (NDI) corporate website. Internet http://www.ndigital.com/, October 2004.

[46] Alan V. Oppenheim, Alan S. Willsky, and Syed Hamid Nawab. *Signals and Systems*. Prentice Hall, Upper Saddle River, NJ, second edition, 1997.

[47] Bradford W. Parkinson, James J. Spilker Jr., Penina Axelrad, and Per Enge, editors. *Global Positioning System: Theory and Applications, Volume I*, volume 163 of *Progress in Astronautics and Aeronautics*. American Institute of Aeronautics and Astronautics, 1996.

[48] Bradford W. Parkinson, James J. Spilker Jr., Penina Axelrad, and Per Enge, editors. *Global Positioning System: Theory and Applications, Volume II*, volume 164 of *Progress in Astronautics and Aeronautics*. American Institute of Aeronautics and Astronautics, 1996.

[49] Terry M. Peters. Image-guided surgery: From x-rays to virtual reality. *Computer Methods in Biomechanics and Biomedical Engineering*, 3:27–57, 2000.

[50] Polhemus corporate website. Internet http://www.polhemus.com/, October 2004.

[51] Boaz Porat. *A Course in Digital Signal Processing*. John Wiley & Sons, Toronto, 1997.

[52] K.F. Riley, M.P. Hobson, and S.J. Bence. *Mathematical Methods for Physics and Engineering*. Cambridge University Press, New York, 2003.

[53] Romer CimCore corporate website. http://www.romer.com/, October 2004.

[54] Thomas Rylander and Jian-Ming Jin. Perfectly matched layer for the time domain finite element method. *Journal of Computational Physics*, 200:238–250, May 2004.

[55] Thomas Rylander and Jian-Ming Jin. Perfectly matched layer in three dimensions for the time-domain finite element method applied to radiation problems. *IEEE Transactions on Antennas and Propagation*, 53(4):1489–1499, April 2005.

[56] H.C. Schau and A.Z. Robinson. Passive source localization employing intersecting spherical surfaces from time-of-arrival differences. *IEEE Transactions on Acoustics, Speech and Signal Processing*, 35(8):1223–1225, August 1987.

[57] H. M. Schey. *Div, Grad, Curl and All That, An Informal Text on Vector Calculus*. W. W. Norton & Company, 1973.

[58] Julius O. Smith and Jonathan S. Abel. Closed-form least-squares source location estimation from range-difference measurements. *IEEE Transactions on Acoustics, Speech and Signal Processing*, 35(12):1661–1669, December 1987.

[59] Andreas Stelzer, Alexander Fischer, and Martin Vossiek. A new technology for precise local position measurement – LPM. *Microwave Symposium Digest, 2004 IEEE MTT-S International*, 2:665–658, June 2004.

[60] Andreas Stelzer, Klaus Pourvoyeur, and Alexander Fischer. Concept and application of LPM– a novel 3-D local position measurement system. *IEEE Trans. on Microwave Theory and Techniques*, 52(12):2664–2669, December 2004.

[61] Dennis M. Sullivan. *Electromagnetic Simulation Using the FDTD Method*. IEEE Press, New York, 2000.

[62] Allen Taflove. *Computational Electrodynamics: The Finite-Difference Time-Domain Method*. Artech House, Boston, MA, 1995.

[63] James Bao-Yen Tsui. *Fundamentals of Global Positioning System Receivers: A Software Approach*. John Wiley and Sons, Toronto, 2000.

[64] John Leonidas Volakis, Arindam Chatterjee, and Leo C. Kempel. *Finite Element Method for Electromagnetics: Antennas, Microwave Circuits, and Scattering Applications*. IEEE Press, New York, 1998.

[65] John G. Webster, editor. *Electrical Measurement, Signal Processing, and Displays*. CRC Press, New York, 2004.

[66] Eric W. Weisstein. Cross-correlation. From Mathworld – A Wolfram Web Resource. http://mathworld.wolfram.com/Cross-Correlation.html, November 2005.

[67] Eric W. Weisstein. Least squares fitting–polynomial. From Mathworld – A Wolfram Web Resource. http://mathworld.wolfram.com/LeastSquaresFittingPolynomial.html, January 2006.

[68] Andrew D. Wiles, David G. Thompson, and Donald D. Frantz. Accuracy assessment and interpretation for optical tracking systems. In *Proceedings of SPIE, Medical Imaging, Visualization, Image-Guided Procedures, and Display*, volume 5367, pages 421–432, San Diego, CA, USA, February 2004.

[69] David A. Winter. *Biomechanics and Motor Control of Human Movement*. John Wiley & Sons, Toronto, 1990.

[70] Xpect Solutions, Inc. CMMs and their history. Internet http://www.ecmmsales.com/cmm-history.htm, December 2005.

[71] Guochang Xu. *GPS Theory, Algorithms and Applications*. Springer-Verlag, New York, 2003.

[72] Kane S. Yee. Numerical solution of initial boundary value problems involving maxwell's equations in isotropic media. *IEEE Transactions on Antennas and Propagation*, 14(3):302–307, 1966.

[73] Derek P. Young, Catherine M. Keller, Dan W. Bliss, and Keith W. Forsythe. Ultra-wideband (UWB) transmitter location using time difference of arrival (TDOA) techniques. *The Thirty-Seventh Asilomar Conference on Signals, Systems & Computers*, 2:1225–1229, 2003.